THE EFFECT OF FIBER VOLUME FRACTION IN HIPERCOMP® SiC-SiC COMPOSITES

BY

DANIEL G. DUNN

A THESIS

SUBMITTED TO THE FACULTY OF

ALFRED UNIVERSITY

IN PARTIAL FULFILLMENT OF THE REQUIREMENTS
FOR THE DEGREE OF

DOCTOR OF PHILOSOPHY

IN

CERAMICS

ALFRED, NEW YORK

SEPTEMBER, 2010

THE EFFECT OF FIBER VOLUME FRACTION IN HIPERCOMP® SIC-SIC COMPOSITES

BY

DANIEL G. DUNN

B.S. ALFRED UNIVERSITY (1994)

M.S. ALFRED UNIVERSITY (1996)

SIGNATURE OF AUTHOR (Signature on File)

APPROVED BY (Signature on File)
JAMES VARNER, ADVISOR

(Signature on File)
WILLIAM CARLSON, ADVISORY COMMITTEE

(Signature on File)
WILLIAM CARTY, ADVISORY COMMITTEE

(Signature on File)
OLIVIA GRAEVE, ADVISORY COMMITTEE

(Signature on File)
WALTER SCHULZE, CHAIR, ORAL THESIS DEFENSE

ACCEPTED BY (Signature on File)
DOREEN D. EDWARDS, DEAN
KAZUO INAMORI SCHOOL OF ENGINEERING

ACCEPTED BY (Signature on File)
NANCY J. EVANGELISTA, ASSOCIATE PROVOST
FOR GRADUATE AND PROFESSIONAL PROGRAMS
ALFRED UNIVERSITY

ACKNOWLEDGMENTS

This material is based upon work supported by United States Air Force under contract number FA8650-04-G-2466-003. I would like to thank Mike Cinibulk, the contract monitor, for his support in using this work for my thesis.

This report was prepared as an account of work sponsored by an agency of the United States Government. Neither the United States Government nor any agency thereof, nor any of their employees, makes any warranty, express or implied, or assumes any legal liability or responsibility for the accuracy, completeness, or usefulness of any information, apparatus, product, or process disclosed, or represents that its use would not infringe privately owned rights. Reference herein to any specific commercial product, process, or service by trade name, trademark, manufacturer, or otherwise does not necessarily constitute or imply its endorsement, recommendation, or favoring by the United States Government or any agency thereof. The views and opinions of authors expressed herein do not necessarily state or reflect those of the United States Government or any agency thereof

From GE, I thank Suresh Subramanian, Krishan Luthra, Jim Steibel, and Jim Vartuli for programmatic and logistical support in using this work for my thesis. I am extremely grateful to the entire CMC team at GE Global Research, GE Aviation, and GE Energy. I thank Mike Brun, Gary Buczkowski, Doug Carper, Greg Corman, Paul Dimascio, Joe Halada, Curt Johnson, Anteneh Kebbede, Dennis Landini, Krishan Luthra, Henry McGuigan, Peter Meschter, Ron Nimmer, Reza Sarrafi-Nour, Jim Steibel, Suresh Subramanian, Dan VanUithuizen, Jim Vartuli and Mike Verrilli. I also thank A.J. Vallee for tensile testing and Tony Barbuto for sample polishing. I am especially grateful to Suresh Subramanian and Greg Corman for years of technical and non-technical support and guidance.

From Alfred University, I thank my advisor Dr. James Varner, as well as my committee members for their support and for accommodating me as a non-traditional student. I owe a special thanks to Dr. Doreen Edwards and Emilie Carney for guiding me through the logistics of being a distance-learning student.

TABLE OF CONTENTS

Page

LIST OF TABLES

LIST OF FIGURES

Page

ABSTRACT

The role of fiber volume fraction on the mechanical properties of HiPerComp® melt-infiltrated SiC-SiC pre-impregnated (prepreg) Ceramic Matrix Composite, CMC, was explored. The reinforcing fiber was Hi Nicalon Type S manufactured by Nippon Carbon Co., Japan. Room-temperature in-plane and interlaminar properties of unidirectional and multi-directional laminates were evaluated as a function of fiber volume fraction and microstructure. The proportional limit of the unidirectional material increased with fiber loading in agreement with the Aveston-Cooper-Kelly, ACK, model. The tensile properties were used to ascertain the elastic properties of the 0 and 90 plies. The ply-level properties were used with composite beam theory to successfully predict the flexure properties of cross-ply composites. Ply-level behavior was demonstrated through four-point bend tests and careful selection of the stacking sequence. Flexural proportional limits of 430 MPa were achieved in cross-ply laminates with a 2:1 bias, matching the matrix cracking strength of the unidirectional 0 degree composites. Fiber volume fraction was also found to have a significant effect on the creep behavior of the CMC. An increase in fiber loading resulted in a decrease in creep rate and an increase in rupture life and rupture strain at 1315°C. Creep-induced matrix cavitation was observed, and the overall creep behavior was consistent with the assumption that the fiber is more creep resistant than the matrix.

INTRODUCTION

CHAPTER I

1.1 Introduction and Objective

Ceramic Matrix Composites, CMCs, are a promising type of material for high-temperature structural applications, such as industrial gas turbines. One class of CMC that is being evaluated for use in turbines is MI SiC-SiC, which is a melt-infiltrated silicon-silicon carbide matrix reinforced by silicon carbide fiber. Relative to metallic superalloys, this material is desirable due to its higher temperature capability and lower density. This material, called HiPerComp®, has a temperature capability in excess of 1300°C and a density less than 3 g/cm^3.

The MI SiC-SiC CMC uses a boron-nitride-based fiber coating that allows the SiC fiber to de-bond from the Si-SiC matrix and impart toughness to the material. Non-linear stress-strain behavior with failure strains over 1% after matrix cracking has been observed for this material system.[1] This damage tolerance achieved through composite behavior makes the CMC desirable over monolithic ceramics that fail catastrophically. The purpose of this research is to develop a phenomenological understanding of the mechanical properties of this MI SiC-SiC prepreg material system through variation in fiber volume fraction.

LITERATURE REVIEW

CHAPTER II

2.1 Background on Melt Infiltrated SiC-SiC Composites

There are several approaches to fabricating the MI SiC-SiC CMC. A review of these options is given by Corman and Luthra.[1] In this study, the CMC is GE's HiPerComp® material. This material is made by first depositing a boron-nitride-based coating system on SiC fiber, and then drum winding the fiber through a bath of matrix precursor slip to form unidirectional prepreg tapes. These tapes are then laid up and laminated to create a preform. The preform is pyrolized to char any organic material and is then infiltrated with molten silicon. The silicon reacts with carbon in the preform to form silicon carbide. Ideally, any remaining porosity will be filled with silicon, resulting in a fully dense composite. The type of silicon carbide that makes up the matrix phase of this composite is often referred to as reaction-formed or reaction-bonded SiC.[1] The HiPerComp® material generates a 2-D structure by stacking multiple 1-D prepreg plies together while varying the orientation of the fibers in each ply. Plies with fibers running parallel to the sample test direction are typically referred to as zero plies or longitudinal plies. Plies with fibers perpendicular to the loading direction are known as 90-degree plies, cross plies, or transverse plies. There are a limited number of commercially available SiC fibers. A comparison of the properties of select fibers is given by Yun and DiCarlo[2] and a review of the development of SiC fibers is given by Bunsell and Piant.[3]

While there are a limited number of published studies on the HiPerComp® material, there is a larger body of literature on the slurry-cast version of MI SiC – SiC. In the slurry-cast process, the fiber is first woven into a 2-D cloth. Layers of the cloth are then stacked up to create a preform. The interfacial coatings are deposited into the preform through a chemical vapor infiltration, CVI, technique. An initial portion of the SiC matrix is also deposited via CVI. The remainder of the matrix phase is created by casting a slurry of matrix precursor into the still porous CVI preform, followed by a final silicon melt infiltration.[1] There are many important differences between this slurry-cast

material and the HiPerComp® prepreg CMC. Of importance for the present comparison is that the slurry-cast plies are composed of a 2-D woven cloth as opposed to the 1-D unidirectional prepreg tapes. The directional nature of the fiber plies is therefore different between these two systems.

2.2 Mechanics

Continuous fiber composites have been widely modeled in the literature. MI CMCs with a boron nitride interface coating belong to the category of brittle matrix composites. A review of the physics and mechanics that describe the behavior of brittle matrix composites is given by Evans and Zok.[4]

2.2.1 Ultimate Tensile Strength

It is well established that the strength of brittle ceramics is statistical in nature and is dependent upon the probability of the presence of flaws. The probability of finding a flaw decreases as the volume of the ceramic decreases. The maximum possible flaw size also decreases. As such, the strength of brittle ceramics is observed to increase as the test volume decreases. Small-diameter fibers of reasonable length and surface quality have small volumes, and therefore high strength.

In simplest terms, the ultimate tensile strength, **UTS**, of a composite can be described as the strength of the reinforcing fiber multiplied by the volume fraction of fiber in the test direction. Equation 1, given by Curtin,[5] is a more complete description that accounts for the statistical nature of the fibers. It is noteworthy that the analysis performed by Curtin[5] predicts the **UTS** of the CMC to be independent of the volume of the sample.

$$UTS = V_f S_C \left[\frac{2}{(m+2)}\right]^{1/(m+1)} \left[\frac{m+1}{m+2}\right] \quad (1)$$

where: V_f = fiber volume fraction
m = Weibull shape parameter
S_C = in situ characteristic fiber strength

This equation requires detailed information about the statistical distribution of the in situ strength of the fiber *after* it has been processed into a composite, accounting for any processing-induced fiber degradation. It predicts the **UTS** to scale linearly with the volume fraction of fibers.

The effect of fiber volume fraction on the prepreg MI SiC – SiC composite has not been studied for balanced-architecture composites; composites that have the same number of 0 and 90 degree plies. Nimmer, et al.[6] have reported results for the Hi Nicalon fiber-reinforced HiPerComp® material in which the fiber volume fraction was varied in the test direction by biasing the architecture. They studied composites with 0:90 ratios of 2:1, 1:1, and 1:2, as well as unidirectional composites. As expected, the **UTS** scaled linearly with the volume fraction of fibers in the test direction. In the current study, the fiber volume fraction will be varied at the ply level, and the expectation is that the **UTS** will scale with the fiber volume fraction.

2.2.2 Proportional Limit

The CMC is expected to show linear elastic behavior up until the onset of matrix cracking. The matrix-cracking stress is often referred to as the proportional limit, **PL**. The **PL** of CMCs is commonly described using a linear offset technique, according to ASTM C1275. A line with a slope equal to the sample modulus is drawn parallel to the linear portion of the stress-strain curve. This line is offset from the actual stress strain curve by plus 0.005% strain. The intersection of this offset line with the stress-strain curve is taken to be the **PL**, or the onset of matrix cracking. The matrix-cracking stress is an important parameter, since matrix cracks provide a potential path through which the atmosphere may reach and degrade the fiber matrix interface.[4] For this reason, it is expected that the **PL** will be the upper bound of the allowable CMC stress for long life applications.

Unidirectional composites have the reinforcing fibers running in just one direction. The **PL** as measured in the fiber direction, or 0 degree direction, of unidirectional composites was first described by Aveston, Cooper, and Kelly[7] and is often referred to as ACK theory. Their approach was later generalized by Budiansky et al.[8] Based on a balance between the applied stress and the tractions on the fibers in the crack wake, the lower bound for the onset of matrix cracking is [8]

$$PL = E_0\left[\frac{6\tau\Gamma_m V_f^{\,2} E_f}{(1-V_f)E_m^2 R E_0}\right]^{1/3} - \sigma^T \quad (2)$$

where:
V_f = fiber volume fraction
E_0 = 0 direction modulus
E_f = fiber modulus
E_m = matrix modulus
Γ_m = matrix fracture energy
τ = interfacial sliding friction
R = radius of fiber
σ^T = residual stress

It should be noted that E_0 is also a function of fiber volume fraction, as will be discussed in section 2.2.4. For the range of practical fiber volume fractions, this relationship predicts that **PL** will increase with fiber loading in a nearly linear fashion.

Most composite applications require fiber reinforcement in more than one direction. Cross-ply composites contain plies in which the fibers are oriented in the 0 direction as well as plies in which the fibers are oriented in the 90 direction. The linear elastic properties of a fiber ply are substantially different in the 0 and 90 directions. If the 90 plies are considered to act as flaws in the composite, then the lower bound for matrix cracking of cross ply laminates will be governed by the thickness of the cross ply, and is given by[9,10,11]

$$PL = \left[\frac{g(x)\Gamma_{90}E_{90}}{t}\right]^{1/2} \quad (3)$$

where:
E_{90} = 90 ply modulus
Γ_{90} = 90 ply fracture energy
t = 90 ply thickness
g(x) = elastic mismatch parameter

This Griffith type equation assumes the intrinsic flaw size of the CMC to be the width of the 90 ply. The validity of this assumption will depend upon the quality of the microstructure of the material as well as the spatial distribution of the fibers.

The **PL** of 2D woven slurry-cast CMC reinforced with Sylramic fiber has been shown by Morscher[12] to increase with fiber loading. However, it is not clear whether or not this trend will hold true for balanced prepreg material in which the linear elastic properties of the 0 and 90 plies are substantially different. Beyerle et al.[9] describe the

sequence of matrix cracking in cross-ply laminates based on direct observation of cracking in calcium-alumino-silicate glass-matrix composites reinforced with SiC fiber. They showed that the matrix cracks initiated in the 90 plies and the **PL** followed the relationship given in equation 3.

Morscher et al.[13] have developed a semi-empirical Griffith-type relationship in which the **PL** of slurry-cast SiC-SiC CMCs with woven plies is shown to be inversely proportional to the square root of the diameter of the tow bundle in the transverse direction. In this case, the 90-degree tow bundles in the woven cloth act as the critical flaw for matrix cracking.

2.2.3 Strain at UTS

Composite behavior differs from that of monolithic ceramics in that the material does not fail catastrophically. Instead, at stresses above **PL**, CMCs exhibit non-linear stress-strain behavior. Commercially available stoichiometric silicon carbide fiber has a tensile strength on the order of 3 GPa, with a modulus of ~ 400 GPa. Dividing the strength of this fiber by its modulus gives a fiber failure strain of ~0.7%. Since the failure strain of the composite is dependent on the strain in the fiber, this simple calculation can be used to estimate the strain that could be achieved with a given fiber in a well-made composite. As described above, the strength of the fiber in the composite may be different from that of the raw fiber tow, and will vary with gauge length. A full analysis by Curtin[14] derives the failure strain in a unidirectional composite with tightly spaced matrix cracks to be

$$\varepsilon_f = \frac{\sigma_{cf}}{E_f}\left[\frac{2(\mathrm{m}+1)}{(\mathrm{m}+2)\mathrm{m}}\right]^{\frac{1}{\mathrm{m}+1}} \qquad \text{where:} \quad \begin{array}{l} \mathrm{m} = \text{fiber Weibull modulus} \\ E_f = \text{fiber modulus} \\ \sigma_{cf} = \text{characteristic fiber strength} \end{array} \tag{4}$$

where σ_{cf} is the characteristic fiber strength for a gauge length equal to twice the fiber slip length in the CMC. The fiber slip length and the requirement of tightly spaced matrix cracks will be discussed in chapter IV.

The evolution of composite strain in a tensile pull test has been studied in the literature.[11,14-20] These models typically contain parameters that cannot be readily predicted and therefore need to be measured for the composite. The measured values are then used to fit the model to the experimental data. For example, the model developed by Curtin[14] requires the stress-dependent crack density and the final crack density, which need to be measured empirically. Similarly, simulated stress-strain curves can be generated based on constitutive laws that require multiple relationships to estimate various non-dimensional parameters.[3] All of these approaches require empirical data for calibration, making it difficult to use them as a predictive tool.

2.2.4 Modulus

The modulus, **E**, of a unidirectional CMC in the 0 direction, $\mathbf{E_0}$, is expected to follow a simple rule of mixtures based on the modulus and volume fraction of each phase present.

$$E_0 = \mathrm{V_f}\ E_f + \mathrm{V_m} E_m + \mathrm{V_c} E_c \qquad (5)$$

where:
$\mathrm{V_f}$ = fiber volume fraction
$\mathrm{E_f}$ = fiber modulus
$\mathrm{V_m}$ = matrix volume fraction
$\mathrm{E_m}$ = matrix modulus
$\mathrm{V_c}$ = coating volume fraction
$\mathrm{E_c}$ = coating modulus
$\mathrm{V_f} + \mathrm{V_m} + \mathrm{V_c} = 1$

The modulus of this same material will be different in the 90 direction. For the material system in question, the weak interfacial coating between the fiber and the matrix will prevent the fiber from contributing significantly to the transverse modulus. Assuming the effective modulus of the fiber in the transverse direction is zero, than the transverse composite ply modulus is[9]

$$E_{90} = \left[\frac{\left(1 + 2\eta V_f\right)}{\left(1 - \eta V_f\right)} \right] E_m \qquad (6)$$

where:
$\mathrm{V_f}$ = fiber volume fraction
$\mathrm{E_m}$ = matrix modulus
$\eta = -0.5$

Laminate theory predicts that the modulus of a cross-ply composite in the 0 or 90 directions will follow a rule of mixtures based on the moduli of the 0 and 90 plies and the ratio of 0 to 90 plies in the composite.

2.3 Ply-Level Behavior

The ply-level behavior of orthotropic materials is well established. The mechanics of such materials can be found in textbooks such as the one by Calcote.[21] While well established in polymer matrix composites, the ply-level behavior of cross-ply SiC-SiC CMCs, and in particular of the HiPerComp® material, has not been well characterized in the literature.

2.4 Creep Rupture

Composite creep behavior falls into two broad categories depending upon the relative creep resistance of the matrix and the reinforcing fiber. The behavior of SiC-SiC CMCs, where the matrix is more creep resistant than the fiber, was examined by Evans and Weber.[22] This outcome is expected in CMCs with a CVI SiC matrix reinforced with a fiber having a lower-use temperature such as Nicalon™ or Hi Nicalon™ (Nippon Carbide Co., Japan).[24] NASA has also reported this behavior for a SiC matrix reinforced with a nearly stoichiometric Sylramic-iBN fiber (COI Ceramics, CA).[23]

The excess free silicon that is characteristic of the MI process used in the present study makes the Si-SiC matrix more creep prone than a CVI SiC matrix. Recently, there have been studies[17,24-26] on the creep behavior of MI SiC-SiC composites fabricated using the slurry-cast method and reinforced with creep-resistant fibers such as Hi-Nicalon Type S ™ (Nippon Carbide Co., Japan), Tyranno SA3 (Ube Industries, Japan), and Sylramic-iBN (COI Ceramics, CA). The fiber reinforcement was in the form of plies of woven 2-D cloth. In these studies, it was inferred that the MI Si-SiC matrix creeps faster than the nearly stoichiometric SiC fiber. For this situation, during composite creep, stress will be transferred from the matrix to the fibers as modeled by McLean.[27] Evidence of this load redistribution phenomenon was inferred for this CMC through room temperature tensile testing following creep at 1315°C. The **PL** was observed to increase, as did the measured matrix residual compressive stress.[24-26] Additionally, the relative 1315°C creep

resistance of this CMC was reported to vary with the reinforcing fiber in a manner consistent with the fiber properties.[25] Under these conditions, Pujar and Morscher[25] reported that creep was primarily controlled by the fiber and, making the assumption that the fiber carries all of the load, considered normalizing composite stress based on fiber volume fraction as a possible way to compare creep results in these composites.

The model describing creep for a composite in which the matrix creeps faster than the fiber was developed by McLean for metal-matrix composites reinforced with SiC fiber.[27] This model has also been demonstrated for SiC fiber reinforced glass-matrix composites such as SiC – CAS.[28]

The minimum or secondary creep rate of many materials is typically described using a power-law relationship given in equation 8.[29] The Type S fiber used in this study has a slight excess of carbon, with a C-to-Si atomic ratio of ~1.05, as stated in the vendor product data sheets. The creep behavior of Type S fiber has been characterized by Sauder and Lamon.[30] For secondary creep, they measured the stress exponent **n** to be ~ 2.6 and attributed creep to grain-boundary sliding accommodated by carbon deformation.[30]

$$\varepsilon = A\sigma^{n} \qquad \text{where: } \varepsilon = \text{steady state or minimum creep rate},\ \sigma = \text{stress},\ A = \text{constant},\ n = \text{stress exponent constant} \tag{7}$$

There are many studies in the literature on the creep behavior of siliconized silicon carbide.[31-36] This material consists of interconnected networks of silicon and silicon carbide. At 1315°C, the temperature of interest in the current study, silicon deforms easily,[37] while the SiC grains are viewed to be essentially non-deforming.[31,32] The presence of any inter-granular phases could potentially control the relative motion of the grains. However, even for siliconized silicon carbide, the presence of a silicon phase at the SiC grain boundaries has not been observed.[33,35] Creep is therefore expected to be controlled by the breaking apart of SiC grains in order to allow for sliding.[31] The volume fraction of the more compliant silicon phase will influence the amount of SiC grain-to-grain contact and will therefore affect the creep resistance.[31] The creep resistance will

also be a function of grain size and other microstructural features such as porosity. The creep exponent **n** of siliconized silicon carbide has been shown to increase with applied stress. Data reported by Wiederhorn et al.[36] has been re-plotted in Figure 1 to illustrate this trend. The change in slope, **n**, was correlated to cavity formation in the material at higher stresses.

The matrix of a melt-infiltrated CMC contains excess free silicon, and is therefore expected to be more creep prone than the nearly stoichiometric Type S fiber. The creep rate of the HiPerComp® CMC matrix material at 1315°C at three stress levels was measured by Kebbede.[38] These data points are also included in Figure 1. The agreement with the data from Wiederhorn et al.[36] is coincidental, as the two materials have different microstructures. The results for Type S fiber reported Sauder and Lamon[30] are also included in Figure 1. This trend line was generated using equation 7 along with the reported creep exponent and stress level. The available data on the matrix and fiber support the expectation that the MI matrix will creep faster than the Type S fiber.

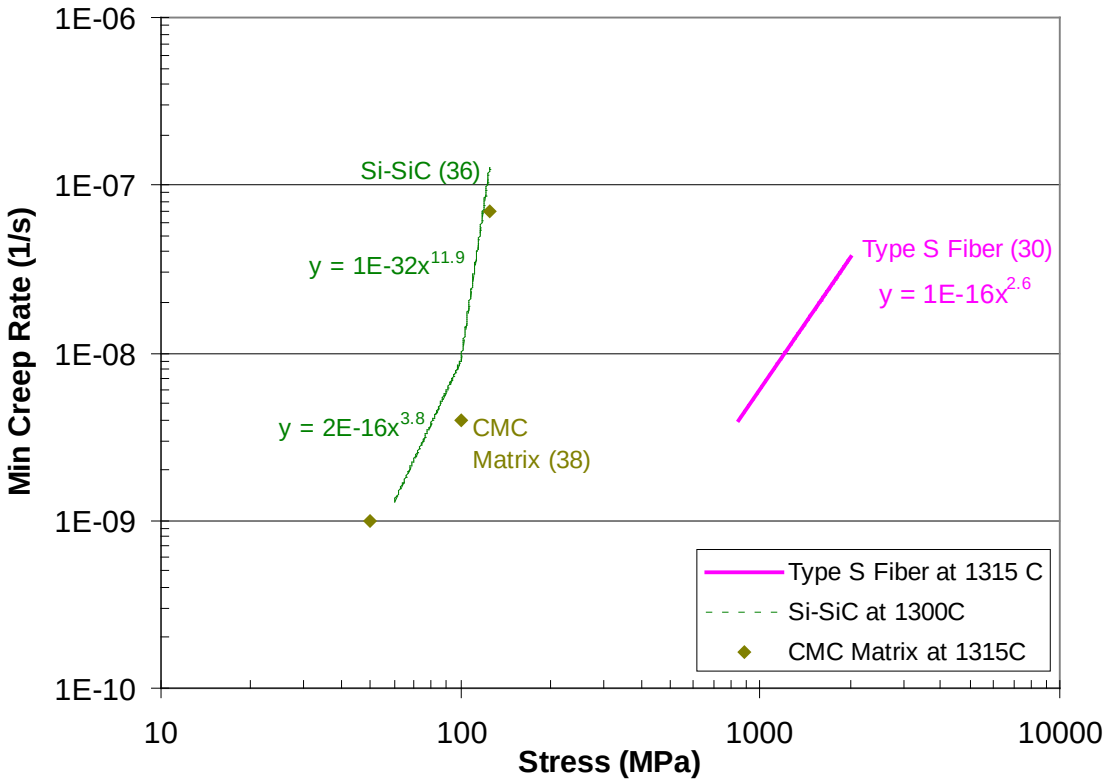

Figure 1. Plots of creep rate versus stress for siliconized silicon carbide at 1300C,[36] the CMC matrix at 1315°C,[38] and Type S fiber at 1315°C.[30]

Creep rupture life / stress curves are generated by plotting the time to rupture on a log scale against applied stress on a linear scale.[29] Typically, the data plotted in this manner fall on a straight line. Additionally, there have been efforts to fit the creep behavior of CMCs and SiC fibers to the Larson-Miller and the Monkman-Grant relationships.[39-42] The Larson-Miller approach uses an empirically calibrated failure parameter, Q, to relate the applied stress to rupture time and temperature.[42] The Larsen-Miller parameter, Q, is given by equation 8. The Monkman-Grant approach relates rupture time to the minimum creep rate through the empirical relationship given in equation 9. Materials that follow this relationship will produce a straight line when the creep rate and rupture time are plotted against each other on log scales. Some researchers believe that neither of these methods are adequate for describing CMC creep life,[23,42] and methods for describing the creep behavior of SiC-SiC CMCs are still evolving.

$$Q = T(\log t_r + C_1) \quad (8)$$

where: Q = Larsen-Miller Parameter
T = temperature
t_r= time to rupture
ε = steady state or minimum creep rate
m = constant (strain rate exponent)
C_1 = constant
C_2 = constant

$$t_r \varepsilon^m = C_2 \quad (9)$$

EXPERIMENTAL PROCEDURE

CHAPTER III

3.1 Overview

The effect of fiber volume fraction on room-temperature in-plane and interlaminar tensile properties of unidirectional and cross-ply composites was explored. The tensile properties were used to ascertain the elastic properties of the 0 and 90 plies. Through beam theory, ply-level behavior was demonstrated in cross-ply CMCs in flexure through careful selection of the stacking sequence. The effect of fiber volume fraction on creep rupture at 1315°C (2400°F) was evaluated.

3.2 Design of Experiments

3.2.1 Room-Temperature Bulk Mechanical Properties

The first design of experiments, DOE I, for room-temperature testing is given in Table I. Two panels for each condition were fabricated, and two tensile bars from each panel were tested. To minimize variation, panels A, B, and C were co-processed and were made using the same spool of coated fiber. Panels D, E, and F were made in the same manner, as were the replicate panels AA, BB, CC and DD, EE, FF. The coefficient of thermal expansion was measured for samples from panels A-F. Additional panels were fabricated using conditions B and C for evaluation of interlaminar tensile and shear properties.

Table I. Test Matrix for Room-Temperature Bulk Property Measurements

Test Condition	Fiber Loading	Test Direction V_f	Fiber Architecture	Initial Panel	# of Tensile Specimens	Replicate Panel	# of Tensile Specimens
A	low	0.11	(0-90-0-90)s	A	2	AA	2
B	medium	0.13	(0-90-0-90)s	B	2	BB	2
C	high	0.17	(0-90-0-90)s	C	2	CC	2
D	low	0.21	(0-0-0-0)s	D	2	DD	2
E	medium	0.26	(0-0-0-0)s	E	2	EE	2
F	high	0.33	(0-0-0-0)s	F	2	FF	2

The DOE II series of panels was constructed to allow a comparison of unidirectional and balanced-architecture composites with the same fiber volume fraction in the test direction. The samples from DOE II were compared to those of DOE I. Table II shows the samples produced for this purpose, where M = a layer of matrix of comparable thickness to a 90 ply. All of the panels in DOE II were co-processed and were made from the same spools of coated fiber. Two tensile specimens were tested from each panel. A balanced-architecture panel made with condition DOE I-C was included in DOE II in order to allow for a direct comparison (samples co-processed and made with the same coated fiber) of a balanced-architecture sample (0-90-0-90)s to a unidirectional sample where the 90 plies were replaced with matrix plies (0-M-0-M)s.

Table II. Test Matrix for Dilute Fiber Unidirectional Composites

Test Condition	Fiber Loading	Test Direction V_f	Fiber Architecture	Panel ID	# of Tensile Specimens
F	high	0.32	(0-0-0-0)s	FF	2
G	high	0.21	0-M-0)s	G	2
H	high	0.16	(0-M-0-M)s	H	2
J	high	0.11	(M-0-M)s	J	2
C	high	0.16	(0-90-0-90)s	CCC	2

3.2.2 Effect of Ply Thickness and Stacking Sequence

As discussed previously, the model given in equation 3 predicts the **PL** of cross-ply laminates to be a function of the thickness of the 90-degree plies. It is possible to critically test this model for the HiPerComp® system. By varying the pre-pregging

parameters, the ply thickness was changed. DOE III, as given in Table III, varies the ply thickness by a factor of two while maintaining the medium fiber volume fraction.

Table III. Test Matrix to Demonstrate the Effect of Ply Thickness on PL

Panel ID	Fiber Loading	Test Direction V_f	Fiber Architecture	Normalized Ply Thickness	# of Tensile Specimens
B	medium	0.13	(0-90-0-90)s	1.00	2
B1	medium	0.13	(0-90-0-90)s	0.67	2
B2	medium	0.13	(0-90-0-90)s	1.33	2

Alternatively, the effective ply thickness may be changed through the stacking sequence by varying the number of adjacent 90 plies in the laminate. For example, microstructurally, two adjacent 90 plies will look very similar to a single 90 ply with twice the nominal ply thickness. Stacking sequence is not expected to affect the initial linear modulus, the **UTS**, or the failure strain of a composite. The **PL** of the CMC as a function of the effective 90-ply thickness is explored in DOE IV, as described in Table IV.

Table IV. Test Matrix for the Effect of Stacking Sequence on PL

Panel ID	Fiber Loading	Test Direction V_f	Fiber Architecture	# of Adjacent 90 Plies	# of Tensile Specimens
K	high	0.17	**90**-0-**90**-0-**90**-0:0-**90**-0-**90**-0-**90**	1	4
L	high	0.17	0-**90-90**-0-0-**90:90**-0-0-**90-90**-0	2	4
M	high	0.17	0-**90-90-90**-0-0:0-0-**90-90-90**-0	3	4
N	high	0.17	0-90-0-0-**90-90:90-90**-0-0-90-0	4	4
O	high	0.17	0-0-0-**90-90-90:90-90-90**-0-0-0	6	4

3.2.3 Ply-Level Behavior

The in-plane tensile tests described above impose a uniform strain throughout the cross-section of the sample, and the properties obtained are representative of the bulk material. In order to observe local ply-level behavior in a cross-ply laminate, a test that induces a strain gradient in the material is desirable. The gradient will allow the local ply-level strains /stresses in the material to be varied. The linear elastic response of a cross-ply composite in bending can be modeled through a combination of beam theory

and laminate theory. Methods for the flexure analysis of composite beams composed of layers of materials with different moduli are well established and can be found in textbooks such as the one by Hibbeler.[43] Combining a flexure test with composite architecture variations will allow the properties of the 0 and 90 plies of a cross-ply composite to be interrogated.

The material with a high fiber volume fraction was used for the flexure test experiments in DOE V. A 2:1 biased 0:90 architecture was chosen in order to increase the likelihood of achieving the full matrix cracking strength of the outer 0 plies prior to cracking the inner 90 plies. Unidirectional composites were also tested in order to provide baseline values of the elastic ply-level flexural properties. The architectures used in DOE V are given in Table V. Four samples from each panel were tested in four-point bending. To allow a comparison between the flexure and tensile properties of the CMC, two samples from each panel were also tested in tension. Additionally, two flexure specimens were taken from the transverse direction of each panel in order to assess the property reduction of the 2:1 bias in the cross direction (1:2 bias). All flexure tests were performed on samples with as-fabricated surfaces. No surface polishing was performed.

Table V. DOE V. Test Matrix for Four-Point Bend Testing

Panel ID	Architecture	Fiber V_f	Test Orientation	# of Test Specimens	
				Tension	Flexure
P	0-0-0:0-0-0	0.33	longitudinal	2	4
Q	0-0-90:90-0-0	0.33	longitudinal	2	4
R	0-90-0:0-90-0	0.33	longitudinal	2	4
S	90-0-0:0-0-90	0.33	longitudinal	2	4
P	90-90-90:90-90-90	0.33	transverse	0	2
Q	90-90-0:0-90-90	0.33	transverse	0	2
R	90-0-90:90-0-90	0.33	transverse	0	2
S	0-90-90:90-90-0	0.33	transverse	0	2

3.2.4 Testing at 1315°C (2400°F)

The tensile properties of selected samples were measured at 1315°C (2400°F). In addition to these fast-fracture tests, creep-rupture testing was done for the medium- and high-fiber-volume-fraction composites at various stress levels. Two panels were

produced at each fiber loading. Again, the creep-rupture panels were co-processed using the same spools of coated fiber. For each fiber volume fraction, six samples were tested to failure at various stress levels.

3.3. Sample Fabrication

Ceramic matrix composites were made using GE's prepreg MI process. GE Ceramic Composite Products LLC, also known as CCP, located in Newark Delaware, manufactures GE's HiPerComp® material in this manner. For the present study, fiber with GE's proprietary coatings was obtained from CCP, and the subsequent processing was done at GE's Global Research Center in Niskayuna, NY. The silicon carbide fiber used to reinforce the composites in this study was Hi Nicalon Type S, manufactured by Nippon Carbon, Japan. The coated fiber was drawn through a bath of matrix precursor slip and wound onto a drum. The material was then cut along the axis of the drum and was removed and laid flat to form a prepreg tape. The plies needed to fabricate the required samples were then cut from these tapes. The plies were stacked together in the desired orientation in order to form panels with the required architectures. The panels were laminated in an autoclave. The organics in the laminated panels were pyrolized in a vacuum furnace, and the pyrolized preform was then infiltrated with molten silicon. The silicon reacted with carbon in the preform to form silicon carbide. The MI SiC matrix made in this fashion contains residual free silicon. After infiltration, excess silicon was cleaned off the surfaces of the samples by grit blasting with 220-grit alumina. No additional surface preparation was done to the test samples.

3.4 Test Methods

3.4.1 In-Plane Tension

The in-plane room-temperature tensile properties (**UTS, PL, E, ε**) were obtained through fast-fracture monotonic pull tests, as described in ASTM C1275. Test specimens that were 12.5 mm wide (0.5") were cut from the test panels. The gauge sections were then dog boned to a reduced width of 10 mm (0.4") by surface grinding with water-lubricated diamond tooling. The specimen geometry is given in Figure 2. An edge-

mounted clip-on extensometer measured the strain over a 25 mm (1") gauge section. The slope of the linear portion of the resulting stress strain curve is the modulus, **E**. For consistency, the modulus was typically taken over a stress range of 14-103 MPa (2-15 ksi). The **PL** was determined using the 0.005% strain offset technique. The maximum stress obtained was the ultimate tensile stress, **UTS**, and the strain at **UTS** was the failure strain, ε_f.

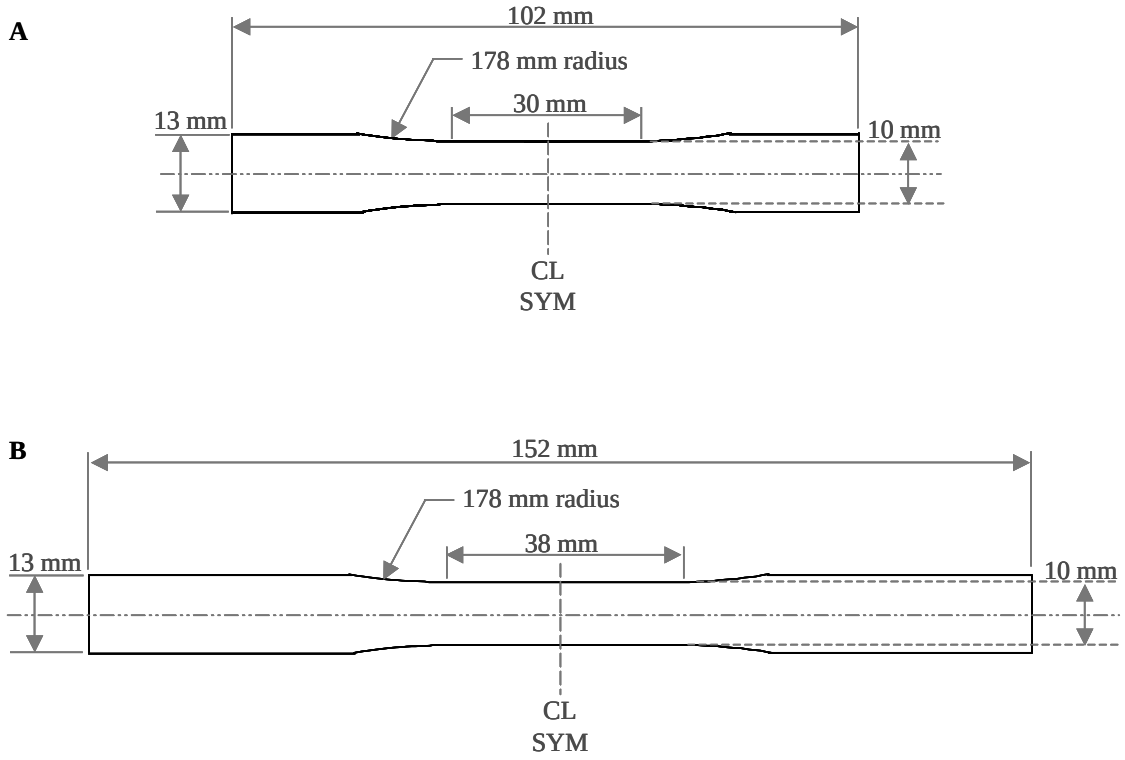

Figure 2. Specimen geometry for room temperature tensile tests (A) and 1315°C (2400°F) creep tests (B).

3.4.2 Interlaminar Shear

Interlaminar shear strength, ILS, was measured at Cincinnati Testing Laboratories, CTL Cincinnati, OH, using a double-notch compression test according to ASTM D 3846. One notch was cut on each broad face of a 12.5mm wide specimen. The distance between the notches on opposing faces was 63 mm (2.5"). The notch depth was

equal to one half the sample thickness. Loading the sample in compression until failure assessed the ILS of the composite mid-plane. The ILS was calculated by dividing the failure load by the mid-plane area of the composite between the two notches.

3.4.3 Room-Temperature Interlaminar Tension

The interlaminar tensile strength, ILT, also known as the flatwise tensile strength, of the composites was measured according to ASTM D 7291. Testing was performed at Cincinnati Testing Laboratories, CTL Cincinnati, OH. Metal studs were adhesively mounted to opposing faces of a flat CMC specimen. The studs and the CMC were then machined to a circular cross-section approximately 25 mm (1") in diameter. The ends of the two studs were then gripped and the CMC was pulled to failure. The ILT strength was calculated by dividing the load at failure by the cross-sectional area of the CMC. It should be noted that the quality of this test method is suspect, due to the possibility of edge defects in the CMC introduced during machining of test specimens.[44]

3.4.4 Residual Stress

Residual stress was measured using a layer removal technique similar to that used by Beyerle et al.[9] Three samples that were initially flat with the architecture (0-90-90-0:0-90-90-0) were surface ground using a diamond wheel to remove plies from each face until the resulting sample had the architecture (90-90-0-0). The ground samples were then polished with progressively finer diamond paste to reduce the possibility of grinding-induced surface stresses. 1-μm diamond paste was used for the final polish. If residual stresses are present in the 0 ply relative to the 90 ply (or in the 0 fiber relative to the remainder of the composite), then this non-symmetric sample will curl toward the ply that had been in residual tension prior to layer removal. For the 90-90-0-0 architecture, the thickness of the double 0 and double 90 layers are equal. Since the starting panel was flat, any residual stress in the 0 ply was opposed by an equal but opposite stress in the 90 ply. The residual stress is this case is given by equation 10.[9]

$$\sigma_R = \frac{E_0 I_0}{rwt^2}$$

where: E_0 = 0 ply modulus
I_0 = moment of inertia
r = radius of curvature
w = width
t = ply thickness

(10)

3.4.5 Measurement of the Coefficient of Thermal Expansion

The coefficient of thermal expansion, CTE, of the composite samples was measured using a LINSEIS L75D/1550 vertical dilatometer. This dual-pushrod dilatometer performed a differential measurement between the CMC samples and a platinum reference sample. An alumina sample holder and alumina pushrods were used. The composites were cut into specimens approximately 2 mm x 2 mm x 20 mm long. The samples were heated at a ramp rate of 5K/min over a temperature range from 200°C to 1350°C. Each sample was cycled twice without removal from the instrument, and the data from the second cycle was used for CTE determination. The secant CTE was calculated over the range of 200°C to 1300°C by dividing the expansion by the change in temperature.

3.4.6 Flexure Test Method

Four-point bend tests using one-third-point loading were carried out according to ASTM C1341. The samples were rectangular bars, 10 mm (0.4”) wide. The loading span was set at 32 times the sample thickness in order to reduce the risk of interlaminar failure. A deflectometer was used to monitor sample displacement at mid-span. The maximum surface strain was calculated from the displacement using equation 11.

$$e = \frac{4.7\,Dd}{S^2}$$

where: D = Deflection at beam center-point
d = sample thickness
S = outer support span

(11)

The maximum surface stress was calculated using the flexure formula, equation 12.

$$\sigma = \frac{SP}{bd^2} \qquad \text{where: } \begin{array}{l} S = \text{outer support span} \\ P = \text{load} \\ b = \text{sample width} \\ d = \text{sample thickness} \end{array} \qquad (12)$$

The flexure stress-strain curves were generated using the results of equations 11 and 12. **PL** was calculated in the same manner as for the tensile tests. The stress-strain curves produced in this manner are only valid in the linear-elastic region. At stresses above **PL**, the matrix is cracked, and the flexure formula no longer applies. For comparative purposes, ASTM C 1341 allows for the use of the entire flexure stress-strain curve based on the flexure formula.

3.4.7 In situ Cracking

In addition to measuring the mechanical response of the specimens tested in flexure, monitoring the progression of damage accumulation may improve the understanding of where cracks initiate in this material and how the material ultimately fails. A simple technique to monitor progressive cracking in the material would be to use intermittent loading, where a sample is loaded and unloaded to progressively increasing stress levels, with microstructural analysis between each loading cycle. However, un-broken fibers contract elastically when the composite is unloaded and in doing so tend to close matrix micro-cracks, making them difficult to observe. Additionally, the presence of compressive residual stresses acting on the matrix phase of MI SiC-SiC composites has been reported by Morscher.[12] A residual compressive stress on the matrix will enhance crack closure upon unloading. A technique where microstructural analysis is performed on loaded samples is therefore useful.

To verify which ply was cracking first in flexure for the architectures in Table V, samples were loaded in three-point bending on the stage of an optical microscope. The sample edge observed by the microscope was diamond polished prior to testing. A strain

gauge was mounted on each sample directly under the loading pin. In three-point bending, the stress peaks directly under the loading pin, making this the most probable location for the initial cracking event. Each sample was loaded to increasing strain levels, and optical microscopy was used to look for microcracking under load at each level. The interrupted loading was continued until the samples failed so that crack progression and crack saturation could be observed.

3.4.8 Creep Rupture 1315°C (2400°F)

The sample geometry was the dog-boned configuration shown in Figure 1. This specimen is longer than the room-temperature tensile specimen in order to allow the gauge section to be heated while keeping the grip area outside of the furnace. Testing was performed at CTL, using dead-weight test frames. The gauge section of the samples were heated in air to 1315°C in a SiC igniter furnace, loaded to the desired stress, and held at constant load until failure. Water-cooled MTS 5KIP hydraulic wedge grips were used to hold the samples and the strain was monitored over a 25 mm (1”) gauge length using a two probe water-cooled high-temperature contact extensometer.

3.4.9 Post-Test Characterization

The fracture surfaces of the failed specimens were examined in order to verify gauge failures. The gauge section of select failed samples was sectioned from the test coupons. This material was mounted in epoxy and diamond polished along the longitudinal edge of the composite. The mounted samples were interrogated using optical microscopy.

RESULTS AND DISCUSSION

CHAPTER IV

4.1 Microstructures for Various Fiber Volume Fractions

The fiber volume fraction of the CMC was varied by adjusting the prepregging conditions. In all cases, well-densified composites were achieved, but there were significant differences in the microstructures, as shown in Figure 3. As the fiber volume fraction decreased, the ply thickness increased. The samples with the highest fiber volume fraction have the most uniform microstructures. As the fiber volume fraction was diluted, the local packing of the fibers was largely unchanged, resulting in microstructures with bands of fiber interspersed with bands of un-reinforced matrix. To a large extent, the samples with lower fiber loading look like the high-fiber-volume-fraction samples with layers of matrix inserted between the plies. The fiber loading for each sample was approximated based on the nominal fiber diameter, the number of filaments per tow, the tow spacing in the prepreg, and the final ply thickness. Quantitative image analysis was performed on polished CMC mounts for two samples to spot-check the above approximation. Both techniques yielded similar results, validating the estimation based on sample thickness. The range of fiber loading achieved in this study was ~ 21 to 33%.

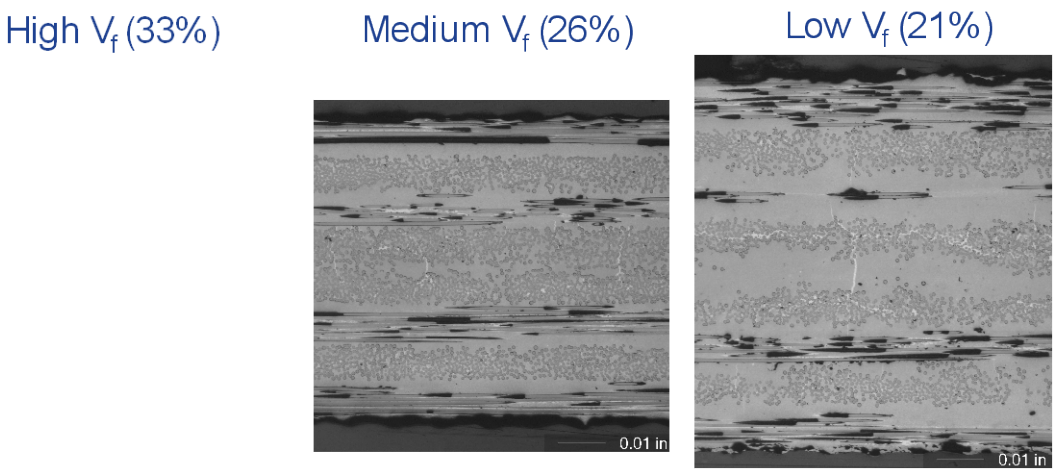

Figure 3. Microstructure of balanced-architecture CMCs produced at high V_f (left), medium V_f (center) and low V_f (right).

4.2 Room-Temperature Tension

The room-temperature stress-strain curves showed a strong influence of fiber volume fraction. Representative stress-strain curves are given in Figure 4. The average values for **PL, E,** and **UTS** for the balanced and unidirectional material are plotted as a function of fiber loading in the test direction in Figures 4 - 6. In the case of the balanced-architecture samples, the fiber loading in the test direction is one half that of the ply-level fiber content and therefore one half that of the unidirectional 0 composites.

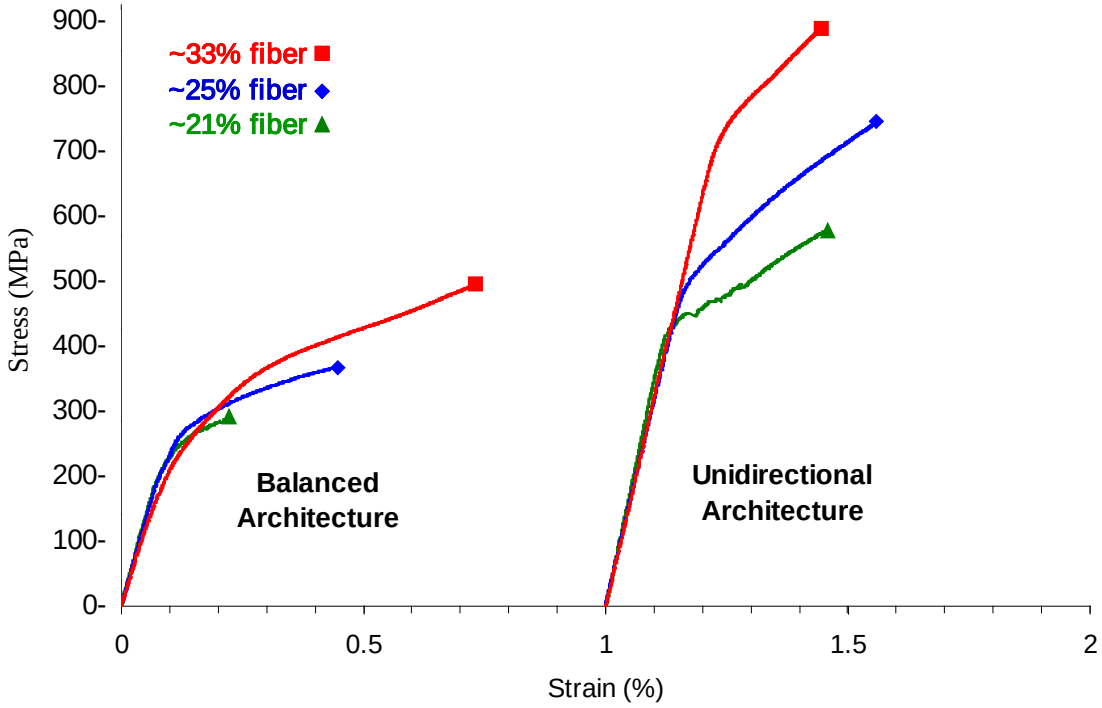

Figure 4. Stress-strain curves for balanced and unidirectional composites.

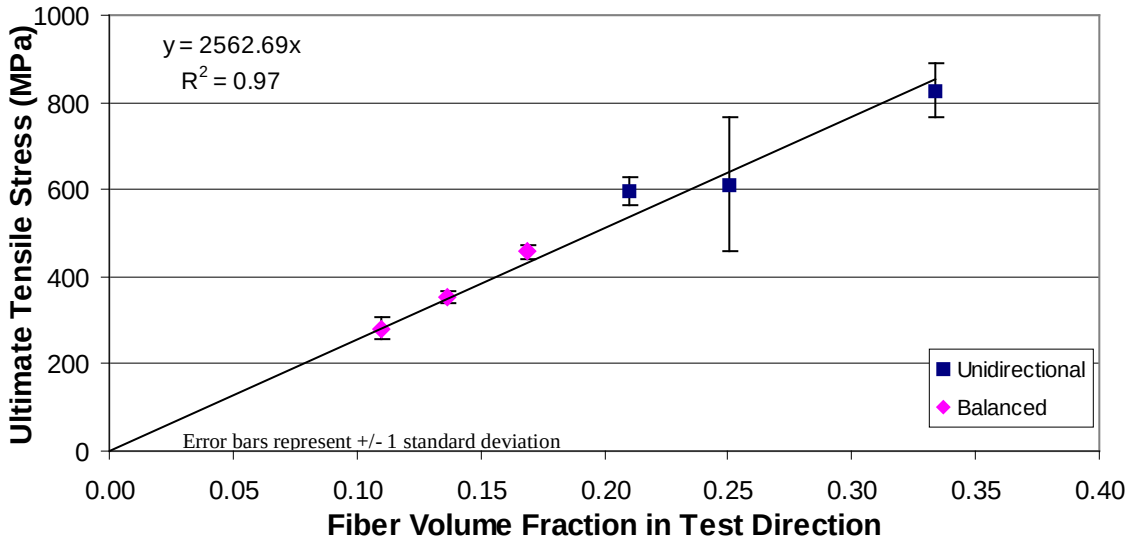

Figure 5. Effect of fiber volume fraction on ultimate tensile strength.

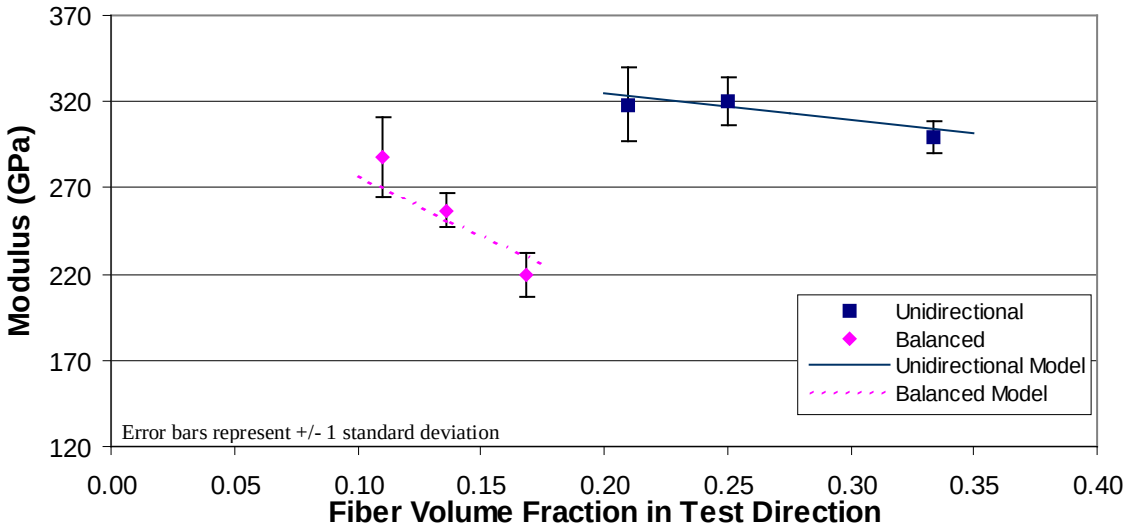

Figure 6. Effect of fiber volume fraction on modulus.

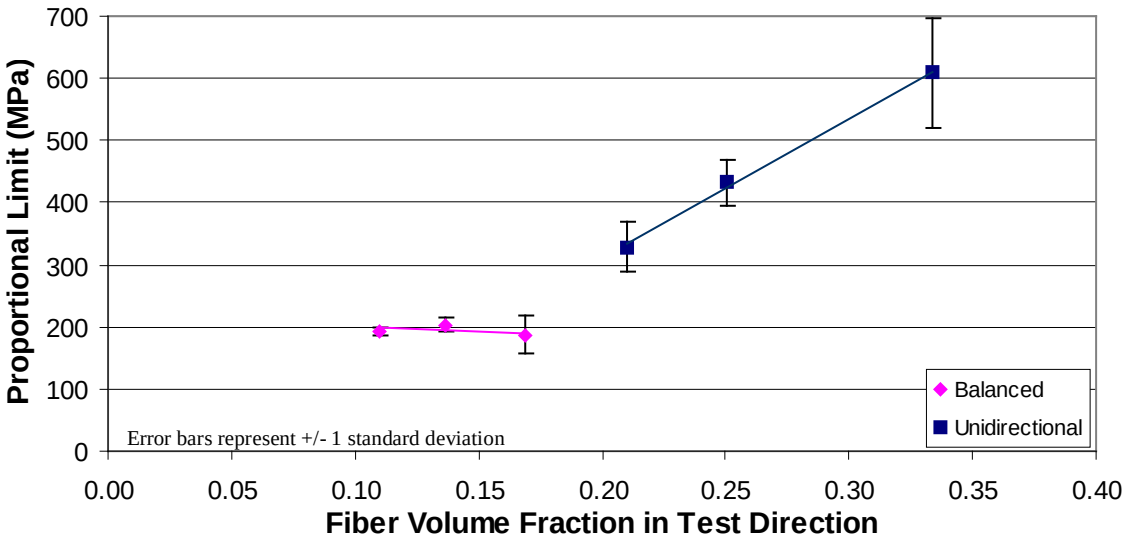

Figure 7. Effect of fiber volume fraction on proportional limit.

4.2.1 Ultimate Tensile Strength

In an ideal CMC, above the proportional limit the matrix is cracked, and the cracks are bridged by the fibers. When a crack spans the entire cross section of the specimen, the fibers carry the entire load, and the ultimate tensile strength is simply the

fiber strength multiplied by the volume fraction of fibers in the test direction. As predicted, the **UTS** of all the samples in this study scaled linearly with the directional fiber volume fraction, and the balanced and unidirectional samples followed a common trend line, as shown in Figure 5. The slope of this line is the fiber strength that was realized in the CMC, which in this case is 2.6 GPA, or 373 ksi. The vendor-reported-strength of the fiber lot used in this study is 2.6 to 2.8 GPa. The agreement between the fiber strength in the CMC and the vendor-supplied fiber strength should be treated as a coincidence, since the gauge length and number of filaments under load is different in the CMC compared to the fiber-tow tests and the statistical parameters of equation 1 are ignored.

4.2.2 Modulus

The modulus in the zero direction of unidirectional composites is expected to follow a simple rule of mixtures as described by equation 5. The matrix of the composite is a mixture of silicon carbide and silicon. It is also expected to follow a rule-of-mixtures relationship. The modulus of silicon is less than that of silicon carbide. The modulus of the matrix should therefore be lower than that of the stoichiometric SiC fiber, which has a vendor-supplied value of 380 GPa (55 MSI). The modulus of the boron-nitride-based coatings, however, is expected to be less than 10 GPa, much lower than SiC. Consequently, the modulus of the coated fiber is less than the modulus of the matrix, and the composite modulus is expected to decrease as the volume fraction of coated fiber increases. Over the range of fiber volume fraction explored in DOE I, the change in the unidirectional 0 composite modulus was less than 10%. Given this small change in modulus, as shown in Figure 6, the predicted trend cannot be cleanly observed due to scatter in the data. The DOE II unidirectional samples span a wider range of fiber loading, and this broader dataset follows the expected trend of decreasing modulus as $\mathbf{V_f}$ increases, as shown in Figure 8. By rule of mixtures, the modulus of the matrix, $\mathbf{E_m}$, is expected to be ~360 GPa (52 MSI), and the modulus of the coated fiber, $\mathbf{E_{cf}}$, is expected to be ~240 GPA (35 MSI). These values can be used to predict the modulus of a unidirectional composite, $\mathbf{E_0}$, using the rule of mixtures per equation 13.

$$E_0 = Vc_f\, E_{cf} + (1-Vc_f)E_m \qquad \text{where:} \quad \begin{array}{l} E_0 = 0 \text{ ply modulus} \\ V_{cf} = \text{coated fiber volume fraction} \\ E_m = \text{matrix modulus} \\ E_{cf} = \text{modulus of coated fiber} \end{array} \qquad (13)$$

For these samples, $\mathbf{V_{cf}} \sim 1.5\ \mathbf{V_f}$. The trend line from equation 13 is overlaid with the measured data in Figure 8. Using these values for $\mathbf{E_m}$ and $\mathbf{E_{cf}}$ tends to slightly over-predict the measured modulus.

The effect of fiber volume fraction on modulus is much greater for the balanced-architecture samples, as shown in Figure 6. The modulus of the 90 ply was calculated for each fiber loading using equation 6. The modulus of the balanced 0-90 composites can be calculated by a simple rule of mixtures using the modulus of the 0 and 90 plies. The moduli of the balanced composites from DOE I were calculated by combining the results of equations 6 and 13. These predictions compare well with the actual data, as shown in Figure 6.

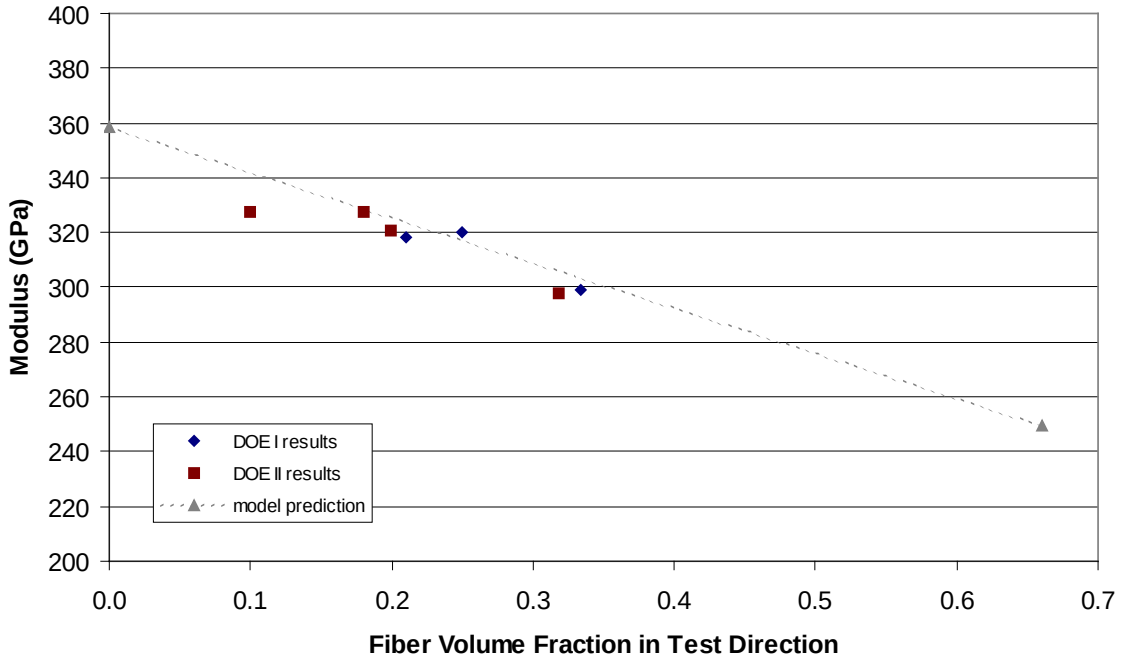

Figure 8. Unidirectional modulus as a function of coated fiber volume fraction. The average values from DOE I and II are plotted. Note: when $V_f = 0.67$, the coated fiber volume fraction =1.0.

4.2.3 Failure Strain

The reported modulus of the Type S fiber used in this study was ~380 GPa (55 MSI). As discussed earlier, the CMC **UTS** as a function of fiber volume fraction indicated that the fiber strength realized in the CMCs in DOE I was 2.6 GPa. Since the fiber is elastic, dividing this fiber strength by fiber modulus gives an entitlement fiber strain on the order of 0.7%.

The unidirectional samples from DOE I showed no significant trend between failure strain and $\mathbf{V_f}$, with a typical value between 0.5 and 0.6%. This is in reasonable agreement with the entitlement fiber strain and indicates that the composite is making effective use of the fiber. Unexpectedly, for the balanced-architecture samples, the failure strain decreased as the fiber volume fraction was reduced, as is apparent in Figure 4. One sample with a $\mathbf{V_f}$ of 0.22 had a failure strain of only 0.08%. Recall that, as shown in Figure 5, the **UTS** of all samples followed the trend predicted by fiber strength multiplied by fiber volume fraction. Therefore, the CMCs made with dilute fiber loading

still realized the same ultimate fiber strength as the samples with higher $\mathbf{V_f}$. Yet, these dilute samples achieved only a fraction of the failure strain. The same trend was evident in the unidirectional DOE II; failure strain dropped as fiber loading was decreased.

The fiber is elastic in nature, and an understanding of the strain in the fiber can be obtained from models that address its stress. The stress in the fiber is commonly described with a shear-lag model.[8,14-17] The stress in the fiber will spike at locations where the fiber is bridging a matrix crack. At a through-thickness crack, all of the load is carried by the fiber, and the fiber stress, σ_f , is simply the applied stress, σ_{app}, divided by the fiber volume fraction, $\mathbf{V_f}$. Moving away from the crack, load is transferred between the fiber and the matrix through the interfacial sliding friction, τ. The slip recovery length, **L**, is the distance required for the stress in a fiber bridging a crack to return to the far-field stress.[45] The far-field stress in the fiber is the applied stress multiplied by the ratio of the fiber and composite moduli. The relationship between **L** and τ can be determined by balancing the force acting axially on the fiber due to the applied load against the frictional force between the fiber and the matrix, as shown in Equation 14. These relationships are used throughout the literature.[16, 42, 45]

$$\sigma_f \pi R^2 = \pi 2 R L \tau \quad \text{or} \quad L = \sigma_f R / 2\tau \tag{14}$$

where: σ_f = fiber stress (at the crack)
τ = interface sliding stress
R = fiber radius E_m = matrix modulus
L = slip recovery length in absence of far-field stress

For a single matrix crack, the strain (or stress) distribution is shown in Figure 9. For the purpose of this discussion, the stress in the fiber bridging a crack will be assumed to be equal to the applied stress divided by the fiber volume fraction. At CMC failure, σ_f is equal to the **UTS** divided by $\mathbf{V_f}$. As was discussed in section 4.2 and shown in Figure 5, the **UTS** scaled linearly with $\mathbf{V_f}$, so that in general, for samples in this study, the peak stress or strain in a bridging fiber at CMC failure was relatively constant at ~ 2.6 GPa. Additionally, the fiber volume fraction was varied without changing the fiber coatings, so the interfacial properties, such as τ and **L**, should also be constant.

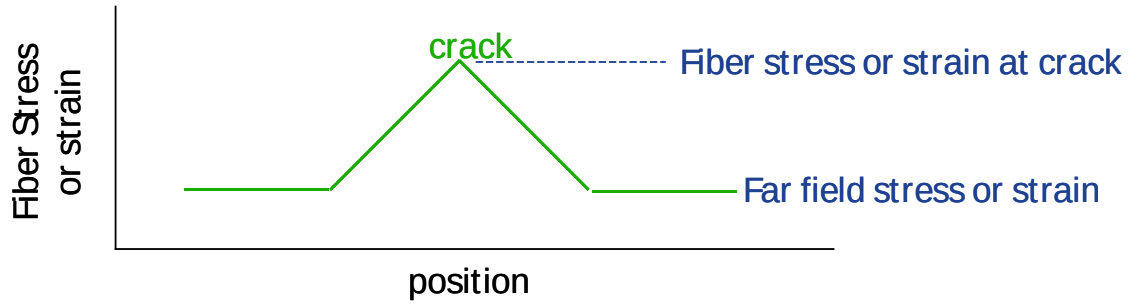

Figure 9. Fiber stress or strain distribution in the vicinity of a matrix crack.

Strain was measured in the tensile samples with an extensometer over a 25 mm (1") gauge length. The bulk strain will be the average fiber strain over the entire gauge length, and will therefore be dependent upon the number of cracks in that gauge length. As the matrix crack spacing, **Z**, decreases, the slip fields of neighboring cracks will overlap, the fiber will not return to the far-field stress/strain state, and the bulk strain in the composite will increase. This is the condition for which Curtin's strain model[14] (Equation 4) is valid for unidirectional material. Examples illustrating the effect of crack spacing on bulk failure strain (for fixed τ and **L**) are shown in Figure 10 as a fraction of the entitlement strain, normalized to 1.0 for this illustration. The ratios of **L** to **Z** in these examples are 3 (non-overlapping slip zones), 2 (no space between slip zones), and 0.5 (overlapping slip zones). When the slip zones overlap, a shielding effect limits the final crack spacing.[45] This final crack spacing is known as the saturation crack spacing, since even at increased loads the stress in the matrix (between the cracks) is low enough that no additional cracks will form.

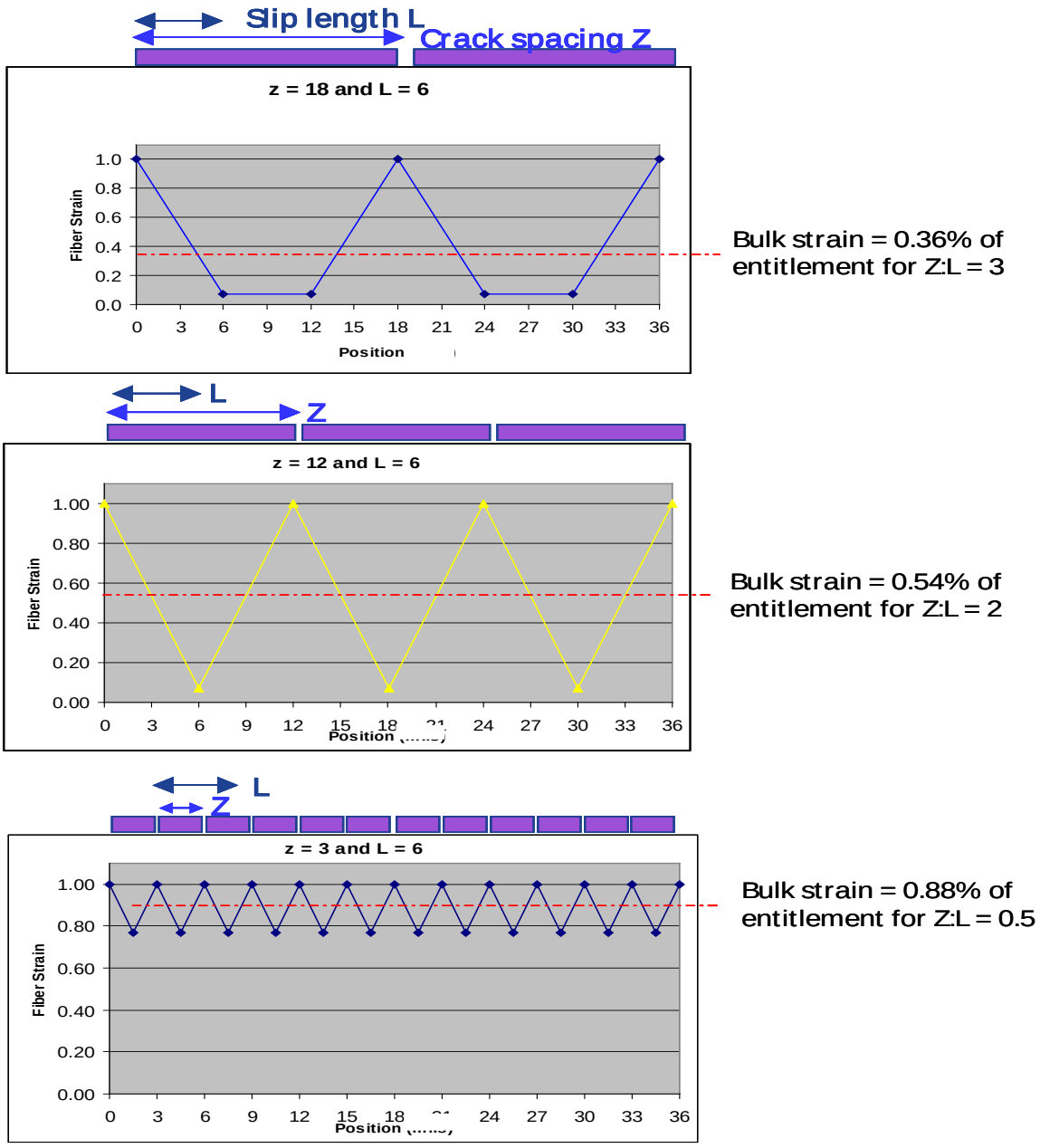

Figure 10. Examples showing the effect of crack spacing on the strain distribution for fixed L and τ. The dashed line represents the average strain.

It follows that the low-strain samples in this study should have a larger crack spacing than the high-strain material. The cracking of cross-ply laminates as described by Beyerle et al.[9] begins with cracks that span the thickness of the 90 plies, and which then tunnel through the cross section of the 90 ply before ultimately propagating into the 0 plies. The crack density may be different in the 0 and 90 plies, but the failure strain

should be dependent only upon cracks in the 0 plies, since those cracks are bridged by fibers. The 0 ply crack density was measured for a high-$\mathbf{V_f}$ sample and for a low-$\mathbf{V_f}$ sample that exhibited high and low failure strain respectively. The gauge sections of the test bars were removed and inspected for cracks using fluorescent dye penetrant. Unfortunately, the cracks in these samples were not visible with the dye penetrant technique. The gauge section was then mounted in epoxy, and the edge was polished in the longitudinal direction starting at the fracture surface. Optical microscopy revealed cracks in each sample, but the cracks were only apparent near the fracture surface. The cracks were increasingly difficult to find as the distance from the fracture surface increased, and were not visible optically 2 mm from the fracture surface. It is likely that many of the matrix cracks close upon unloading when fibers that bridge the cracks contract elastically. Examples of the cracks visible optically are shown in Figure 11. These images are from a balanced-architecture sample with a fiber loading of 33% and a large failure strain of 0.7%. The upper image shows the entire cross section of the sample starting at the fracture surface. The region outlined in the upper image is shown with greater resolution in the lower image, where the arrows point to fine matrix cracks. Additional matrix cracks were visible using SEM at a magnification of 8000x. However, at this magnification, it is impractical to splice together enough images to determine the crack density, and another technique is needed.

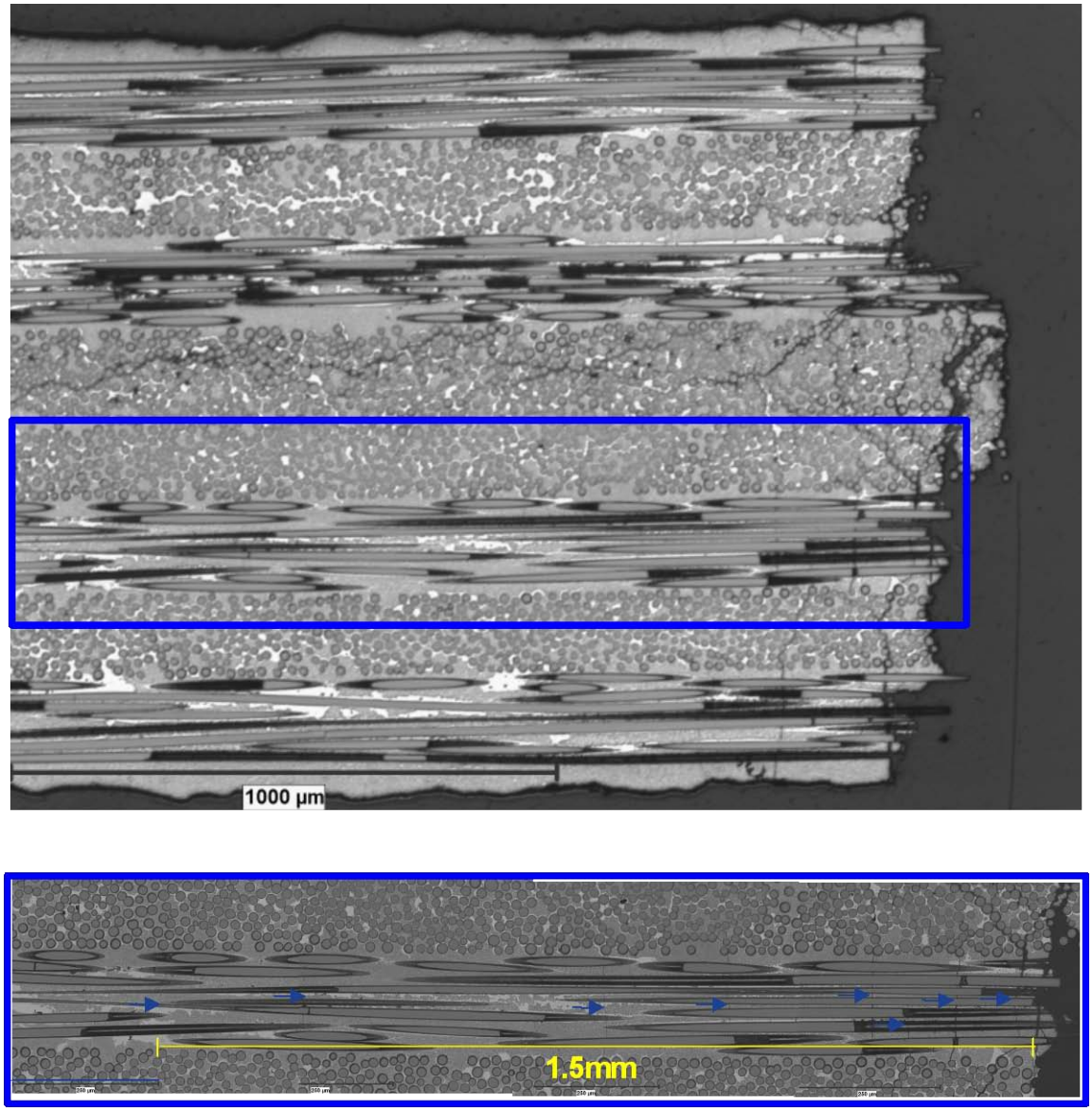

Figure 11. Optical micrographs that show cracks in a failed specimen.

The failed samples were observed under load in order to re-open the cracks. The gauge section of the failed specimens was cut from the test bar, and the longitudinal edge was polished. A strain gauge was mounted to the broad face of the sample, and it was loaded in three-point bending on the stage of an optical microscope. As long as the surface strain measured by the strain gauge in three-point bending is below the tensile failure strain of the previously tested CMC, then no new cracks should be introduced. Once the sample was loaded, many previously unseen cracks were visible at only 0.1% strain. These cracks became more apparent as the load was increased. No audible

cracking was heard during the loading process, and no additional cracks were seen as the surface strain was increased. The observed crack density in the outer zero ply was ~100 um (4 mils) as shown in the upper portion of Figure 12. This image was taken at a surface strain of 0.3%. The crack density in a low $\mathbf{V_f}$ sample with 21% fiber and a failure strain of only 0.3%, as measured in the same manner, was ~ 300 um (12 mils) as shown in the lower image of Figure 12. The difference in failure strain for these two samples is consistent with the difference in crack density.

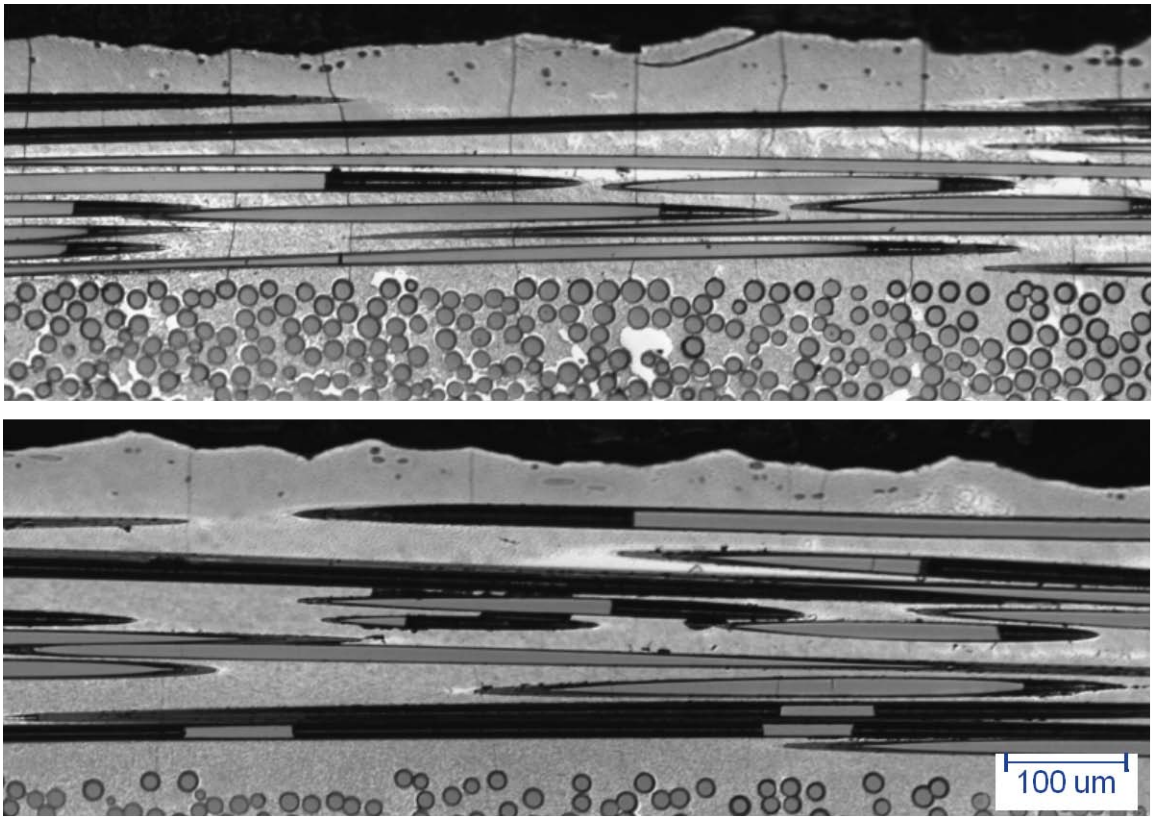

Figure 12. Optical micrographs showing the crack densities in the outer 0 ply of previously failed tensile specimens. The cracks are being held open in a three-point bend fixture. The specimen in the upper image, had $V_f = 0.33$ and e = 0.7%. The lower image had $V_f = 0.22$ and e = 0.3%.

To understand why, for dilute fiber loadings, an increase in $\mathbf{V_f}$ would lead to an increase in matrix cracks and therefore failure strain, it is useful to start with the case where the **UTS** based on $\mathbf{V_f}$ $\boldsymbol{\sigma_f}$ is equal to the matrix cracking stress. For the purpose of this illustration, the simplifying assumption will be made that cracks run through the

entire cross section of the sample. When the matrix cracks, the load that the matrix was carrying is transferred to the fiber. In this example, the stress in the fiber at the crack equals the fiber **UTS,** and the composite fails. Locally, where the fiber bridges the crack, the strain in the fiber may reach the entitlement strain, but the bulk strain measured over a 25mm gauge length will be essentially equal to the far-field strain. Consistent with the results of DOE I, if the assumption is made that for the balanced architecture CMC the composite stress at **PL** does not change as a function of fiber loading, then, as more fibers are added to the composite, the difference between the **PL** and **UTS** will increase. In this example, when the matrix cracks, the fibers can carry the extra load. As the load is further increased, the far-field stress in the matrix will continue to increase until either a second matrix crack forms or the stress in the bridging fibers exceeds the fiber **UTS**. If the $\mathbf{V_f}$ and the **UTS** are high enough, this process will continue until the saturation crack spacing is reached.

For the medium- and low-$\mathbf{V_f}$ samples in the present study, matrix crack saturation is not reached due to the reduced **UTS**. Even at these volume fractions, however, it should be possible to increase failure strain through any combination of the following parameters.

a) **Fiber strength**. There is still considerable variation in the strength of the starting fiber. Fiber with higher strength will produce a composite with higher **UTS**, which would offset the effect of reduced fiber loading.

b) **Flaw population.** A larger population of critical defects in the matrix would allow matrix cracks to form at lower stresses, thereby allowing the saturation crack spacing to be reached at a lower composite **UTS**. These defects could be porosity or clusters of fiber.

c) **Interfacial sliding friction, t**. For a given crack spacing below the saturation value, the strain should vary inversely with τ. If τ is decreased, the slip length will increase per Equation 14, causing an increase in the average fiber strain.

4.2.4 Measurement of τ and Γ_m

Figure 13 shows the stress-strain curve for a high-$\mathbf{V_f}$ unidirectional CMC that reached crack saturation. For stress-strain curves with the general shape of those in Figure 13, matrix cracking commences at **PL** and saturates at the increase in modulus denoted as σ_s.[16] Ideally, the composite modulus after saturation will be equal to the modulus of the fibers multiplied by the fiber volume fraction. However, due to fiber breakage, the actual modulus is likely to be reduced.[46] For the sample in Figure 13, the modulus after σ_s is 74 GPa, compared to an $\mathbf{E_f}$ $\mathbf{V_f}$ value of 125 GPa. Once the saturation crack spacing, **Z**, and the saturation stress, σ_s are known, then τ and Γ_m can be determined using Equations 15a[47] and 15b.[48]

$$\Gamma_m = \left(\frac{Z_s}{\chi R}\right)^3 \left[\frac{V_f \tau E_0 R}{(1-V_f)E_f E_m}\right] \qquad (15a)$$

$$\tau = \left[\frac{\sigma_s R E_m (1-V_f)}{Z_s V_f E_l}\right] \qquad (15b)$$

where:
V_f = fiber volume fraction
E_0 = 0 ply modulus
E_m = matrix modulus
E_f = fiber modulus
Z_s = saturation crack spacing
R = radius of fiber
$\chi \approx 1.6$

For the sample shown in Figure 13, based on σ_s = 570 MPa and $\mathbf{Z_s}$ = 110 um, τ and Γ_m are calculated to be ~52 MPa and 36 J/m^2 respectively. This value of Γ_m is reasonable compared to the range reported for various silicon carbides.[49]

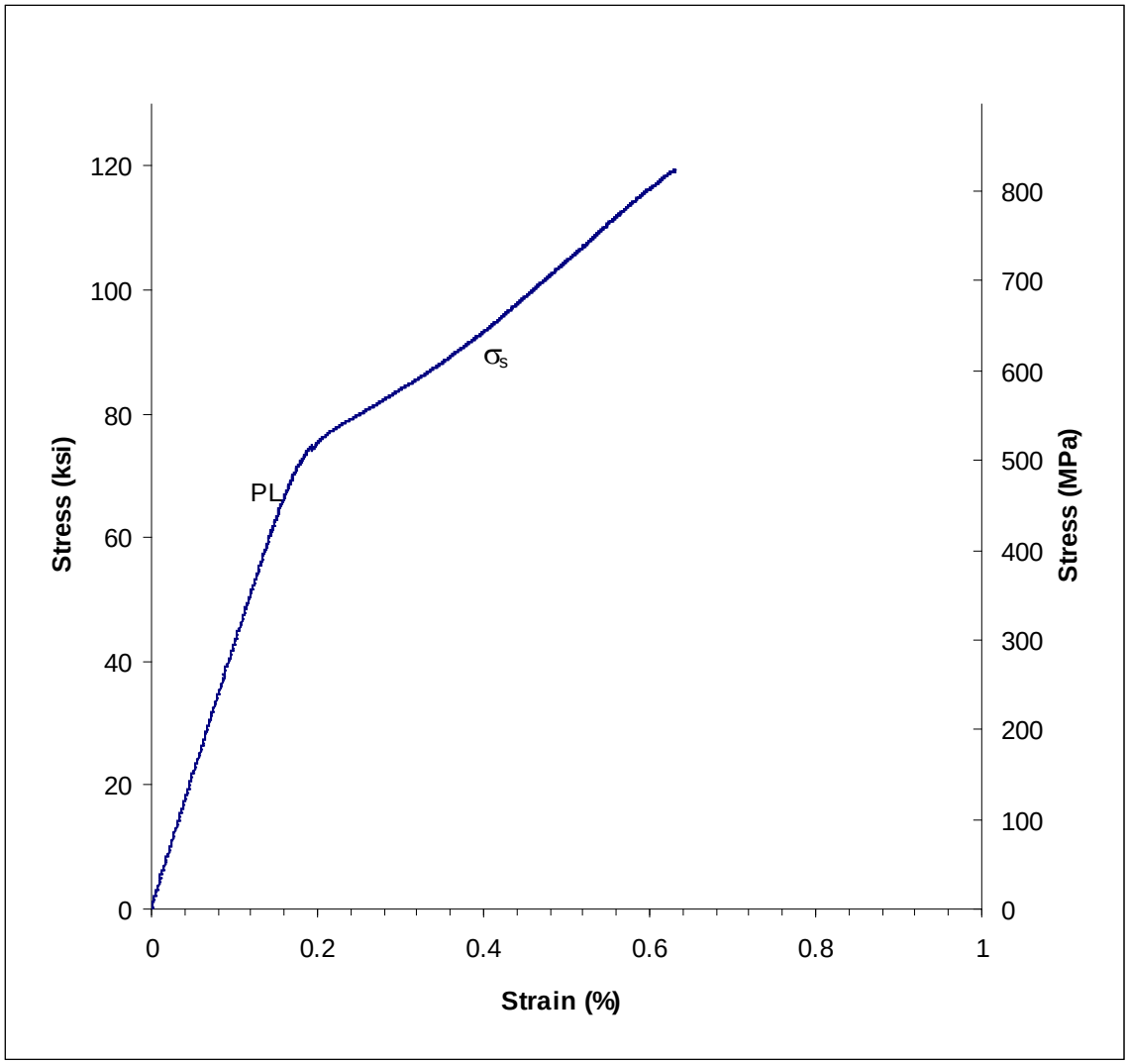

Figure 13. Unidirectional stress strain curve showing proportional limit and saturation cracking stress.

4.2.5 Proportional Limit

Changing fiber volume fraction had different effects on the **PL** of balanced and unidirectional composites, as shown in Figure 7. As $\mathbf{V_f}$ increases, the **PL** of balanced architecture material remains essentially unchanged, while the **PL** of unidirectional material increases. The balanced samples had test direction fiber volume fractions between 10 and 17%, while the unidirectional samples ranged from 20-35 %. In order to evaluate the unidirectional and cross-ply laminates over the same range of fiber loading,

the DOE II series of panels was fabricated. The resulting samples had fiber volume fractions in the test direction similar to that of the balanced-architecture specimens.

As $\mathbf{V_f}$ increased from ~10 to 35%, the unidirectional **PL** increased in a nearly linear fashion. This increase is predicted by Equation 2. Values for the terms in this model were obtained in order to compare its prediction to the experimental results. $\boldsymbol{\tau}$, $\boldsymbol{\Gamma_m}$, $\mathbf{E_m}$ and the relationship for $\mathbf{E(V_f)}$ (eq 13) were taken from the results given above in sections 4.2.4 and 4.2.2. The vendor-supplied values of fiber radius and modulus were used, which are 6.5 um and 380 GPa respectively. The term $\boldsymbol{\phi}$ in Equation 2 compensates for residual stress acting on the matrix. MI CMCs are fabricated at high temperature, above the melting point of silicon. Chemical reactions and phase changes that occur at temperature, as well as CTE mismatches between the various constituents, can result in residual stress in the composite at room temperature. The residual stress in the HiPerComp® CMC as measured on three samples using the layer-removal technique ranged from 7 to 28 MPa (1-4 ksi) of compressive residual stress acting on the matrix relative to the fiber.

Figure 14 shows the **PL** results for the unidirectional material along with the model trend line based on Equation 2. The experimental results are in good agreement with the model. Equation 2 predicts a lower bound for the stress at which pre-existing matrix cracks with length greater than $\mathbf{a_0}$ will propagate. The agreement between the experimental data and Equation 2 implies that flaws of length $\geq$ $\mathbf{a_0}$ are present. This critical flaw size can be estimated using Equation 16.[48] Populating Equation 16 with the same values used in Equation 2, indicates a critical flaw size of less than 1 um. It seems reasonable that flaws of this size would be plentiful in the CMC microstructure, as it is much smaller than the typical microstructural features such as the 13 um diameter fiber or the pockets of free silicon.

$$a_0 = \frac{1}{2} E_m \Gamma_m^{1/3} \left[\frac{(1-V_f)^2 R(1+(E_f V_f / E_m(1-V_f))}{\tau V_f^{\,2} E_f} \right]^{1/3} \quad (16)$$

where:
V_f = fiber volume fraction
E_f = fiber modulus
E_m = matrix modulus
Γ_m = matrix fracture energy
τ = interfacial sliding friction
R = radius of fiber

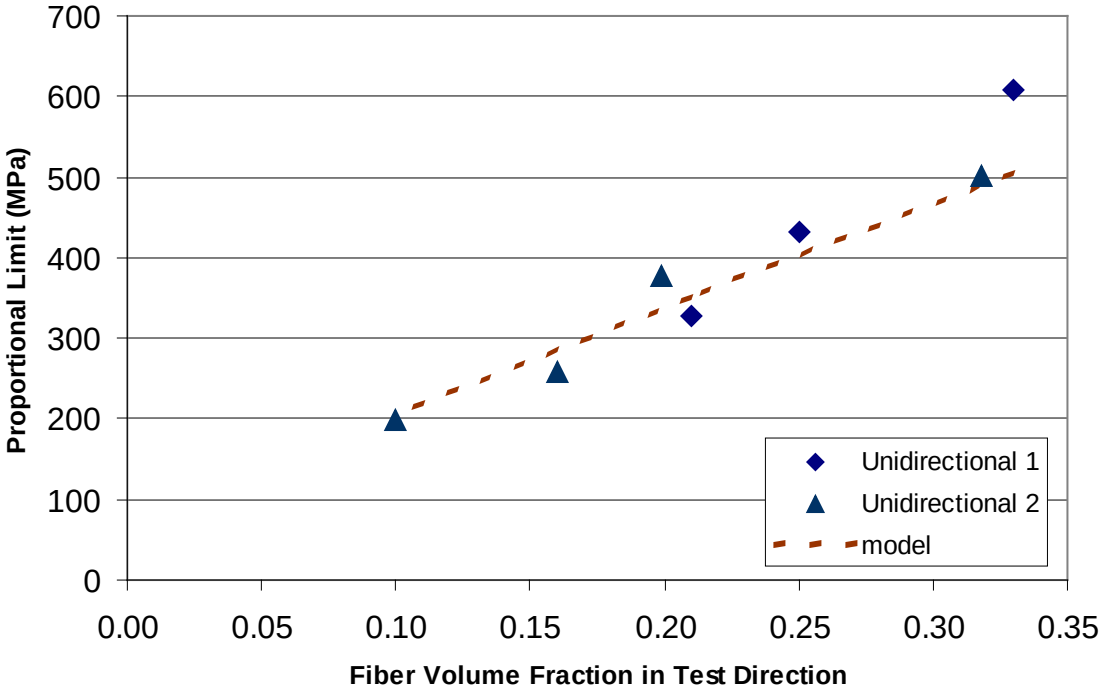

Figure 14. Unidirectional samples from DOE I and II with the trend predicted by Equation 2.

DOE II also compares a balanced architecture sample, (0-90-0-90)s to a unidirectional sample where the cross plies were replaced with matrix-only plies of comparable thickness, (0-M-0-M)s. The resulting room temperautre stress-strain curves and properties are given in Figure 15. The modulus of the (0-M-0-M)s specimen is higher than the balanced sample, because the matrix modulus is approximately twice that of the 90 ply. The **PL** of the unidirectional sample is also higher, because the matrix is stronger than the 90 ply. These samples clearly demonstrate how the 90 ply reduces composite modulus and **PL,** and support the hypothesis that the 90 plies crack before the 0 plies.

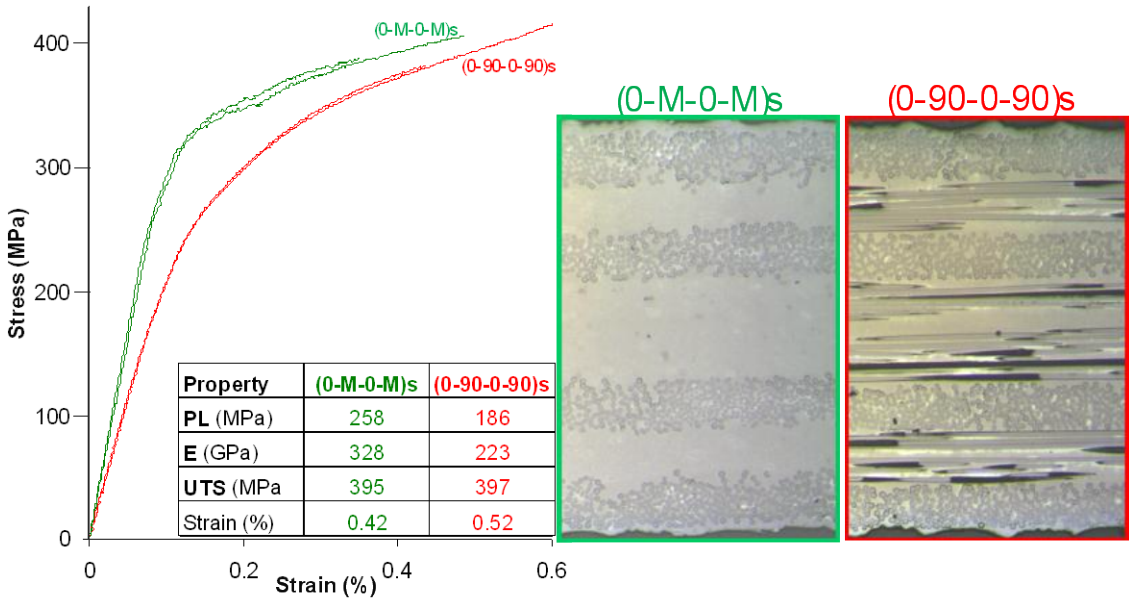

Figure 15. Stress-strain curves for a balanced-architecture sample and a corresponding sample where the cross plies were replaced with matrix-only plies.

4.2.6 Tensile Ply Level Properties

Despite the improvement in unidirectional **PL** with increased fiber loading, increasing the fiber volume fraction did not have an appreciable effect on **PL** for balanced-architecture samples. The reason is, that in a cross-ply CMC, the 90 plies are expected to crack first,[9] as was demonstrated in Figure 15. The stress in the 90 ply at **PL** can be calculated based on its modulus, $\mathbf{E_{90}}$, relative to the composite modulus, $\mathbf{E_C}$. Assuming a uniform strain condition in the tensile test, the stress in the 90 ply, σ_{90}, can be obtained by multiplying the composite strain by $\mathbf{E_{90}}$. Alternatively, it is equal to the composite stress multiplied by the ratio $\mathbf{E_{90}}$ / $\mathbf{E_C}$. The stress in the 0 ply, σ_0, can be obtained in the same manner. Table VI lists the average moduli and ply-level stresses at **PL** for the DOE I samples.

Table VI. Ply Level Stresses for DOE I Samples

Architecture	Fiber Vol. Frac.	Modulus (GPa)			Stress at Proportional Limit** (MPa)		
		composite	0 ply	90 ply	composite	0 ply	90 ply
unidirectional 0	0.33	299	299	NA	545	545	NA
balanced 0:90	0.33	220	299*	140	187	255	119
unidirectional 0	0.25	320	320	NA	432	432	NA
balanced 0:90	0.25	257	320*	194	203	252	153
unidirectional 0	0.21	318	318	NA	329	329	NA
balanced 0:90	0.21	288	318*	257	193	214	173

*from unidirectional 0 sample **based on 0.005% offset

For the balanced specimens, at **PL**, the stress in the 0 plies is much less than the **PL** stress of the unidirectional 0 material. By extension, the stress in the 90 ply at **PL** can therefore be interpreted as the cracking strength of the 90 plies. This result validates the expectation that the 90 plies crack first in the cross-ply laminates, and therefore the 90 plies control the **PL** of the composite. As shown in Table VII, the strength of the 90 plies is decreasing as $\mathbf{V_f}$ increases. This decrease is consistent with the microstructures shown in Figure 3. As $\mathbf{V_f}$ is increased, the inter-ply bands of matrix-rich material are being removed. Compared to the 90 plies, the matrix has higher modulus and higher strength. It follows that the modulus and strength of the 90 ply will decrease as these matrix bands are removed.

4.2.7 Effect of 90 Ply Thickness and Stacking Sequence on Proportional Limit

The ply thickness **t** decreased as $\mathbf{V_f}$ was increased in DOE I. However, due to the banded microstructure, the thickness of the fiber-rich portion of the 90 ply was essentially unchanged. The **PL** model presented in Equation 3 assumes a pre-existing flaw that spans the width of the 90 ply. With the banded microstructure, it is possible that the effective ply thickness may be the width of the dense fiber band. This presents uncertainty in the value of **t** to be used in Equation 3. Additionally, for the DOE I samples, the values of $\mathbf{E_{90}}$, **g(x)**, and $\mathbf{\Gamma_{90}}$ all change with fiber volume fraction. The fracture energy of the 90 ply, $\mathbf{\Gamma_{90}}$, was not measured, and there would be a great deal of

uncertainty in estimating it. Given this scenario, the samples from DOE I are not optimum for assessing the applicability of Equation 3 to the HiPerComp® SiC-SiC system.

DOE III consists of a series of three panels that were made to critically test Equation 3. For these panels, the ply thickness was varied by a factor of two while maintaining a constant fiber volume fraction. Three 8-ply samples were made with three different ply thicknesses, the microstructures of which are shown in Figure 16. The banding of the microstructure observed in DOE I is apparent in these samples as well, with the thinnest sample having the most uniform microstructure. The fiber bands in the intermediate sample tend to be tight, but there are still regions where the 90 fibers span the entire width of the 90 ply. For the thickest sample, the fiber tends to be dispersed across the thickness of the 90 ply, and even the double 90 ply at the mid-plane has large regions were the fibers from the two adjacent 90 plies become nearly indistinguishable from each other. These microstructures show that the 90-ply thickness of the thick sample is ~ 2x that of the thin sample. For this series of samples, the only term changing in Equation 3 is the ply thickness, and Equation 3 therefore predicts a 40% change in **PL**. However, as shown in Figure 17, the results did not show much of an effect of ply thickness on **PL**. The diamonds are the measured **PL** from tensile bars. The squares and trendline show the predicted **PL** based on Equation 3, normalized to the intermediate ply thickness.

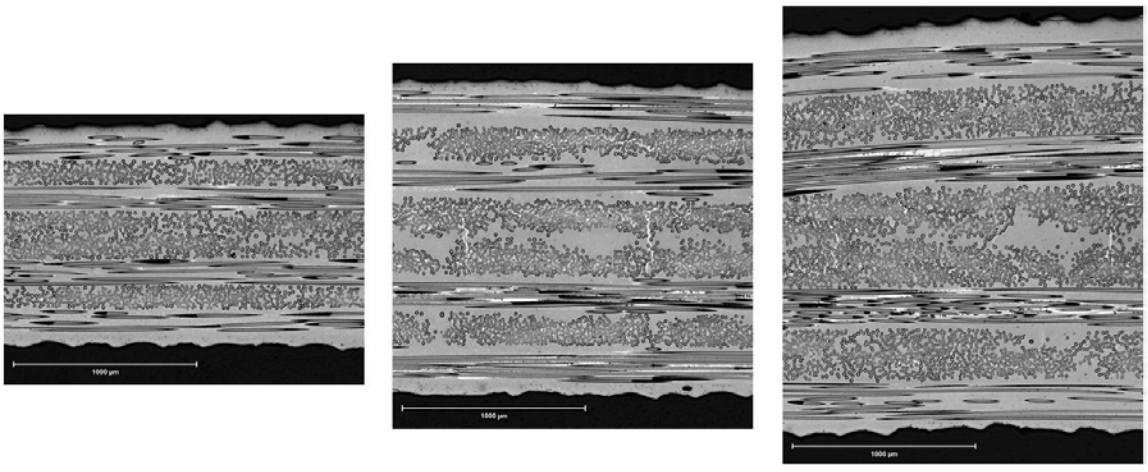

Figure 16. Microstructures of CMC samples made with medium -V_f at three different ply thicknesses.

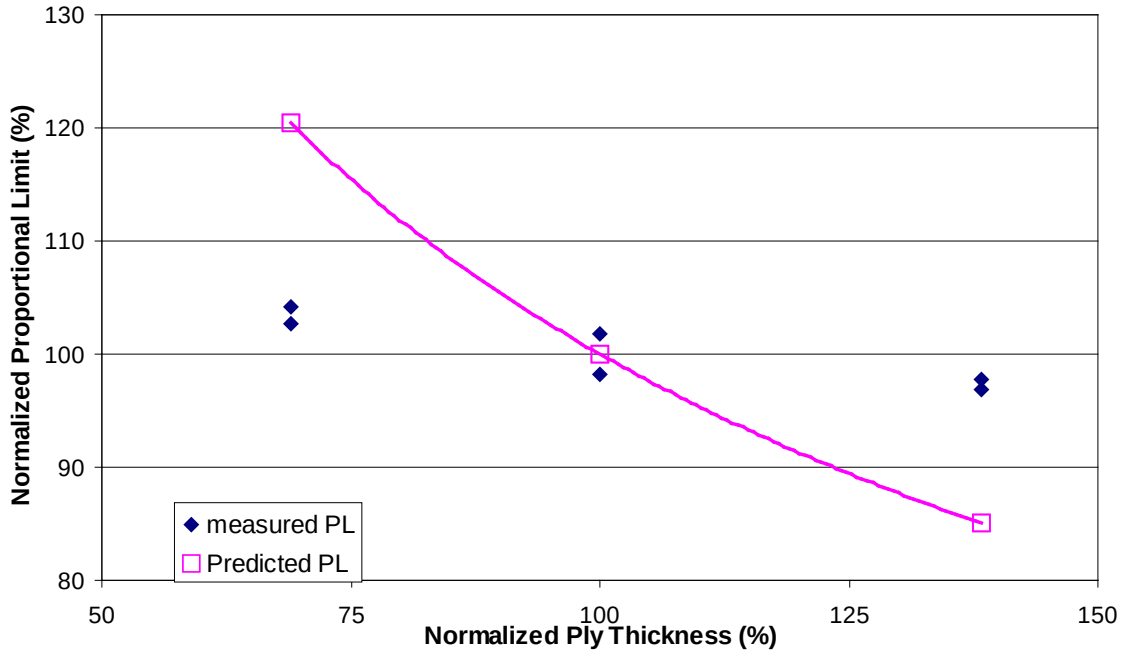

Figure 17. Effect of ply thickness on PL at a constant fiber loading. PL and thickness have been normalized to allow comparison to model predictions.

The limited data shown in Figure 17 does not show the expected relationship between **t** and **PL**. In addition to the ply thickness changing, the sample volume was also changing in these samples. Through stacking sequence variation, the effective ply thickness can be changed while maintaining both a constant fiber loading and a constant sample volume. For example, microstructurally, two adjacent 90 plies will look very similar to a single 90 ply with twice the nominal ply thickness. The effective ply thickness was changed by a factor of 6 by varying the stacking sequence in DOE IV, as shown in Table IV. For these panels, the high fiber loading was used, as it is the least prone to have bands of un-reinforced matrix between the fiber plies. Micrographs showing the different clusters of 90 plies are given in Figure 18. There are no significant inter-ply matrix-rich bands, and the clusters of adjacent 90 plies are therefore expected to behave as a single ply of greater thickness.

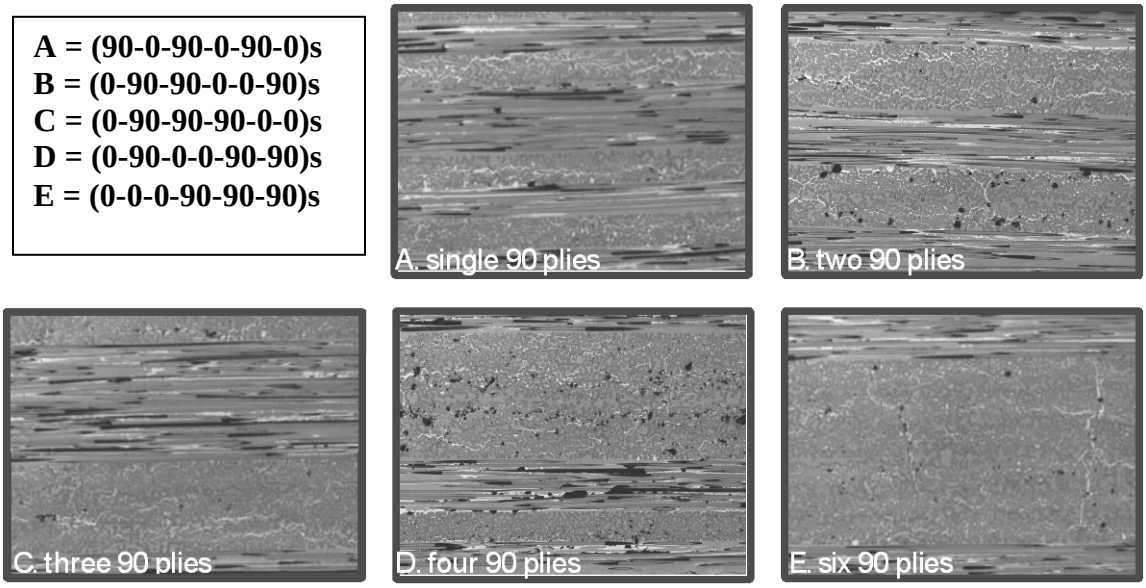

Figure 18. Microstructures for samples with different numbers of adjacent 90 plies are shown.

Four room-temperature tensile tests were performed on specimens from each panel. Examples of the stress-strain curves are shown in Figure 19. Equation 3 predicts a change in **PL** of ~ 2.5x as the ply thickness varies by a factor of 6. However, as shown in Figure 20, there was no trend between stacking sequence and **PL,** and there are no obvious differences between the stress-strain curves from all the stacking sequences. In Figure 20, the diamonds are the measured **PL** data points and the squares are the values predicted using Equation 3, normalized against the double 90-ply thickness.

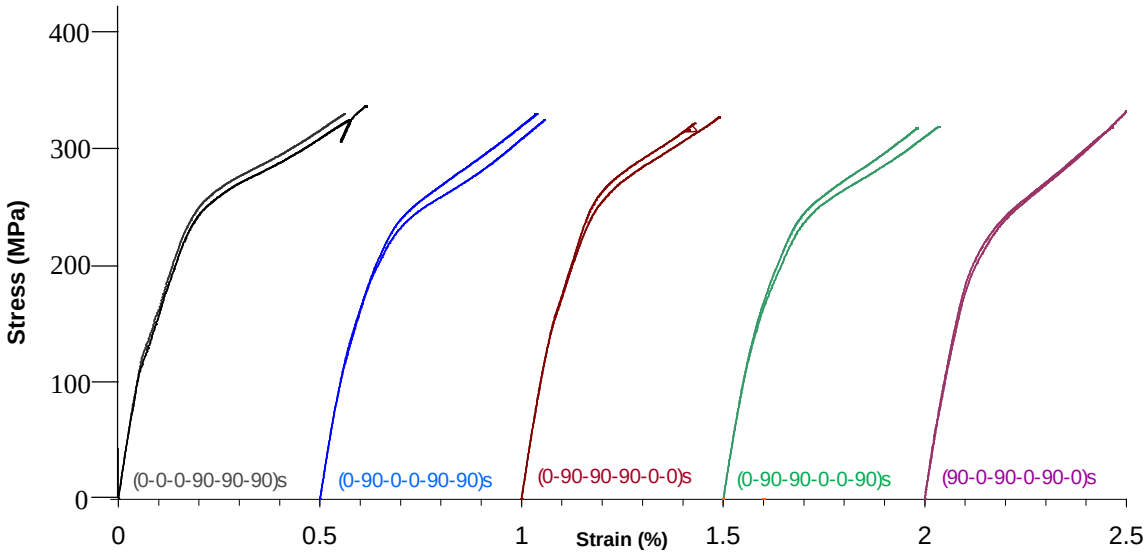

Figure 19. Stress-strain curves for the stacking sequences of DOE IV.

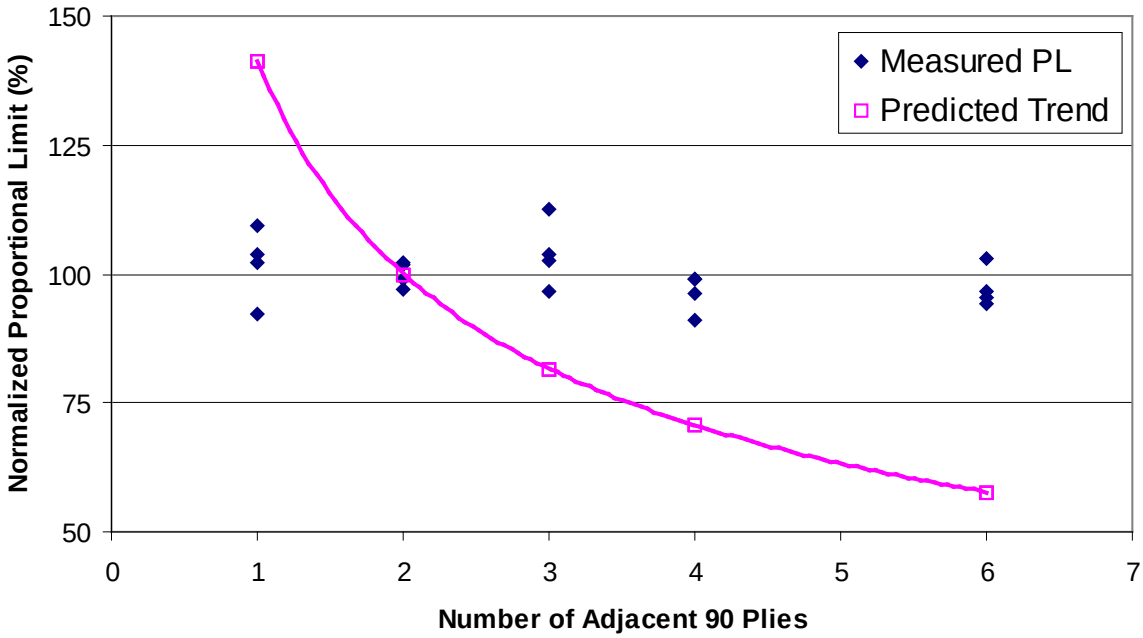

Figure 20. The effect of stacking sequence on proportional limit.

The **PL** for this series of samples is somewhat low as compared to DOE III. This is likely due to porosity in the samples. The micrographs in Figure 18 show a range of porosity that can be found in each of the samples. That is, while micrograph 18A shows a low level of porosity for the single 90-ply sample, there are regions in that sample that have porosity similar to what is shown in micrograph 18D, the four 90-ply sample. All of

these samples were processed together using the same starting materials and have qualitatively similar porosity levels. The result suggests that for these samples the **PL** is being controlled by porosity, not ply thickness. Additionally, consistent with Figure 18, the pore size was never observed to be equal to or greater than the effective 90-ply thickness.

This outcome, coupled with the results from DOE III, which also did not show the predicted ply thickness effect, demonstrate that the assumption of pre-existing flaws that span the width of the 90 ply is not valid in the HiPerComp® prepreg MI SIC-SiC system. In this system, the fiber and the matrix are both based on silicon carbide, and therefore they have well-matched thermal properties. The result is that this system has only a small amount of post-processing residual stress. As was discussed above, the residual stress that is present puts the matrix and the 90 ply in slight compression, making it unlikely that the matrix will be micro-cracked after processing. Therefore, the assumption of a pre-existing flaw that spans the width of the 90 ply is unlikely to be true. In the case of the glass matrix composites for which Equation 3 has been validated, due to CTE mismatch, the matrix is in residual tension relative to the fiber, making it more likely that the matrix will be microcracked after processing.

The matrix cracking of the cross-ply HiPerComp® CMC should still be based on the presence of flaws, and it is proposed that it should be treated like monolithic ceramics using Weibull statistics. The fibers, or clusters of fibers, in the 90 ply are likely to act as flaws that initiate matrix cracks when loaded. This concept will be discussed in more detail in section 4.4.

4.3 Interlaminar Properties

The interlaminar tensile and shear results for the CMC with different fiber loading are shown graphically in Figure 21. Fiber volume fraction did not appear to impact the interlaminar properties, although there is a lot of scatter in the data. This result again ties into the banded microstructure of Figure 3. The fracture surfaces from the interlaminar tests all show fiber rich planes, and there are no matrix rich areas visible. The BN based coating on the fiber provides a weak interface that will fail when the CMC is loaded interlaminarly. Failure is expected to occur along planes that have a high density of fiber

and therefore fiber coating. Because the local fiber packing in the fiber-rich bands is similar regardless of fiber loading, the interlaminar tensile and shear properties of the CMC are also similar. This outcome would likely be different if the fibers were well dispersed at the lower fiber loadings.

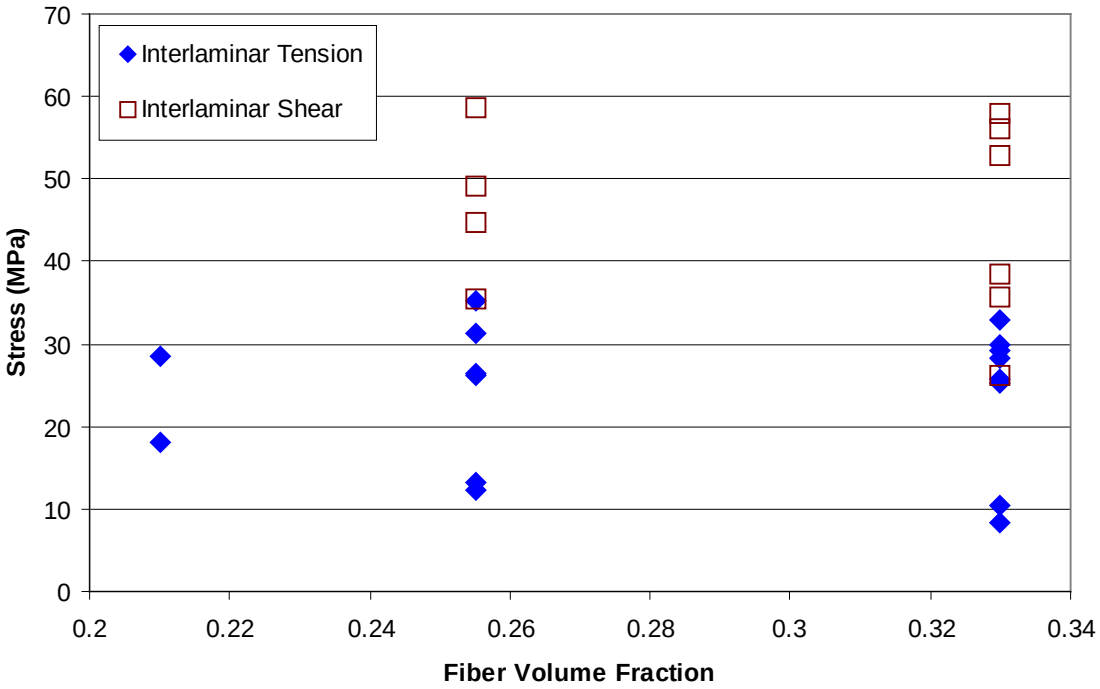

Figure 21. Interlaminar properties at the medium and high fiber loading.

4.4 Ply-Level Behavior

In section 4.2.5, it was shown that fiber volume fraction did not have a substantial effect on the **PL** of cross-ply CMCs. It was also shown that the **PL** of unidirectional CMCs can be 2-3 times that of the balanced-architecture material. DOE V was designed to determine whether the high **PL** of the unidirectional material can be realized locally in a cross-ply composite. Specimens from the Flex DOE V panels were tested in tension. The tensile stress-strain curves are shown in Figure 22. Similar to DOE IV, the stacking sequence had little effect on the tensile stress-strain response of the 2:1 samples.

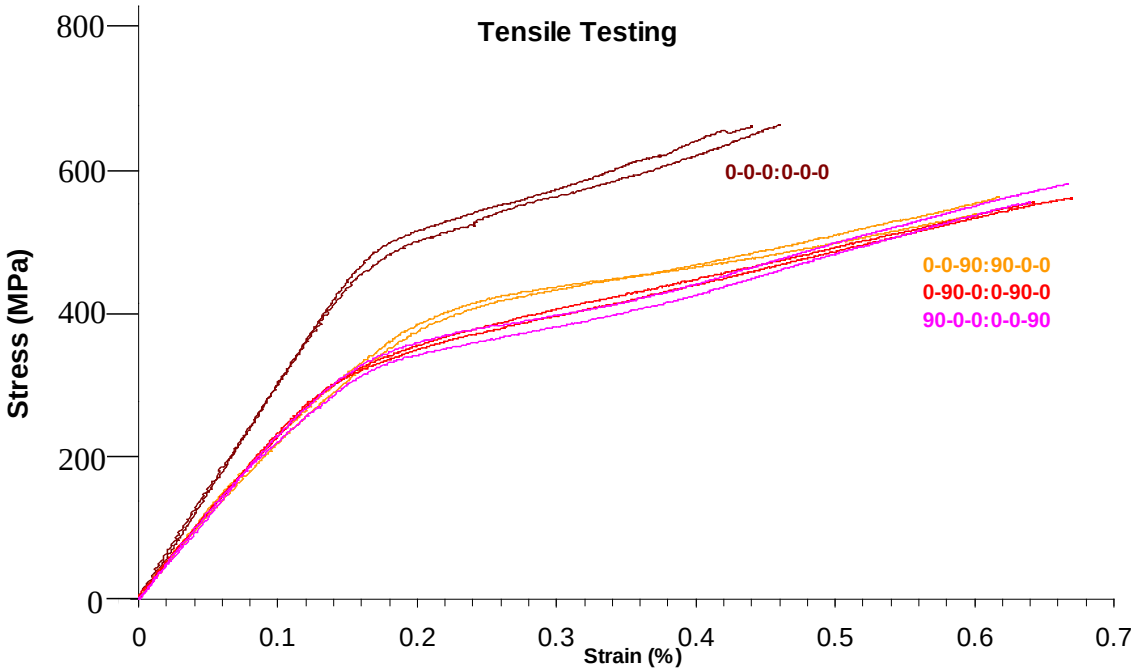

Figure 22. Tensile stress-strain curves for DOE V.

The Flex DOE V samples were all co-processed using the same starting fiber in order to minimize variation. It should be noted, however, that the Flex DOE panels were made at a different time, using different coated fiber than the Tension DOEs, and the resulting properties were slightly different. The ply-level moduli and **PL** were obtained from the tensile results, and the values are given in Table VII.

Table VII. Tensile results for Flex DOE V

	Tensile Modulus (GPa)			Tensile Proportional Limit** (MPa)			# of
Architecture	composite	0 ply	90 ply	composite	0 ply	90 ply	samples
unidirectional 0	298	298	NA	452	452	NA	2
2:1 biased 0:90	231	298*	98	233	300	99	6

*from unidirectional 0 sample **based on 0.005% offset

The samples from Flex DOE V were tested in four-point bending. The stacking sequence of the cross-ply composites had a dramatic effect on the flexural stress-strain response. The entire stress-strain curves are given in Figure 23, but only the initial linear portion is valid. Above **PL**, the matrix is cracking, and the flexure equation used to

calculate stress is no longer valid. The stress-strain curves are presented solely for comparison purposes.

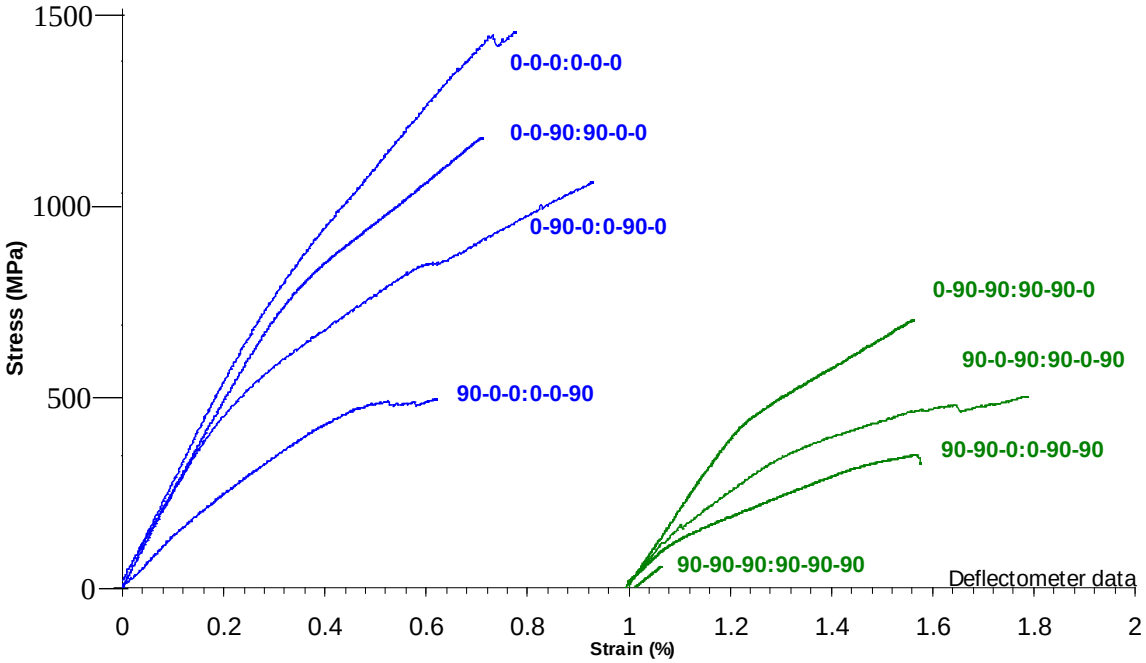

Figure 23. Flexure stress-strain curves for DOE V. Note that only the linear portion of the curve is valid.

The flexure modulus was calculated for each specimen based on the slope of the linear portion of the curve. The flexure moduli of the unidirectional 0 and 90 specimens were within 10 percent of the tensile moduli, and this difference is probably experimental error. Based on composite beam theory, the expected modulus of the biased laminates was calculated using both the flexure and tensile ply-level moduli. As predicted, the measured flexure modulus of the cross-ply samples varied by a factor of ~2 based on the stacking sequence. The measured flexure modulus agreed very well with the predictions, validating the ply-level behavior and the use of beam theory, as shown in Figure 24. The ability to predictably vary flexure modulus by a factor of 2 through stacking sequence demonstrates how this model can be used to tailor the CMC properties.

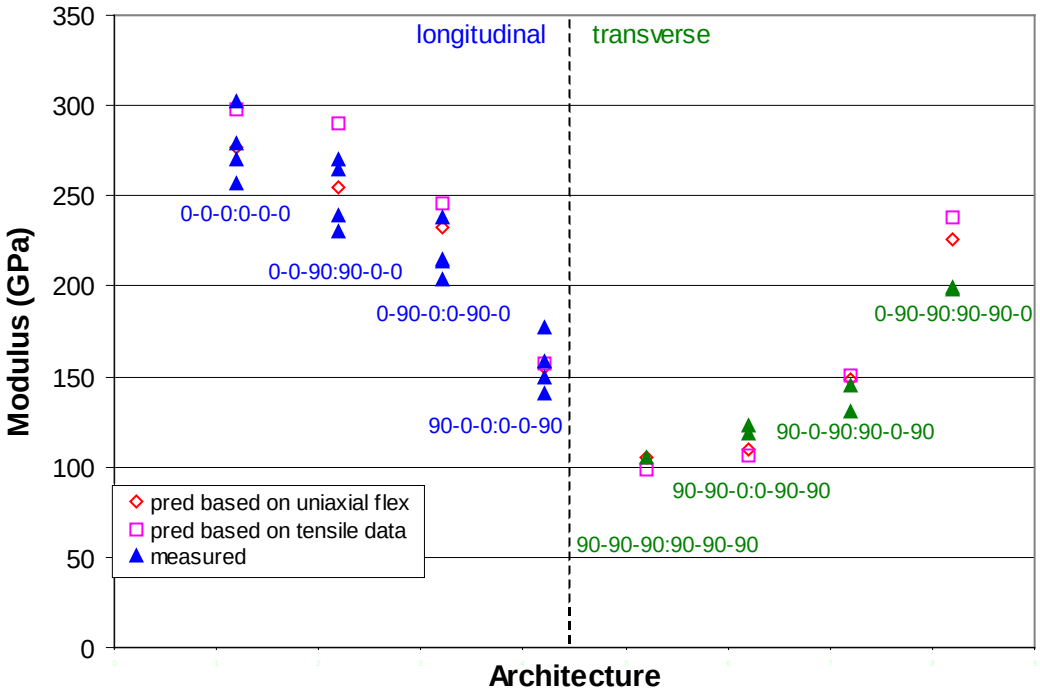

Figure 24. Flexure modulus is shown as a function of stacking sequence. The solid symbols are measured data points and the hollow symbols are the predicted values.

The composite flexure **PL** was determined using the same 0.005% offset as was used to determine the tensile **PL**. A difference of approximately 300% in flexure **PL** was realized as a function of stacking sequence. Based on the flexure moduli of the 0 and 90 plies, the stress in each ply at **PL** was calculated for each sample using beam theory. A comparison to the **PL** predicted based on the Table VII tensile ply-level data is given in Figure 25.

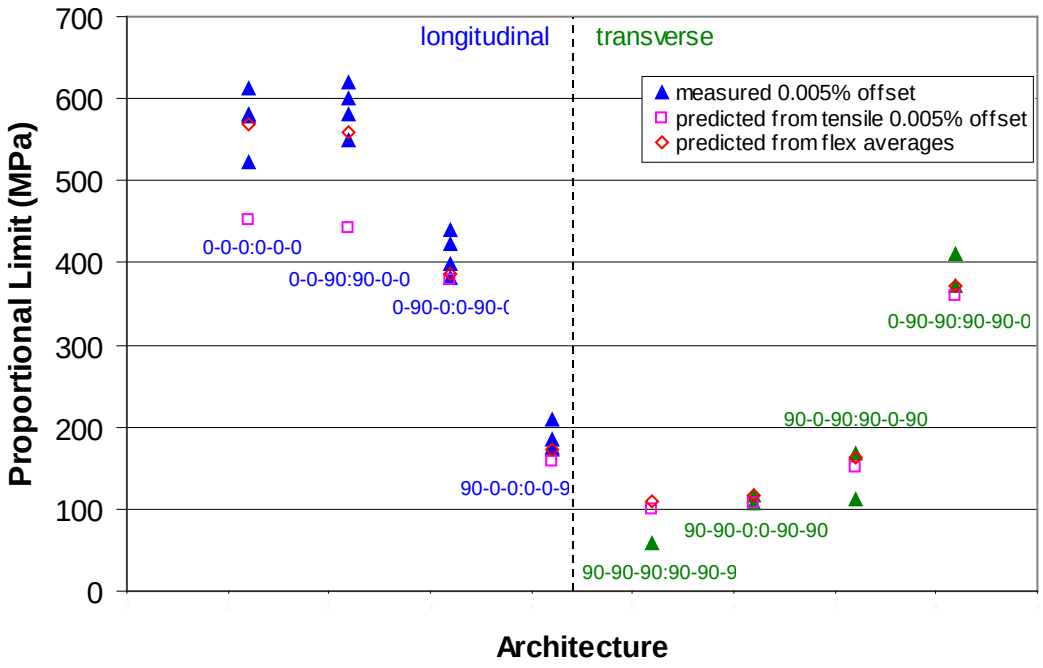

Figure 25. Flexure PL is shown as a function of stacking sequence. The solid symbols are measured data points, and the hollow symbols are the predicted values.

For flex samples with 0 plies on the outside, the typical procedure of using an 0.005% offset to determine **PL** appears to grossly over estimate the **PL**. Careful observations of the stress-strain curves show significant reductions in modulus at stresses well below the calculated **PL**. To reduce this over-estimation, the method of determining **PL** was modified as follows. A line corresponding to the sample modulus without any offset was superimposed on the stress-strain curve. The last data point from the stress-strain curve that falls on the left-hand side of this projected modulus line was taken to be the **PL**. To validate this zero-offset technique, the instantaneous modulus was plotted as a function of stress. The instantaneous modulus was calculated using a least squares regression over a stress range of ~ +/- 14 MPa (2 ksi). The zero-offset approach yielded results in good agreement with the change in modulus, as illustrated in Figure 26. This modified technique reduced the **PL** of the flexure samples with 0 plies on the outside by as much as 175 MPa (25 ksi), but had only a minimal effect on the flexural samples with outer 90 plies, as their stress-strain curves bend over more sharply at **PL**. For consistency, the zero-offset technique was also applied to the in-plane tensile stress-strain

curves for the unidirectional samples from this DOE. For these samples, the reduction in calculated **PL** was about 30 MPa (4 ksi). The use of this zero-offset technique warrants more scrutiny, and alternative methods such as acoustic emission may be more reliable for determining matrix cracking.

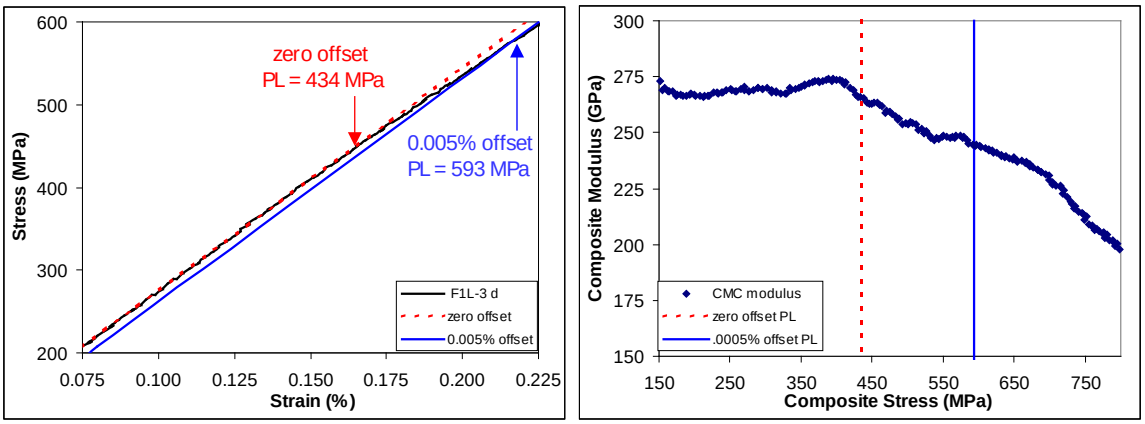

Figure 26. A comparison of the zero-offset and 0.005% offset lines used to measure PL for a unidirectional 0 sample is shown on the left. The instantaneous modulus as a function of stress for the same sample is shown on the right.

The revised **PL** values produce better agreement between the tensile and flexure results, as shown in Figure 27. As predicted, the flexure **PL** of the (0-0-90)s, sample was nearly the same as for the unidirectional (0-0-0)s sample. Both were ~ 420 MPa. Recall that in tension, the unidirectional panel had nearly twice the **PL** of the (0-0-90)s panel. Additionally, the stacking sequence variations in the cross-ply composites produced the predicted effect on **PL**. When the 90 ply was on the outside, (90-0-0)s, the **PL** dropped by a factor of 3 to 140 MPa (20ksi). The ability to predictably change the composite flexure modulus by a factor of 2 and the flexure **PL** by a factor of 3 by altering the stacking sequence demonstrates that the directional nature of the plies can be used to tailor the properties of HiPerComp® CMC in accordance with laminate theory and beam theory. *Most importantly, the ability to utilize the full cracking strength of a 0 ply in a cross-ply laminate in a stress gradient was demonstrated.*

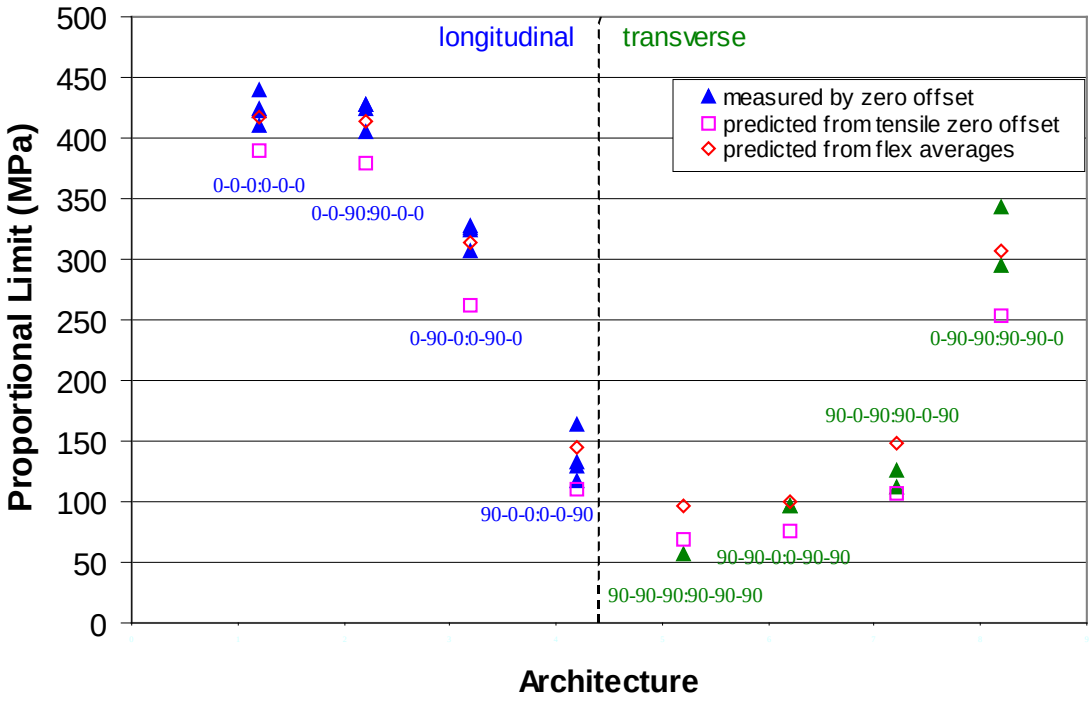

Figure 27. The zero-offset flexure PL is shown as a function of stacking sequence. The solid symbols are measured data points, and the hollow symbols are the predicted values.

The average flexure **PL** and the calculated ply-level stresses at **PL** are given in Table VIII. The ply-level stresses were determined using beam theory, the measured ply thickness, and the ply-level moduli obtained from unidirectional 0 and 90 flex samples. Figure 28 shows the stress distribution of the (0-90-0)s sample for illustration. For completeness, Table VIII includes the **PL** as calculated using both the standard 0.005% offset as well as the zero offset calculations, although it is proposed that the zero offset dataset is more valid and the ensuing discussion will be based on that dataset.

Table VIII. Proportional limit results for the Flex DOE V

The predicted ply level stresses at PL are tabulated. The shading indicates the ply that reaches its failure criteria first, resulting in matrix cracking.

	Zero Offset			0.005% Offset		
Architecture	Measured PL (MPa)	Stress at PL (MPa)		Measured PL (MPa)	Stress at PL (MPa)	
		0 ply	90 ply		0 ply	90 ply
0-0-0:0-0-0	424	424		573	573	
0-0-90:90-0-0	421	432	54	588	601	74
0-90-0:0-90-0	321	383	95	411	491	122
90-0-0:0-0-90	136	162	91	186	221	124
90-90-90:90-90-90	57		57	58		57
90-90-0:0-90-90	97	81	91	110	93	104
90-0-90:90-0-90	119	148	83	140	174	97
0-90-90:90-90-0	319	391	97	392	481	120
tensile result		389	70		452	99

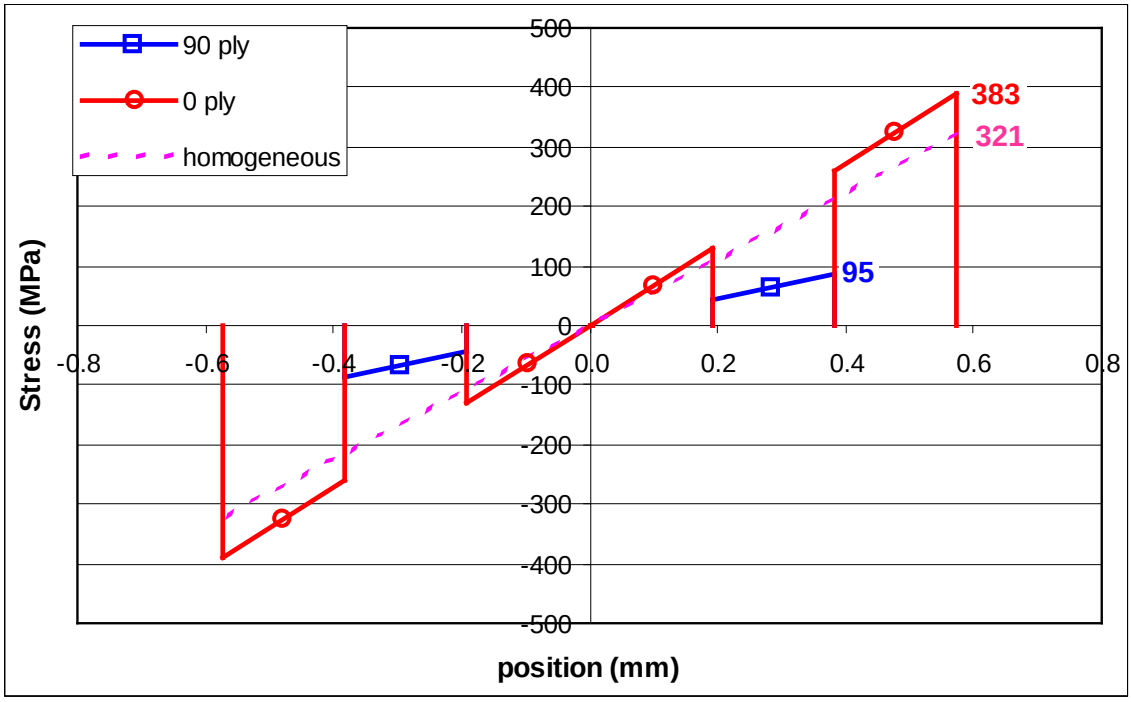

Figure 28. The stress distribution for (0-90-0)s specimen is shown.

The shading in Table VIII indicates the ply that reached its cracking criteria first, as based on the unidirectional flexure **PL**. For the (0-90-0)s and the (0-90-90)s samples, the 0 ply stress at **PL** was within 10% of the unidirectional 0 ply **PL**, so it is possible that the outer 0 plies in these samples may have cracked before the inner 90 plies. Table VIII shows that, for the four architectures in which the 0 ply is believed to crack first, the average peak 0-ply stress ranges from 383 to 432 MPa (56-63 ksi). As compared to the tensile 0-ply cracking stress of 389 MPa (56 ksi), the flexure strength of a 0 ply is zero to 12% higher. A 12 % difference is small, and given the uncertainty in the **PL** calculation, it is difficult to resolve from experimental error for this limited dataset. The strength of ceramics typically increases as the stressed volume decreases. Using the loading factors given by Quinn[50] and Ramamurty et al.,[51] for tensile and flexure tests with similar sample geometry, the flexure strength is related to the tensile strength by Equation 17.

$$\frac{\sigma_f}{\sigma_t} = \left[\frac{6(m+1)^2}{(m+3)} \right]^{1/m} \qquad (17)$$

where: σ_f = 4 pt bend strength (1/3 pt loading)
σ_t = tensile strength
m = Weibull modulus

Even if the 12% difference is real, it would correspond to a Weibull modulus of 46, as calculated from Equation 17. A Weibull modulus of 46 for a ceramic material would be exceptionally high. The minimal difference in 0-ply cracking stress as measured for flexure and tensile specimens implies that flaws of size $\mathbf{a_0}$ (Equation 16) are abundant enough to be present in the stressed volumes of the flexure tests in this study. The conclusion is therefore that, in the case of 0 plies, there is little if any effect of sample volume on cracking stress.

The 90 plies do not have the bridging mechanism of the 0 fibers to resist crack growth. They are therefore expected to fracture in a manner similar to other brittle ceramics, with the added caveat that the 90 fibers with their BN-based coatings may act as flaws in the matrix. In the absence of gross porosity, the largest defect in a 90 ply is likely to be a fiber, or more likely a cluster of fibers. The Type S fibers used in this study are nominally 14 um in diameter. In section 4.2.5, based on the unidirectional results, it was inferred that in tensile testing of balanced-architecture composites, the 90 plies crack

first. Building on this inference, the variation in the tensile **PL** of balanced CMCs will be due to variation in the strength of the 90 plies. A larger historic database of **PL** for balanced-architecture tensile samples can therefore be used to determine the strength variation of the 90 ply and the Weibull modulus of the 90 ply. A database containing over a hundred data points was incorporated into the Weibull plot shown in Figure 29.

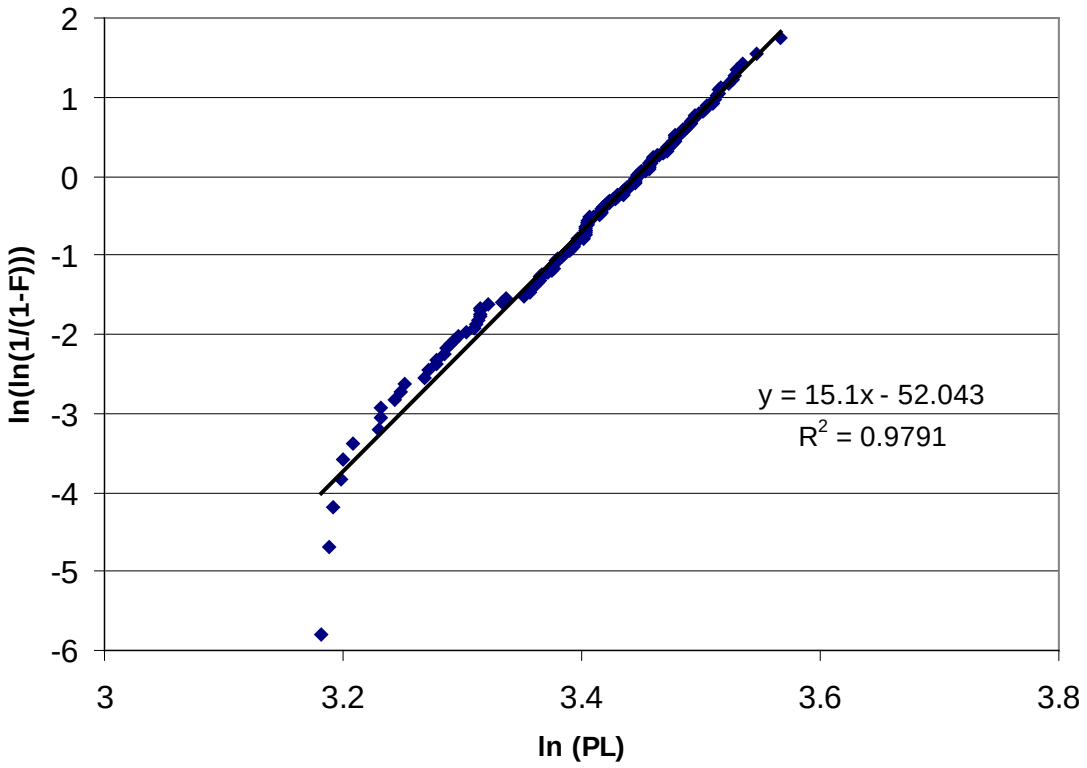

Figure 29. Weibull plot for the strength of a 90 ply based on historic balanced architecture specimens.

The slope of the line in Figure 29 is 15, which is the Weibull modulus. Using m=15 and Equation 17, the expectation is that the flexure strength of the 90 ply should be ~35% higher than the tensile strength as measured in this study. As listed in Table IX, the strength of the 90 ply in the cross-ply tensile tests averaged 69 MPa ksi (10 ksi). The expected cracking strength of the 90 ply in four-point bending is therefore ~ 93 ksi (13.5 ksi). For the cross-ply flexure samples with a 90 ply on the surface, (90-0-0)s, (90-0-90)s, and 90-90-0)s, the stress in the 90 ply at **PL** had an average value of 90 MPa (13 ksi). While based on limited data, this result seems to be in reasonable agreement with the Weibull modulus prediction. For the (0-90-0)s and the (0-90-90)s samples, the

flexure stress in the 90 plies at composite **PL** was 97 MPa (14 ksi). If the outer 0 plies cracked first, then the actual cracking strength of the 90 plies is not known, but it will be greater than or equal to 97 MPa (14 ksi). This stress is potentially greater than the 83-90 MPa (12-13 ksi) measured for samples with 90 plies at the surface. For tensile testing of HiPerComp® CMC reinforced with Hi Nicalon fiber, Nimmer et al.[6] have shown that the tensile **PL** is not affected by the orientation of the surface ply. That is, their balanced-architecture composites with 90 plies on the outside had **PLs** that were statistically equivalent to composites with 0 plies on the outside. Their result suggests that the tensile test is not sensitive to surface flaws. It is therefore likely that the clusters of fibers within the 90 ply are larger than any surface flaws. In the case of the flexure testing in this study, surface flaws may now play a role, and may reduce the strength of the 90 ply when it is on the outside of the sample relative to specimens where it is within the sample bulk with 0 plies on the surface.

The remaining flexure sample to be discussed is the unidirectional 90 ply composite. At 55 MPa (8 ksi), the **PL** of this sample was lower than the calculated 90-ply cracking stress in any of the other flexure samples, and was even lower than the tensile value of 69 MPA (10 ksi). Part of this discrepancy can be explained by residual stress. As described in section 4.2.5, in cross-ply laminates, 7-28 MPa (1-4 ksi) of compressive residual stress acting on the 90 plies was measured. This stress is opposed by an equal and opposite tensile stress acting on the 0 plies, and would therefore not be present in a unidirectional 90 composite. The absence of this residual compressive stress is a likely cause of the low **PL** of the unidirectional 90 CMC.

4.5 *In situ* Cracking

In situ observations of the cracking of specimens from the FLEX DOE V were performed to validate the assumptions of which ply was cracking first. In this case, the flexure specimens were loaded in three-point bending, with a strain gauge mounted on the tensile face directly below the loading pin. One edge of the sample was polished so that the microstructure and microcracking could be observed. Three-point bending was used instead of four- point bending, because the stress will peak under the loading pin. It

is likely that the initial cracking will occur at this peak stress location, so observations were taken of the CMC under the loading pin. The sample was loaded incrementally, held under load, and mounted on the microscope for imaging at each load level. It was then removed from the microscope in order to increase the load.

Figure 30 shows the first crack detected for three of the architectures in this study. As expected, the outermost 0 ply cracked first for the (0-0-90)s sample, and the outer 90 ply cracked first for the (90-0-0)s sample. The ply-level stress at **PL** for the (0-90-0) samples in four- point bending suggested that both the outer 0 ply and the 90 ply were close to their cracking criteria. The first crack detected by the three- point bending *in situ* cracking observations was in the outer 0 ply. While not shown in Figure 30, the same was true for the (0-90-90)s specimen; the first visible crack was in the outer 0 ply. An important caveat to this technique is that only one plane of the sample is visible for observation. Given that the samples are 10mm (0.4") wide, it is possible that other cracks are present in the sample prior to the observation of the cracks at the polished edge. However, it is likely that any cracks would propagate across the thickness of the sample (in the plane of highest stress) more rapidly than they would through the thickness of the sample. These edge observations are therefore still likely to detect the first significant cracking.

Unfortunately, for the 0-90-0 sample, these in situ crack observations using three-point bending do not illuminate which ply cracked first in four-point bending. Three-point bending has a smaller stressed volume than four-point bending and the strength of a 0 ply was shown to be less sensitive to the stressed volume then a 90 ply. The relationship between three- and four-point bend strengths is[50]

$$\frac{\sigma_3}{\sigma_4} = \left[\frac{(m+3)}{3}\right]^{1/m} \qquad (18)$$

where: σ_4 = 4 pt bend strength (1/3 pt loading)
σ_3 = 3-point bend strength
m = Weibull modulus

Based on m = 15 for the 90 ply and m = 46 for the 0 ply, the increase in ply strength in three-point bending compared to four-point bending is 13% for the 90 ply and only 6% for the 0 ply. It is therefore possible that for the 0-90-0 sample, even though the outer 0

ply cracked first in three-point bending, the inner 90 ply may crack first in four-point bending.

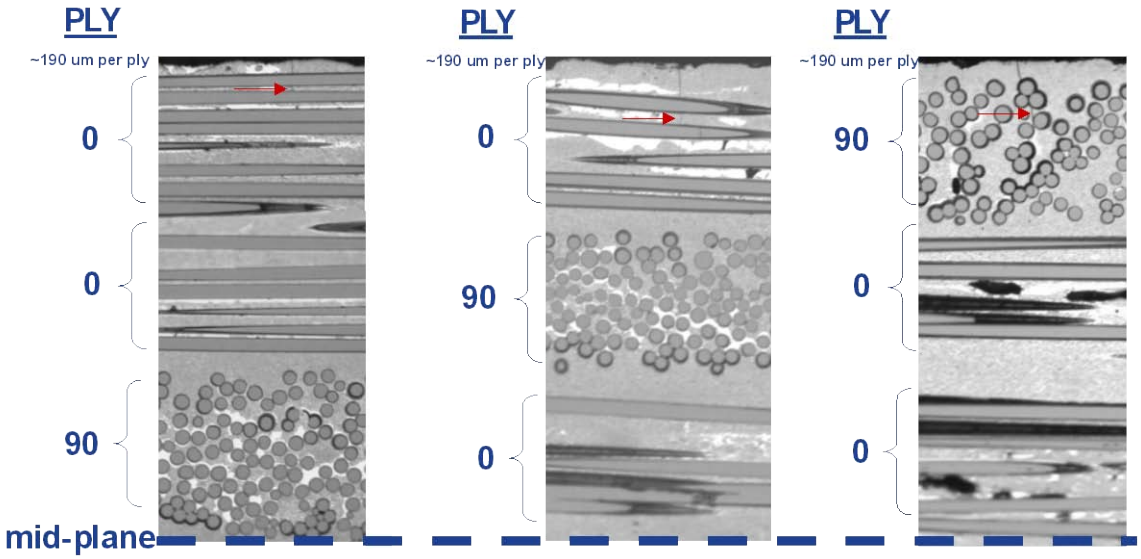

Figure 30. *In situ* crack observations in three-point bending. The first visible crack in each architecture is marked with an arrow.

Optical micrographs of the (0-0-90)s sample at various strain levels are shown in Figure 31. The first crack observed was at the surface of the outer 0 ply. As the load was increased, this crack propagated through the 0 plies, eventually reaching the inner 90 ply. At 0.6% strain, the 0 plies reached a saturation crack spacing of ~ 80 um (3 mils).

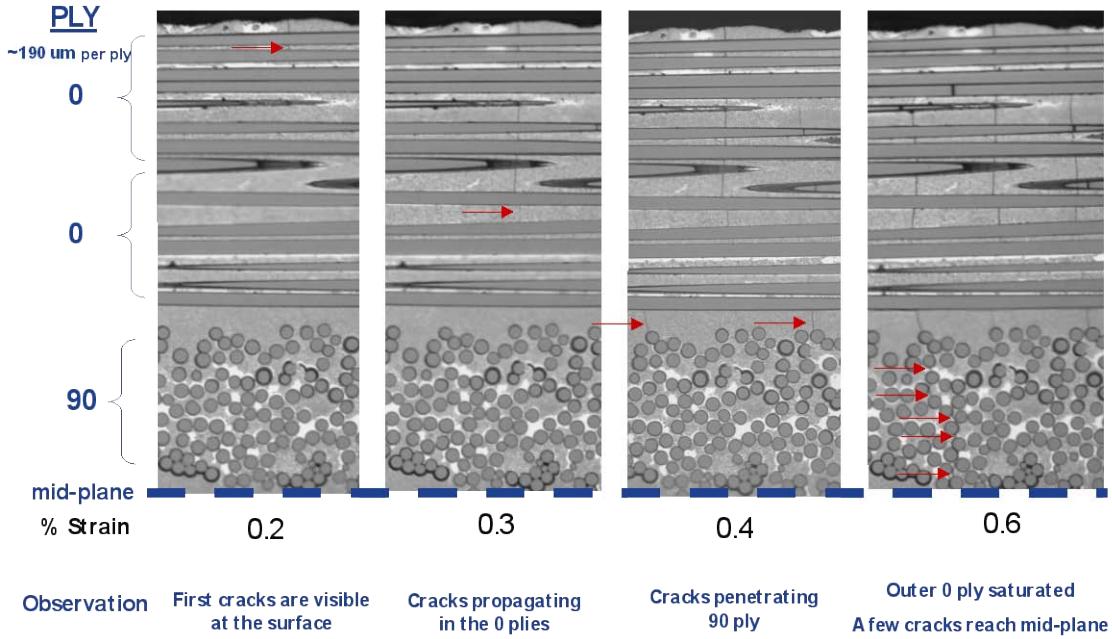

Figure 31. Optical micrographs of the (0-0-90)s specimen at incremental strain levels. The arrows indicate cracks.

This specimen ultimately failed at 0.8% strain, as shown in Figure 32. Failure occurred while the sample was mounted on the microscope, a few seconds after the upper image was taken. The uniform saturation crack spacing was maintained well over 2.5 mm (100mils) away from the loading pin. The box marked region A is the area of the composite under the loading pin, shown previously in Figure 31. The lower image shows that there was an interlaminar component to the final failure, as the large crack present propagated laterally through the 90 ply. However, the cracks of interest in this study are the initial cracks associated with PL and the 0-ply saturation cracks. These cracks are oriented normal to the tensile face, indicating that they are mode I tensile cracks, not shear cracks.

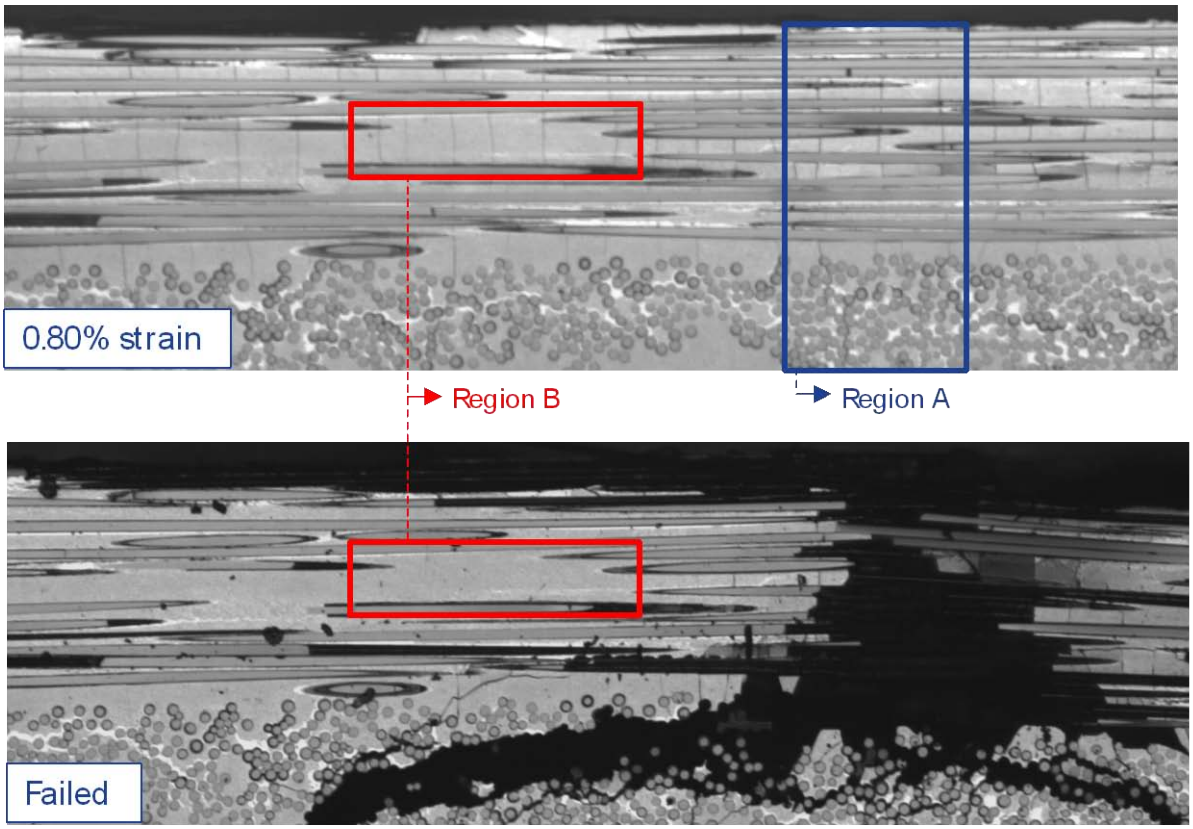

Figure 32. Optical micrographs of the (0-0-90)s specimen before (top) and after (bottom) failure in three-point bending. Three plies are shown (0-0-90), and the nominal ply thickness is 190 um (7.5 mils).

The lower image of Figure 32 also illustrates the phenomenon where matrix cracks close when the sample is unloaded. Matrix cracks were easily visible in region B when the sample was under load. However, as soon as the load was removed, the cracks closed and became difficult to find. The upper image in Figure 33 is an enlargement of region B from Figure 32. This image was taken at 50x initial magnification. The lower image in Figure 33 is the same region after the sample was unloaded, taken at 1000X initial magnification. The scale is the same for both images in Figure 33. The lack of visible cracks in the unloaded sample demonstrates that optical microscopy is not capable

of finding matrix cracks, even if their location is known. The cracks in region B were also not found using scanning electron microscopy.

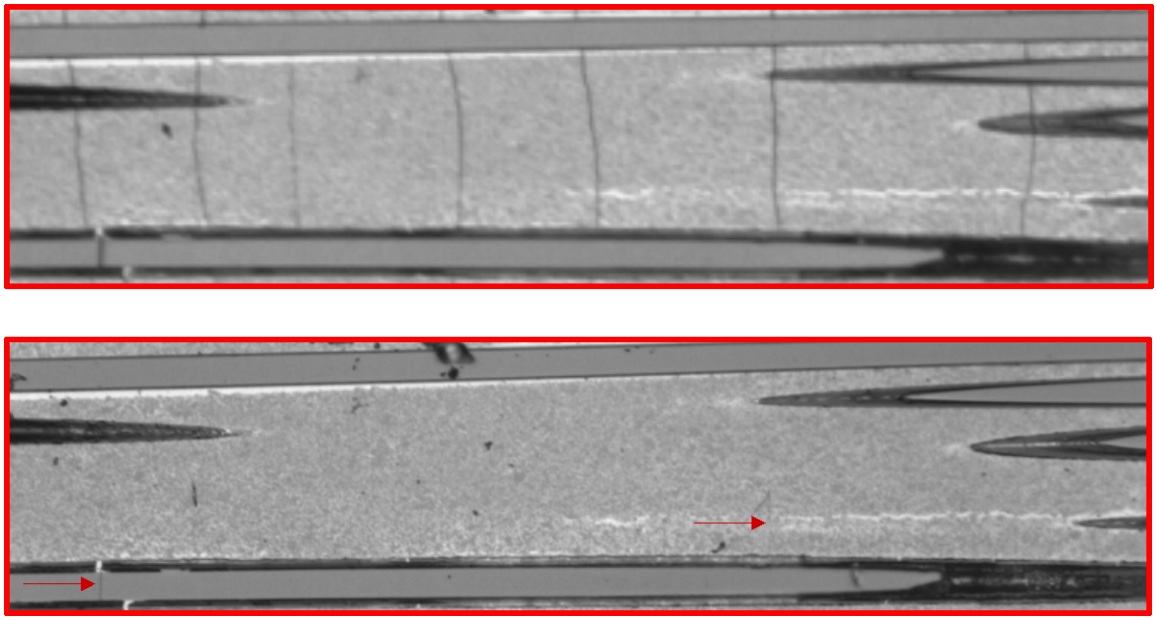

Figure 33. Optical micrographs of the (0-0-90)s specimen at incremental strain levels. The upper image was taken when the sample was under load. The lower image is after unloading. Both images are ~ 500um (24 mils) wide.

4.6 Coefficient of Thermal Expansion

The coefficients of thermal expansion, CTE, of the unidirectional samples from DOE I are summarized in Table IX. The secant CTE from 200C to 1300C is given for the 0 and 90 fiber directions at each fiber loading. A matrix only sample is included as well. The CTE of the 0 and 90 plies at a given fiber loading are very similar. The difference in CTE between the low and high fiber loadings is less than 0.1 ppm/C, indicating that this property is not strongly affected by fiber volume fraction.

Table IX. Secant CTE of 0 and 90 Plies at Three Fiber Loadings

Ply Orientation	Fiber Loading	~ Fiber V_f	200°C to 1300°C Secant CTE (ppm/°C)
matrix only	none	0.00	5.14
0	low	0.21	4.95
90	low	0.21	4.99
0	med	0.23	4.96
90	med	0.23	4.96
0	high	0.33	4.88
90	high	0.33	4.91

4.7 Elevated Temperature

4.7.1 Tensile Tests

The creep-rupture behavior of the medium- and high-V_f material was measured at 1315°C (2400°F). Two panels each were fabricated at the medium- and high-V_f loadings. The panels were 12 ply (0-90-0-90-0-90)s architecture and were co-processed to reduce scatter in the data. Samples from these panels were tested in fast fracture at room temperature and at 1315°C. Figure 34 shows stress-strain curves for these tests. Changing fiber volume fraction did not have a substantial effect on the CMC **PL** at either temperature, but it should be noted that the knee in the curve at **PL** was much more gradual for the high-fiber samples at both temperatures. It is expected that the CMC will have long life at stresses below matrix cracking, where the fiber and fiber coatings are protected from the environment. Since the medium- and high-V_f material have similar **PL**, the creep-rupture testing was done at stresses close to and above **PL** in order to distinguish between the two materials.

4.7.2 Creep-Rupture Results

Table X shows the stress level that each panel was tested at, along with the time to failure and the total sample strain at rupture. The rupture strains include both elastic and creep strain. All of the samples in this study failed in the gauge section.

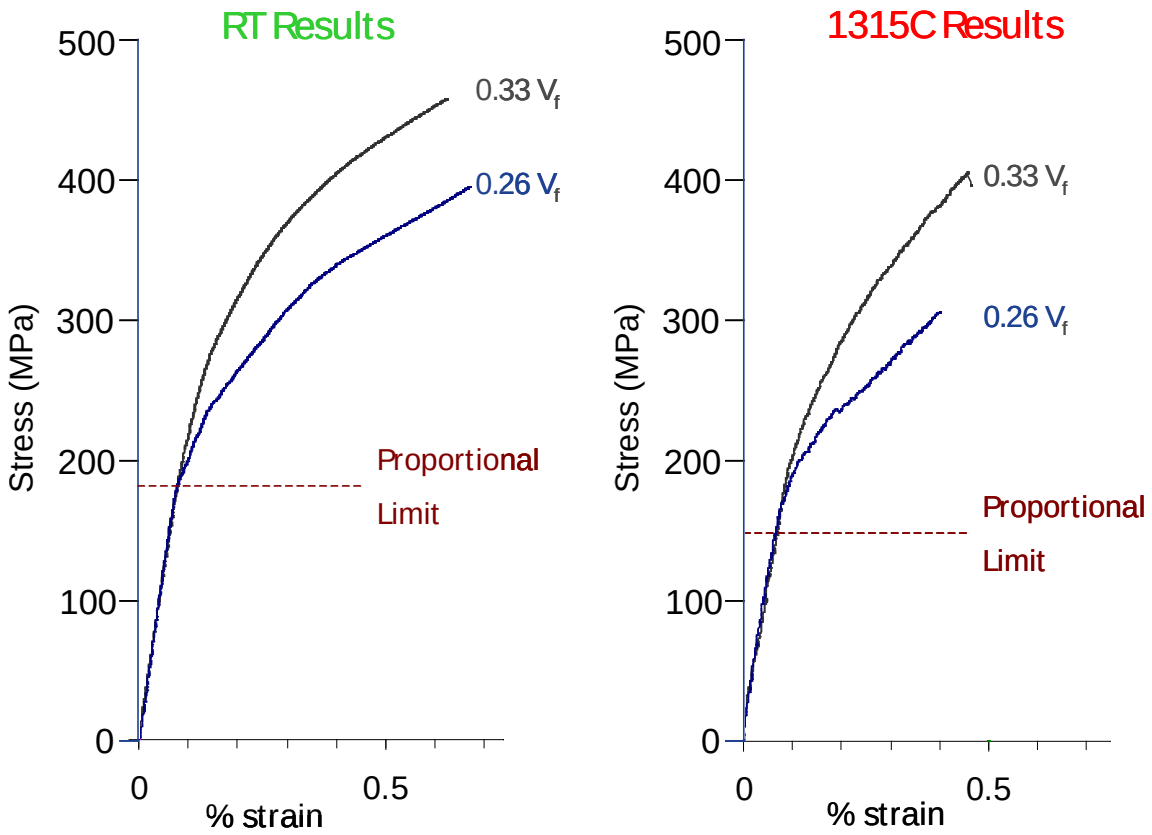

Figure 34. Room temperature and 1315°C stress-strain curves for medium and high–fiber- loading samples.

The strain-versus-time plots for both sets of samples are given in Figure 35. It is apparent that the total strain at rupture (elastic strain plus creep strain) decreased as stress increased. The strain-time curves for most samples display a high initial creep rate, followed by a decrease in creep rate with time. The exceptions are the highest-stressed samples that had short lives and failed in primary creep. The minimum creep rate in the second regime was taken for analysis purposes. After passing through this minimum rate, to varying degrees, some of the samples showed an increase in creep rate that continued until failure. This tertiary creep is more apparent in the high-$\mathbf{V_f}$ samples, but is present in the medium- $\mathbf{V_f}$ specimens as well.

Table X. Creep-Rupture Summary

Sample ID	Nominal V_f	Composite Stress (MPa)	Max Fiber Stress (MPa)	Min Creep Rate (1/s)	Rupture Strain (%)	Rupture Time (hrs)	a surface	b spans 90	c spans 0	d 90 bundle
1	0.26	214	1645	2.9E-06	0.20	0.1	NA	NA	NA	NA
2	0.26	193	1485	5.2E-08	0.33	5	no	yes	yes	no
3	0.26	179	1379	1.8E-08	0.40	20	no	yes	yes	no
4	0.26	166	1273	1.4E-08	0.70	74	yes	yes	yes	no
5	0.26	138	1061	5.0E-09	0.75	272	yes	no	no	yes
6	0.26	131	1008	8.9E-09	0.72	135	yes	yes	no	yes
7	0.33	241	1463	3.4E-08	0.50	16	yes	yes	no	no
8	0.33	228	1379	1.8E-08	0.73	64	no	yes	no	yes
9	0.33	214	1296	1.4E-08	0.81	92	yes	yes	no	yes
10	0.33	200	1212	1.5E-08	1.20	118	yes	yes	no	yes
11	0.33	172	1045	9.2E-09	1.50	336	no	no	no	yes
12	0.33	166	1003	5.5E-09	1.48	479	no	no	no	yes

a) span a 90 ply, cross a 0 ply and span the 90 ply on the other side of the 0 ply
b) cracks in the surface matrix rich layer, arrested by outer 0 ply fibers
c) tunnel cracks in 90 ply that span the width of the 90 ply and are arrested by the fibers in the adjacent 0 plies
d) cracks within the 90 tow bundle that do not leave the tow bundle

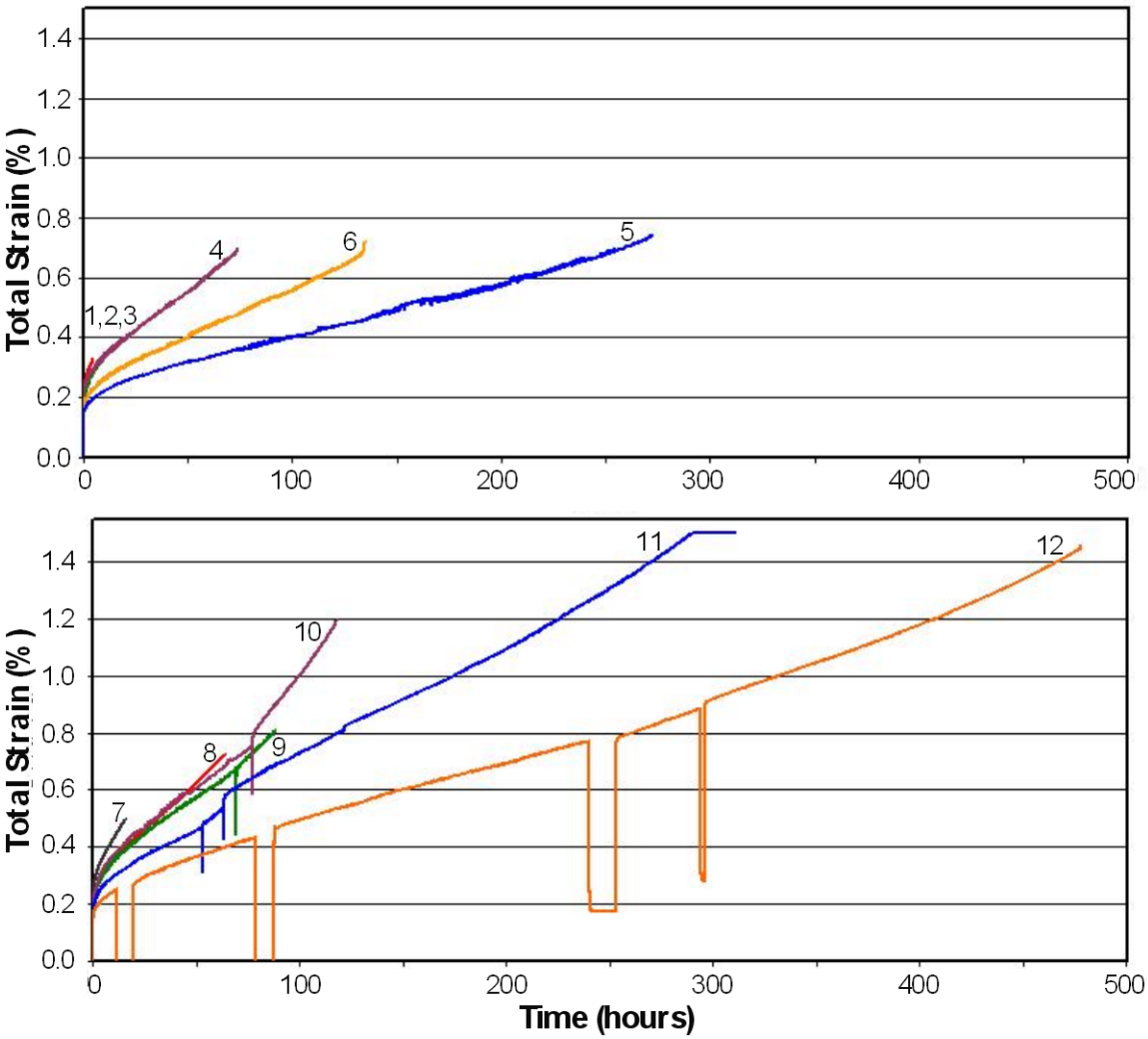

Figure 35. Strain-time curves at 1315°C. Curve numbers correspond to sample identifications given in Table X.

Stress versus rupture life is typically plotted using a log scale for life, as shown in Figure 36. When plotted this way, both datasets follow nearly linear trend lines, with the high-fiber specimens experiencing longer lives at a given composite stress. Alternatively, for a given rupture time, the high-fiber CMC can withstand higher stresses than the medium-fiber material.

The model put forth by McLean[27] for a creeping fiber in a creeping matrix assumes power-law creep (Equation 7) for both the fiber and the matrix. Due to the difference in creep rates in these constituents, the model predicts that the composite's stress exponent, **n**, in Equation 7 will vary with applied stress. However, the data in this study span a limited stress range, so the minimum creep rate may still have a constant

stress exponent over the stress range explored. The minimum creep rate, $\boldsymbol{\varepsilon_{min}}$, is plotted against the composite creep stress on a log-log scale in Figure 37. The power-law relationship holds for each dataset, as the data points in this plot fall along approximately straight lines. Each data set was curve fit, and, based on the regression lines, the values of **A** and **n** for Equation 7 were determined, as shown in Figure 37. In both cases, the creep exponent **n** was just over 3. As determined by the creep exponent, the slopes of these lines are similar, but the high-fiber curve is offset, producing lower creep rates at a given composite stress. This is consistent with the notion that the fiber is more creep resistant than the matrix.

The rupture strain as a function of applied stress for the medium- and high-fiber samples is plotted in Figure 38. The composite strain at rupture is a combination of elastic strain plus creep strain. At higher applied stresses, there should be a larger elastic strain. However, both datasets show an increase in rupture strain at lower stresses, where the time to rupture was longest. This result implies that the strain in the lower-stressed samples had a larger contribution from creep than the higher-stressed shorter-lived samples. At a given applied stress, the high-$\mathbf{V_f}$ samples had longer rupture times and larger rupture strains than the medium-$\mathbf{V_f}$ samples. This result implies that the high-$\mathbf{V_f}$ samples underwent more creep deformation than the medium-$\mathbf{V_f}$ samples.

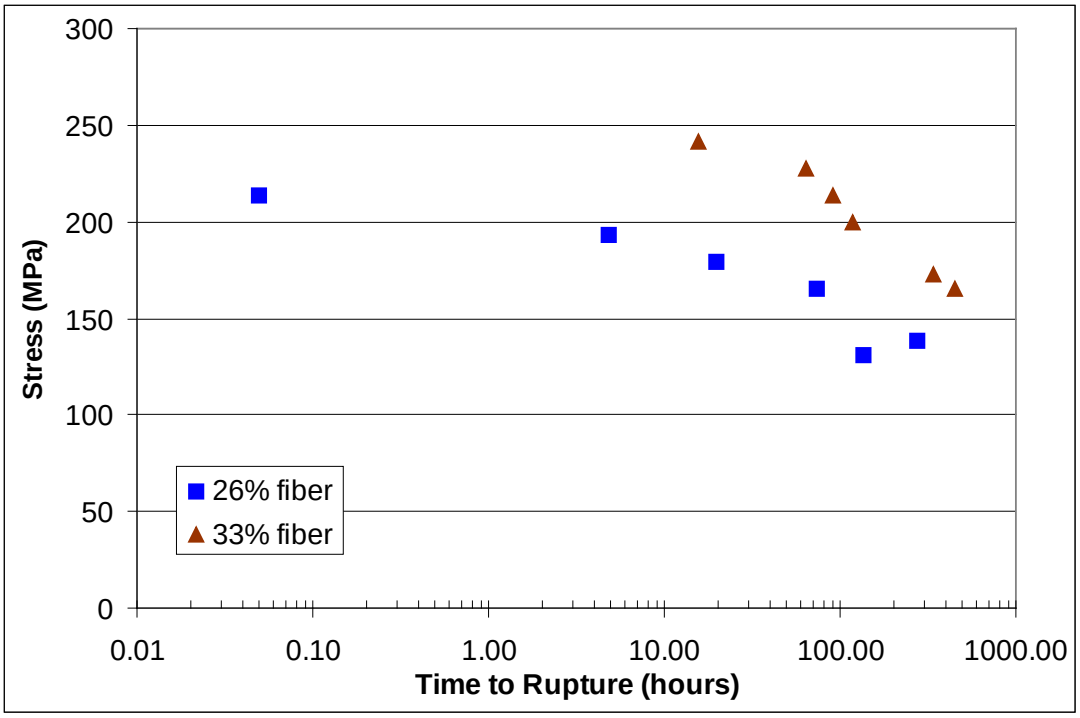

Figure 36. Plots of data for stress versus rupture time at 1315°C.

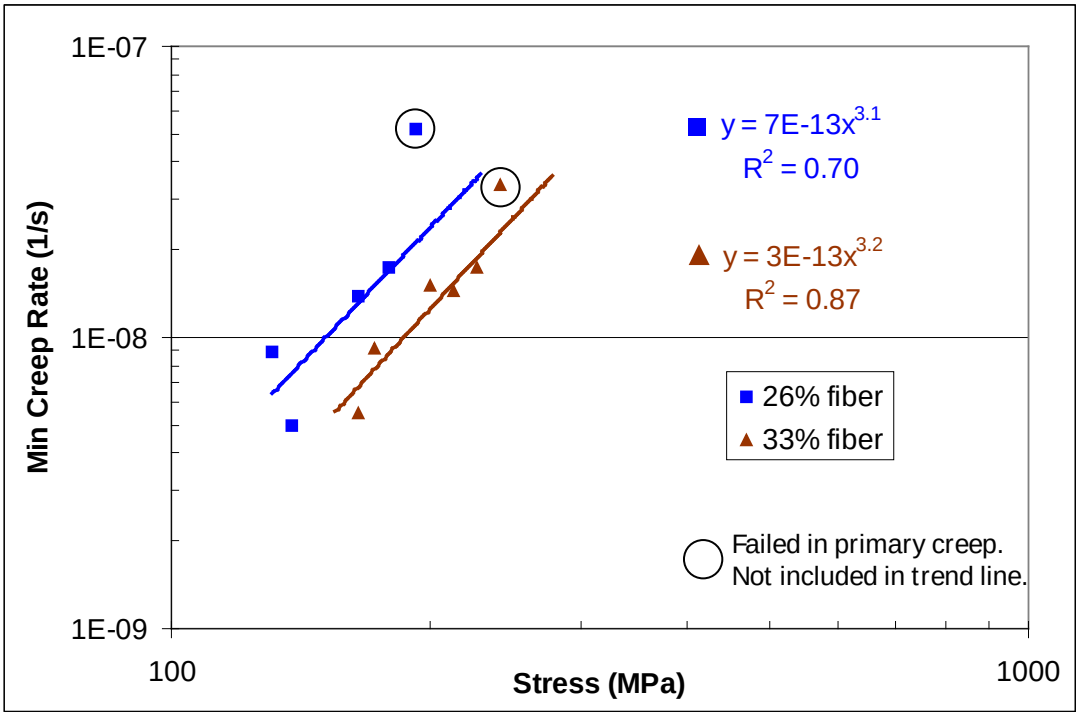

Figure 37. Minimum creep rate versus composite stress.

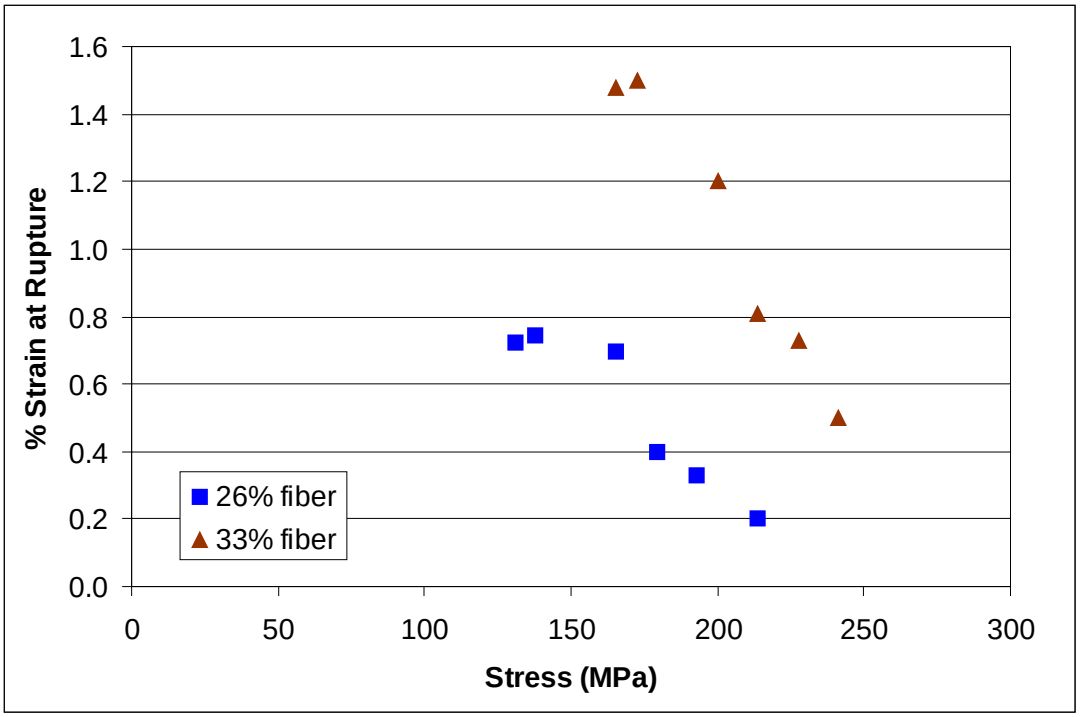

Figure 38. Rupture strain as a function of applied stress.

4.7.3 Post-Rupture Microstructures

Post rupture, the samples were mounted in epoxy, and the edge normal to the fracture surface was polished. Optical microscopy revealed cracks in all of the samples. For the purpose of this discussion, the cracks will be described by four groups, as illustrated by Figure 39. The first, group A, is for cracks in the matrix-rich layer at the surface of the CMC. In all cases, these cracks terminate at the outermost 0 fibers and do not penetrate the 0 ply to a significant degree. Group B contains tunnel cracks that span the entire width of a 90 ply before arresting at the adjacent 0 plies. These cracks penetrate the 0 plies to varying degrees. If such a crack completely crossed a 0 ply, then it is categorized as group C. The last group, D, are intra-tow features within the fiber rich band of a 90 ply. These features meander around the 90 fibers, which are oriented normal to the load direction. While some of the cracks in groups B and C might have originated from these features, group D is reserved for the case where these cracks do not leave the fiber bundle; that is, they do not cross the matrix-rich band (if present) and do not terminate at a 0 fiber.

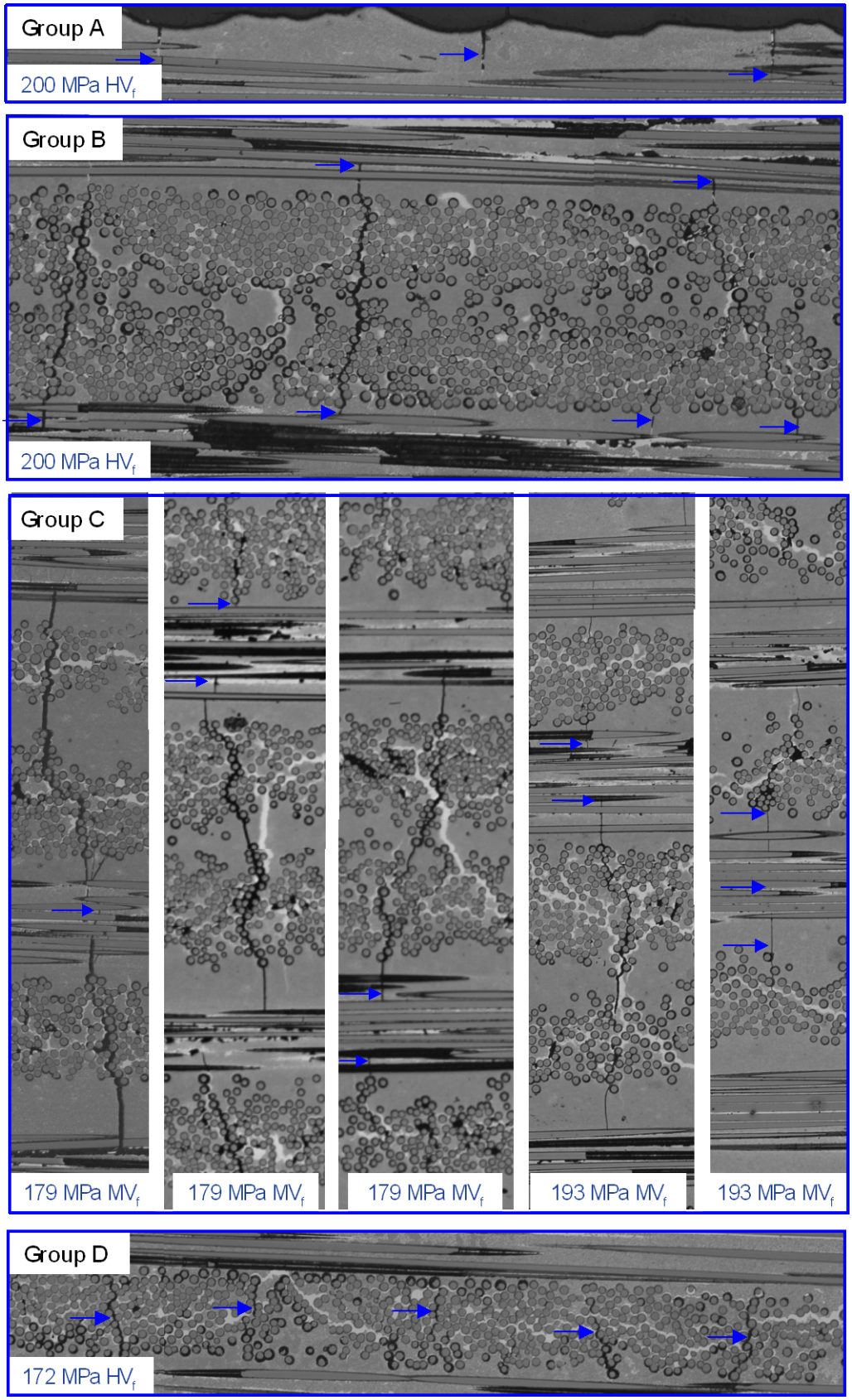

Figure 39. Examples of the crack types seen in the ruptured specimens.

The group-D cracks appear to be the result of creep-induced cavitation. Even though the 90-degree fibers are loaded normal to their axis, they will still be more creep resistant than the matrix. Additionally, due to the fiber coating, the 90 fibers are not expected to carry load in the 0 direction, and therefore would not have a driving force for creep. The result is that the 90 fibers act as a creep-resistant inclusion. During creep, the matrix deformation may not always be capable of accommodating the non-deforming 90-degree fibers. As a result, cavities form adjacent to the fiber, as shown in the top of Figure 40. These cavities are always located on a side of the fiber in line with the loading direction, and form at the coating–matrix interface, as opposed to at the coating-fiber interface. This is consistent with the expectation that the 90-degree fibers and coatings are not carrying load in the 0 direction. The uppermost arrow in the upper image in Figure 40 shows a cavity that formed at an individual fiber, without any associated matrix crack. The remaining arrows in this image show a number of these cavities linking up to form a crack in the 90 ply. This type of crack is the group D defect tabulated in Table X. The group D cavitation cracks tend to exist at a periodic spacing in the 90 plies, as shown in the bottom of Figure 40. A summary of the types of cracks present in each of the creep samples is given in Table X. The medium-$\mathbf{V_f}$ sample had a rupture life of only 3 minutes, so its cracks were not easy to find and are not included in Table X. The cracks in the other samples were readily visible.

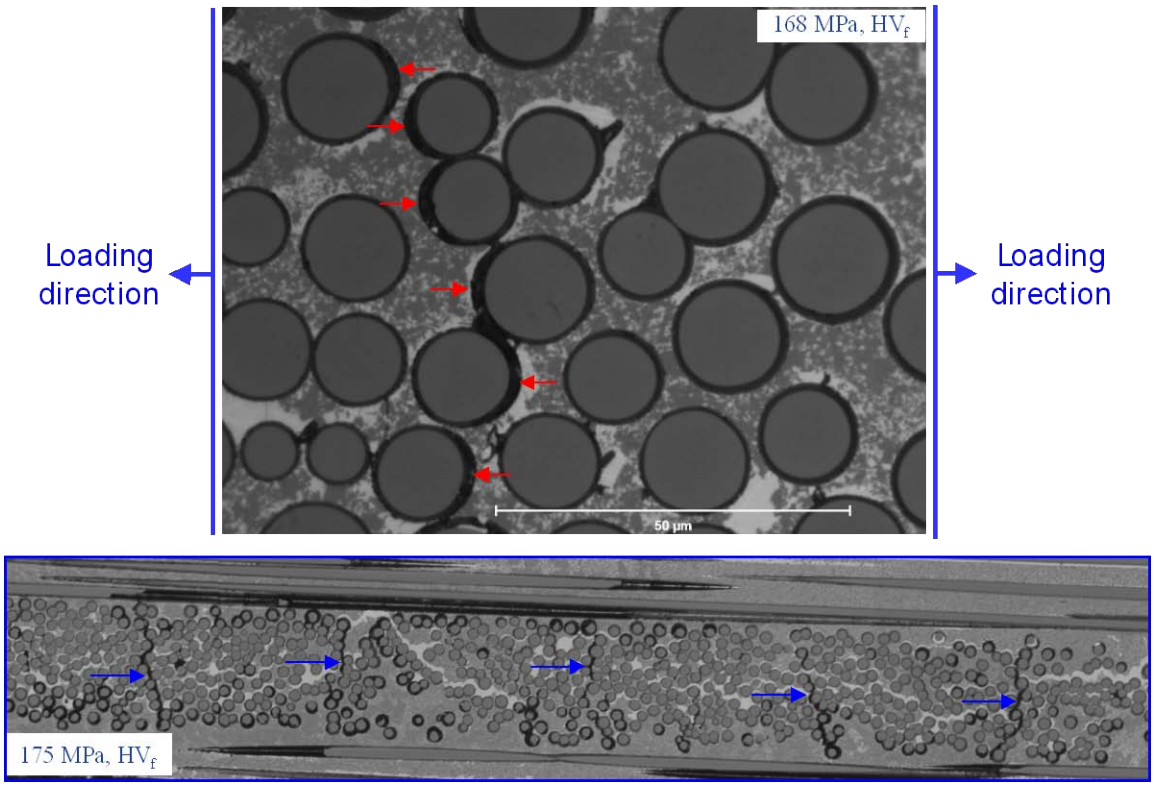

Figure 40. Matrix cavitation adjacent to 90-degree fibers in line with the loading direction (top). 90-degree ply crack resulting from the joining of cavities from neighboring fibers (bottom).

Cracks in groups A, B, and C all potentially expose load-carrying 0 fibers to the test environment and make them subject to oxidative degradation. A group-C crack would expose the most 0 fibers. Since the group-D cracks remain in the 90-tow bundles, they do not expose the 0 fibers to environmental degradation. All of the samples with medium $\mathbf{V_f}$ had cracks from group A, B, or C. Three of the medium-$\mathbf{V_f}$ samples had group-C cracks that had propagated all the way through a 0 ply. These cracks were over 10 microns wide and were full of oxide, indicating that they had been open to the environment for some time. Often, the cracked 0 ply was adjacent to the double 90 plies at the specimen's mid-plane. As concluded in section 4.2.5, the double 90 ply has the same initial cracking stress as a single 90 ply. However, once the crack is formed, the crack length in a double 90 ply will be twice that of a single 90 ply. Less stress will be required to propagate this longer crack through a 0 ply. The group-C cracks are therefore more likely to be found in 0 plies adjacent to double 90 plies.

The two medium-$\mathbf{V_f}$ samples with the lowest stresses, 133 and 140 MPa, have group A and group B cracks, but none from group C. Interestingly, counter to the trend for the rest of the samples, despite having a lower stress and lower creep rate, the 133 MPa sample had a shorter rupture life and higher creep rate than the 140 MPa sample. Examination of the ruptured sample did not provide an obvious reason why the 133 MPa sample is an outlier. One possibility is that, due to sample-to-sample variation in PL, the 133 MPa sample may have cracked upon loading, while the 140 MPa sample may not have cracked. This argument is speculative, as there is no data to either prove or disprove this hypothesis.

None of the high-$\mathbf{V_f}$ samples had group-C cracks spanning a 0 ply. The medium-$\mathbf{V_f}$ CMC exhibited group-C cracks at composite creep stresses as low as 168 MPa. In comparison, the high-$\mathbf{V_f}$ material did not have such cracks even at a 245 MPa composite stress. Two factors may contribute to this difference. First, the high-$\mathbf{V_f}$ 90 plies are ~ 25% thinner than the medium-$\mathbf{V_f}$ 90 plies. Therefore, a crack spanning a high-$\mathbf{V_f}$ 90 ply will be shorter and will require more energy to propagate than a longer crack in the medium-$\mathbf{V_f}$ material. Additionally, with the higher fiber loading in the high-$\mathbf{V_f}$ material, more energy is required to propagate a crack through the 0 ply. The result is that, at a given stress, 90-ply cracks in the high-$\mathbf{V_f}$ material will not extend as far into the adjacent 0 ply as in the medium-$\mathbf{V_f}$ material. Therefore, in the high-$\mathbf{V_f}$ material, fewer 0 fibers are exposed to environmental degradation, and the rupture life and rupture strain will be larger. This conclusion is supported by the results in Table X. Additionally, it is suspected that the lower composite creep rates of the high-$\mathbf{V_f}$ material would reduce the tendency for cavitation. At a given stress, using a more creep-resistant fiber can further reduce the composite creep rate. CMC samples were also fabricated with Sylramic iBN fiber, which is reported by NASA researchers[52] to have better creep resistance than Type S fiber. Figure 41 shows the strain-time curves at 166 MPa for medium-and high-V_f Type S CMC along with medium-V_f Sylramic iBN CMC. The improvement in composite creep resistances is obvious, and two iBN Syrlamic samples reached the 500-hour run-out at this stress level. The gauge section of one of the iBN Sylramic samples was sectioned and polished as before, and optical microscopy did not reveal any signs of the matrix cavitation adjacent to 90 degree fibers that was prevalent in the Type S CMC.

Since all samples in this study used the same matrix material, the lack of cavitation in the Sylramic iBN CMC can be attributed to the lower composite creep rate.

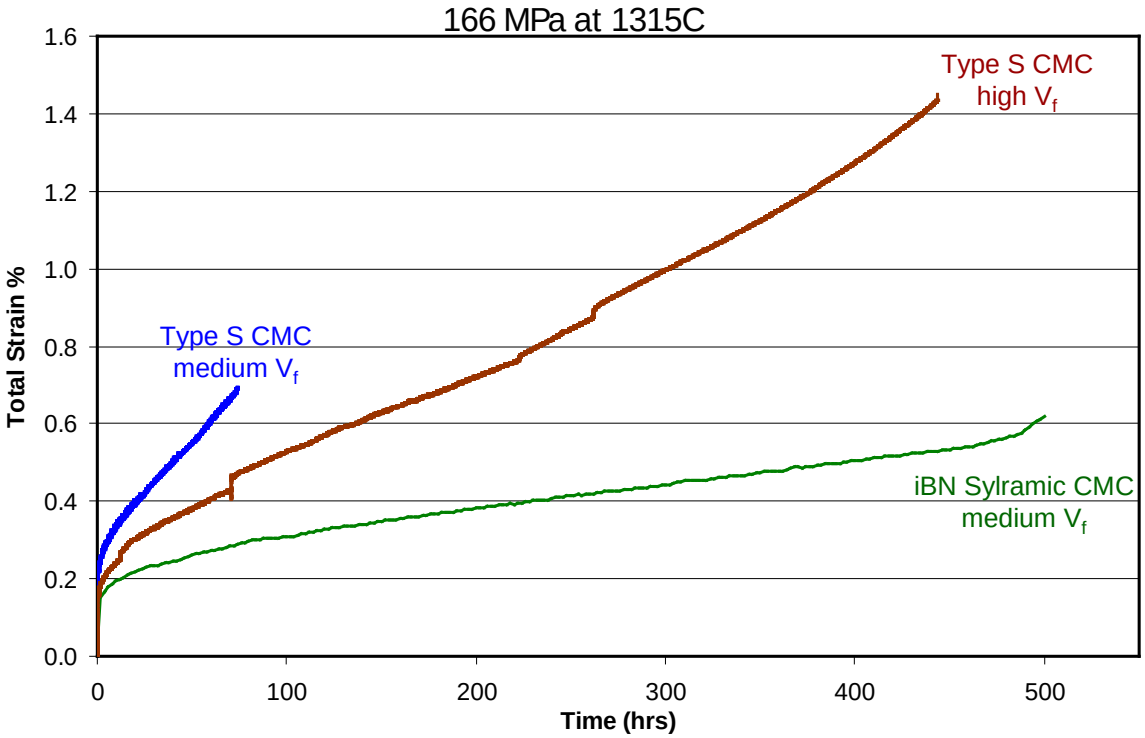

Figure 41. Effect of fiber type on CMC creep at 166 MPa and 1315°C.

4.7.4 Creep Rupture Normalized for Fiber Loading

As discussed in the chapter II, the MI matrix used in this study is expected to be more creep prone than the Type S fiber. During creep, the stress in the matrix will relax as load is shed to the more creep-resistant fiber. Additionally, as shown in the previous section, all of the specimens in this study cracked during creep exposure. The matrix cracks will further transfer load to the fibers. For the samples in this study, if the simplifying assumption is made that the bulk of the stress is being carried by the fibers, then the results can be normalized based on fiber volume fraction. For the purpose of this study, the maximum possible fiber stress was determined as the applied composite stress divided by the fiber volume fraction. When the data are plotted as a function of the maximum fiber stress, the stress-versus-rupture and rupture-strain-versus-stress curves for the medium- and high-$\mathbf{V_f}$ samples converge towards a common trend line, although

the high-$\mathbf{V_f}$ data points are still slightly above the medium-$\mathbf{V_f}$ points, as shown in Figures 42 and 43. The strain-rate-versus-stress data for both fiber loadings merge onto a master trend line, as shown in Figure 44. For comparison, creep-rate data for the constituent phases are included in Figure 44. The creep rate based on the maximum fiber stress is remarkably similar to that reported by Sauder and Lamon[30] for the raw fiber. Sauder and Lamon reported a creep exponent of ~2.6 for the fiber. The creep exponent of the combined dataset from this study is ~3.1. Note that the two composite specimens with the highest stresses exhibited higher creep rates than the raw-fiber trend line. These samples appear to have failed in primary creep (see Figure 35), and as such were excluded from the regression calculation. These results demonstrate that, for the HiPerComp® CMC at 1315°C, the composite creep rate at a given applied stress may be predicted from the raw-fiber creep rate and the composite fiber volume fraction.

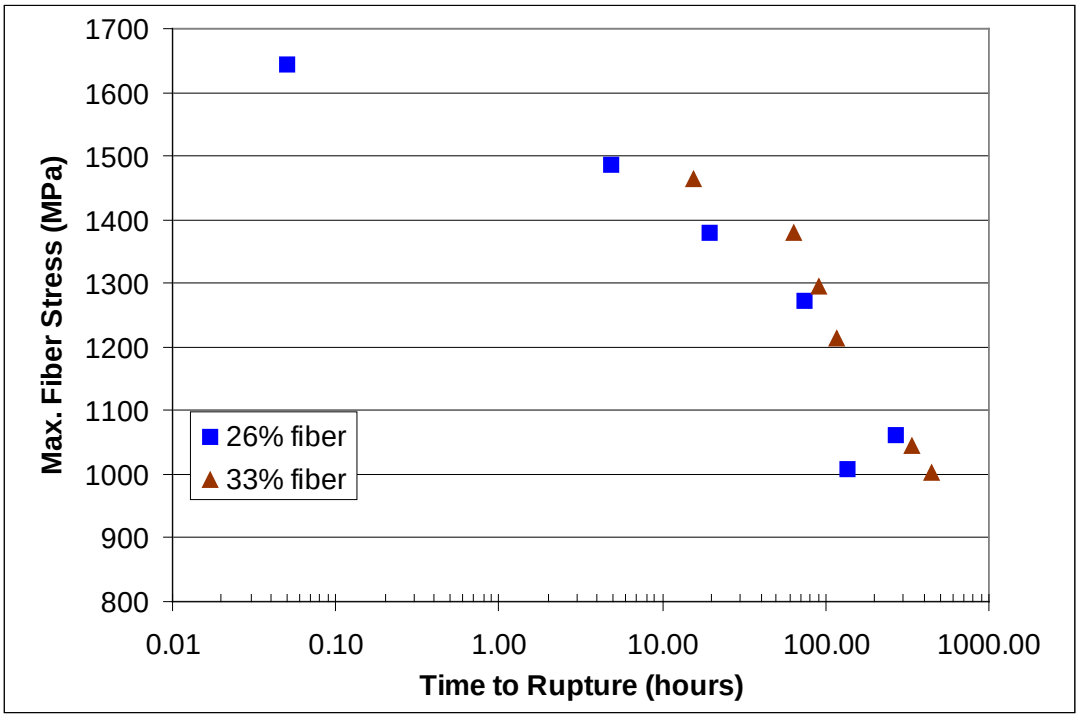

Figure 42. Stress–rupture curves normalized for fiber loading.

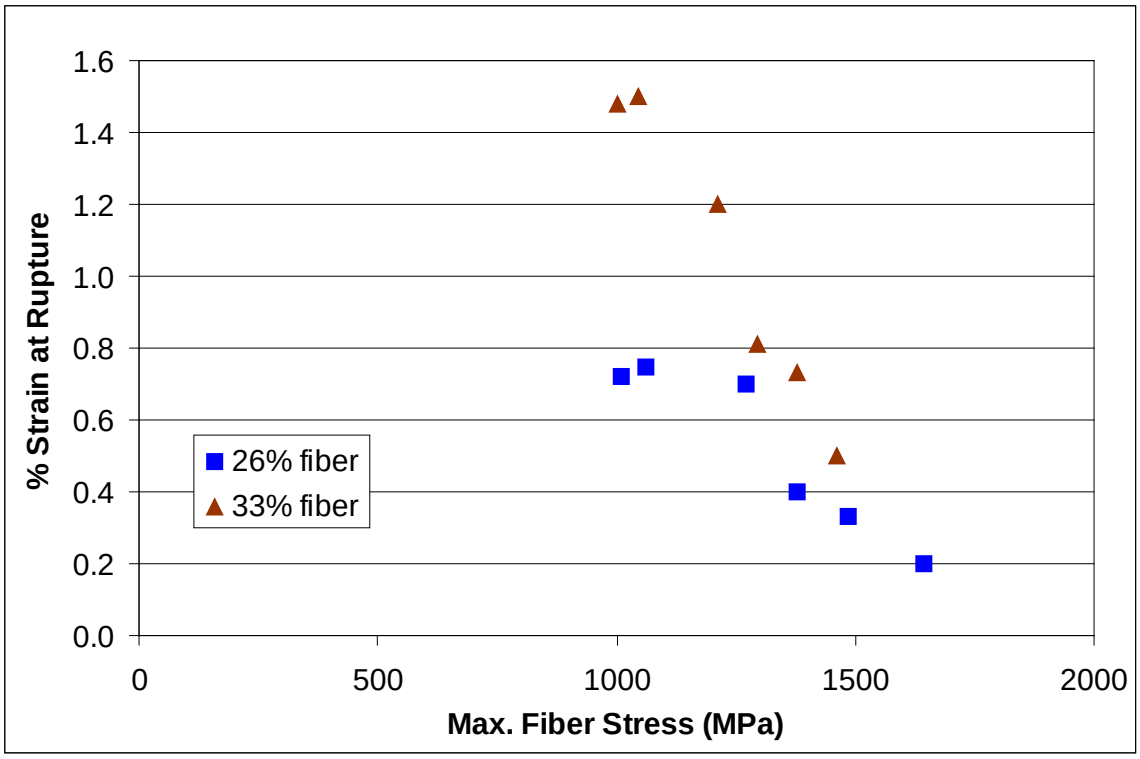

Figure 43. Rupture strain–stress curves normalized for fiber loading.

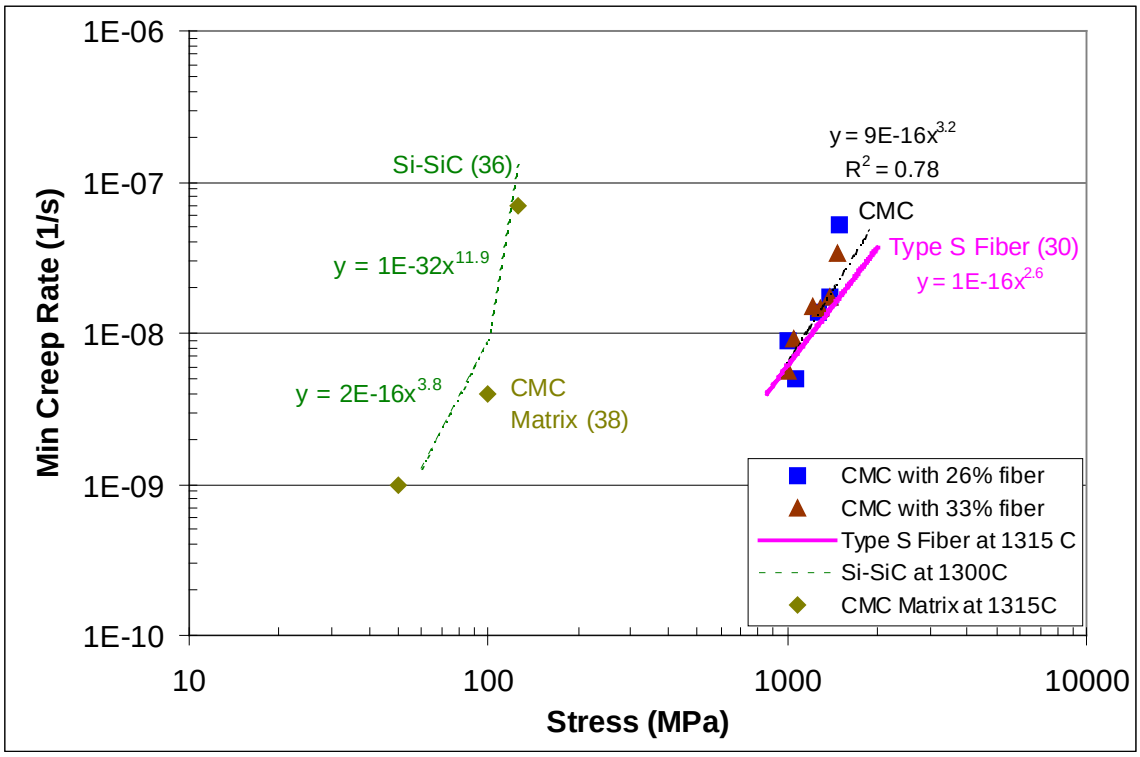

Figure 44. Creep-rate-versus-stress curves normalized for fiber loading.

This result illustrates how the creep rate of the composite can be tailored by changing the fiber volume fraction in the test direction. In the present study, the fiber loading was varied in balanced-architecture CMCs. The fiber volume fraction in the test direction can also be varied by biasing the fiber architecture. For example, the $\mathbf{V_f}$ for the high-fiber CMC in this study is 0.33. For the balanced samples where the 0:90 ratio is 1:1, the $\mathbf{V_f}$ in the test direction is 0.165. If the ratio of 0:90 were 2:1, then $\mathbf{V_f}$ in the test direction would be 0.22. The results of this study suggest that this biasing effect could reduce the creep rate. The creep rate of biased CMCs was not measured in this study, and such testing is suggested for future work.

A Monkman-Grant plot for both fiber volume fractions is given in Figure 45. In this plot, both the medium- and high-$\mathbf{V_f}$ data points fall on straight lines, indicating that this model fits the data. The exponents for both $\mathbf{V_f}$ are greater than 1, indicating a greater amount of viscoelastic strain at lower strain rates. This is consistent with the rupture-strain results discussed in section 4.3.2. The trend line for the high-$\mathbf{V_f}$ material is above that of the medium-$\mathbf{V_f}$ material, with the high-$\mathbf{V_f}$ samples exhibiting ~ 2X the life of the medium-$\mathbf{V_f}$ samples at a given strain rate. This result is consistent with the trends shown in Figures 42 and 43. At a given creep rate, the high-$\mathbf{V_f}$ CMC has longer rupture times and larger rupture strains. More work needs to be done to understand these differences, but the cracking seen in the post-rupture microstructures, and tabulated in Table X, suggests that 0 fibers in the medium-$\mathbf{V_f}$ samples may have greater environmental exposure than in the high-$\mathbf{V_f}$ material. Such exposure would degrade the fiber properties and shorten the rupture life.

There is good agreement between the data in this study and the commonly used power-law relationship between strain rate and stress (Equation 7) as well as with the Monkman-Grant model (Equation 9). It is unknown whether this relationship will be true at other temperatures or in stress ranges where the matrix is not cracked. The McLean model[27] for a composite, in which the matrix creeps faster that the fiber, predicts that the creep exponent will vary with applied stress. If this model is true for the HiPerComp® CMC, then Equations 7 and 9 may not describe the CMC behavior in a regime where the fiber is not carrying the bulk of the load. Additional studies that include lower stresses and lower temperatures are suggested as to illuminate this relationship.

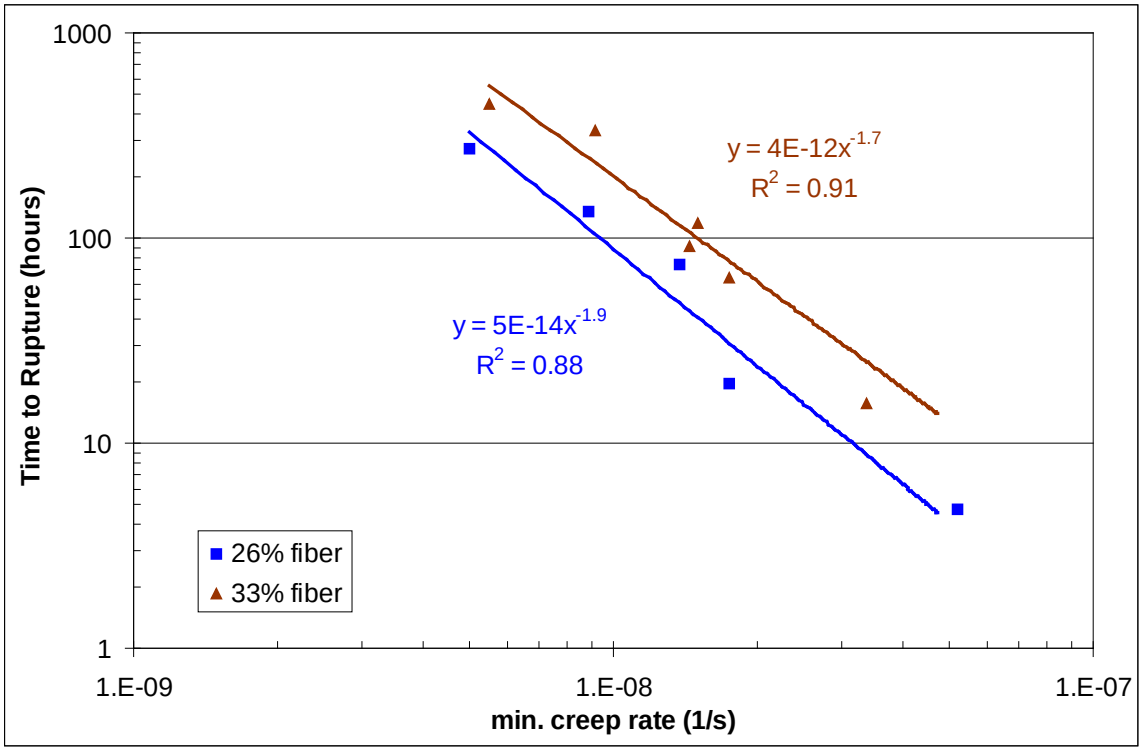

Figure 45. Monkman-Grant curves for medium- and high-fiber-volume-fraction CMC.

CONCLUSIONS AND SUGGESTIONS FOR FUTURE WORK

CHAPTER V

5.1 Conclusions

The effect of fiber volume fraction on the room-temperature tensile properties of balanced and unidirectional HiPerComp® CMCs was demonstrated. Modulus and ultimate tensile strength were observed to follow existing models. Reduced failure strain was observed at dilute fiber loadings due to unsaturated matrix cracking. The **PL** of unidirectional 0 CMCs followed ACK theory and increased with increased fiber loading.

Ply-level moduli and cracking stresses were calculated from the tensile results and compared to flexure properties. The flexure modulus and **PL** of cross-ply CMCs were accurately predicted from the ply-level properties using beam theory. Through stacking-sequence variations, the flexure modulus was varied predictably by 200% and the flexural **PL** was varied by 300%. Careful stacking-sequence selection allowed the high cracking strength of unidirectional 0 composites to be realized in flexure testing of cross-ply CMCs. The implication is that the CMC architecture can be tailored to locally tolerate stresses that are much higher than the **PL** of the bulk composite.

Based on limited data, only minor differences were seen between the tensile and flexural cracking strengths of 0 plies, indicating that this material is somewhat insensitive to volume effects. The 90 ply strength in cross-ply CMCs was 30% higher in flexure than in tension. This difference is consistent with predictions based on the measured Weibull modulus of balanced CMCs tested in tension. The strength of 90 plies in cross-ply laminates was greater than in unidirectional 90 material due to compressive residual stress imposed on the 90 plies by the 0 plies. The 90 ply cracking strength did not follow the model Beyerle et al.[9] demonstrated for glass-matrix composites in which the matrix is in residual tension.

Fiber volume fraction had significant effects on the time-dependant properties of the CMC at 1315°C. Increasing the fiber content decreased the composite creep rate, increased the rupture life, and increased the rupture strain of the CMC. The results are consistent with the expectation that the matrix creeps faster than the fiber. Matrix creep

and matrix cracking re-distribute load to the fibers. Assuming the entire load is carried by the fibers, the composite creep rate as a function of the fiber stress is consistent with published data[30] for the creep rate of the raw fiber. Post-rupture analysis revealed cracks in the 90 plies for all of the creep-rupture samples in this study. Some of these cracks are believed to be creep-induced cavitation, where the fibers running in the cross direction separated from the matrix in the radial direction at the outside of the fiber coating.

5.2 Suggestions for Future Work

A larger number of samples should be tested in flexure and in tension to conclusively demonstrate the volume effects for 0 and 90 plies. Additionally, the elevated-temperature ply-level behavior with respect to creep and **PL** could be explored. The effect of fiber volume fraction that was demonstrated on the creep behavior of balanced-architecture composites should also be observable in biased architectures. For example, the fiber volume fraction in a 2:1 biased 0:90 CMC will be 33% higher than for a balanced-architecture composite. Biasing would offer another path to utilize the effect of fiber volume fraction to tailor the high-temperature creep behavior of the CMC. Creep-induced cavitation of the 90 plies also warrants further study, as this could be a source of environmental degradation and could compromise the ability of 90 fibers to carry load in the 90 direction.

REFERENCES

1. G.S. Corman and K.L. Luthra, "Silicon Melt Infiltrated Ceramic Matrix Composites HiPerComp®"; pp. 99-115 in Handbook of Ceramic Composites. Edited by N.P. Bansal, Kluwer Academic Publishers, Boston, 2005.

2. H.M. Yun and J.A. DiCarlo, "Comparison of the Tensile, Creep, and Rupture Strength Properties of Stoichiometric SiC Fibers," NASA Technical Publication 1999-209284, NASA Glen Research Center, Cleveland, OH, 1999.

3. A.R. Bunsell and A. Piant, "A Review of the Development of Three Generations of Small Diameter Silicon Carbide Fibres," *J. Mater. Sci*., **41** [3] 823-39 (2006).

4. A.G. Evans and F.W. Zok, "The Physics and Mechanics of Fibre-Reinforced Brittle Matrix Composites," *J. Mater. Sci*., **29** [15], 3857-96 (1994).

5. W.A. Curtin, "Theory of the Mechanical Properties of Ceramic-Matrix Composites," *J. Am. Ceram. Soc*., **74** [11] 2837-41 (1991).

6. R. Nimmer, G. Corman, and R. Gilmore, "Laminate Orientation and Bias Effects on Prepreg HiPerComp™ CMC Mechanical Properties," TISCAT Report 2009GRC519, General Electric Global Research, Niskayuna, NY, 2009.

7. J. Aveston, G.A. Cooper, and A. Kelly, 1971. *The Properties of Fibre Composites*, pp. 15-16. Conference Proceedings, National Physical Laboratory, Guildford, IPC Science and Technology Press Ltd. As cited in B. Budiansky, J.W. Hutchinson, and A.G. Evans, "Matrix Fracture in Fiber-Reinforced Ceramics," *J. Mech. Phys. Solids*, **34** [2] 167-89 (1986).

8. B. Budiansky, J.W. Hutchinson, and A.G. Evans, "Matrix Fracture in Fiber-Reinforced Ceramics," *J. Mech. Phys. Solids*, **34** [2] 167-89 (1986).

9. D.S. Beyerle, S.M. Spearing, and A.G. Evans, "Damage Mechanisms and the Mechanical Properties of a Laminated 0/90 Ceramic /Matrix Composite," *J. Am. Ceram. Soc*., **75** [12] 3321-30 (1992).

10. Z.C Xia, R.R. Carr, and J.W. Hutchinson, "Transverse Cracking in Fiber-Reinforced Brittle Matrix, Cross-Ply Laminates," *Acta Metall. Mater*., **41** [8] 2365-76 (1993).

11. N. Laws and G. Dvorak, "Progressive Transverse Cracking in Composite Laminates," *J. Compos. Mater.,* **22** [10] 900-16 (1980).

12. G.N. Morscher, “Stress-Dependent Matrix Cracking in 2D Woven SiC-Fiber Reinforced Melt-Infiltrated SiC Matrix Composites,” *Compos. Sci. Technol.*, **64** [9] 1311-19 (2004).

13. G.N. Morscher, H.M. Yun, and J.A. DiCarlo, “Matrix Cracking in 3D Orthogonal Melt-Infiltrated SiC/SiC Composites with Various Z-Fiber Types,” *J. Am. Ceram. Soc.*, **88** [1] 146-53 (2005).

14. W.A. Curtin, B.K. Ahn, and N. Takeda, “Modeling Brittle and Tough Stress-Strain Behavior in Unidirectional Ceramic Matrix Composites,” *Acta Mater.* **46** [10] 3409-20 (1998).

15. W.A. Pryce and P.A. Smith, “Matrix Cracking in Unidirectional Ceramic Matrix Composites Under Quasi-Static and Cyclic Loading,” *Acta Metall. Mater.*, **41** [4] 1269-81 (1993).

16. B.K. Ahn and W.A. Curtin, “Strain and Hysteresis By Stochastic Matrix Cracking in Ceramic Matrix Composites,” *J. Mech. Phys. Solids*, **45** [2] 177-209 (1997).

17. G.N. Morscher and V.V. Pujar, “Design Guidelines for In-Plane Mechanical Properties of SiC Fiber-Reinforced Melt-Infiltrated SiC Composites,” *Int. J. Appl. Ceram. Technol.*, **6** [2] 151-63 (2009).

18. R. Talreja, “Continuum Modeling of Damage in Ceramic Matrix Composites,” *Mech. Mat.* **12** [2] 165-80 (1991).

19. F.W. Zok, “Fracture Analysis of Fiber-Reinforced Ceramic-Matrix Composites,” pp. 407-418 in ASM Handbook, Vol. 21, *Composites*. Edited by D.B Miracle and S.L. Donaldson. ASM International, Materials Park, OH, 2001.

20. J. Lamon, B. Thommeret, and C. Percevault, “Probabilistic-Statistical Approach to Matrix Damage and Stress-Strain Behavior of 2-D Woven SiC/SiC Ceramic Matrix Composites,” *J. Eur. Ceram. Soc.*, **18** [13] 1797-1808 (1998).

21. L.R. Calcote, *The Analysis of Laminated Composite Structures*. Reinhold Book, New York, 1969.

22. A.G. Evans and C. Weber, “Creep Damage in SiC/SiC composites,” *Mater. Sci. Eng., A*, **208** [1] 1-6 (1996).

23. J.Lang and J.DiCarlo, “Further Developments in Modeling Creep Effects within Structural SiC/SiC Components,” NASA Technical Report Number 20080047429, NASA Glen Research Center, Cleveland, OH, 2008. Also available at <http://ntrs.nasa.gov/archive/nasa/casi.ntrs.nasa.gov/20080047429_2008047212.pdf>

24. G.N. Morscher and V.V. Pujar, “Creep and Stress-Strain Behavior after Creep for SiC Fiber Reinforced, Melt-Infiltrated SiC Matrix Composites,” *J. Am. Ceram. Soc.*, **89** [5] 1652-8 (2006).

25. V.V. Pujar and G.N. Morscher, “Tensile Creep Behavior of Melt-Infiltrated SiC-SiC Composites for Gas Turbine Engine Applications,” *ASME Conf. Proc.*, **1,** 261-6 (2007).

26. G.N. Morscher, G. Ojard, R. Miller, Y. Gowayed, U. Santhosh, J. Ahmad, and R. John, "Tensile Creep and Fatigue of Sylramic-iBN Melt-Infiltrated SiC Matrix Composites: Retained Properties, Damage Development, and Failure Mechanisms," *Compos. Sci. Technol*., **68** [15-16] 3305-13 (2008).

27. M. McLean, "Creep Deformation of Metal-Matrix Composites," *Compos. Sci. Technol*., **23** [1] 37-52 (1985).

28. C.H. Weber, J.P.S. Lofvander, and A.G. Evans, "Creep Anisotropy of a Continuous-Fiber-Reinforced Silicon Carbide/Calcium Aluminosilicate Composite," *J. Am. Ceram. Soc*., **77** [7] 1745-52 (1994).

29. W.D. Kingery, H.K. Bowen, and D.R. Uhlmann, *Introduction to Ceramics*, 2nd ed.; pp. 708. John Wiley & Sons, New York, 1976.

30. Sauder and J. Lamon, "Tensile Creep Behavior of SiC-Based Fibers with a Low Oxygen Content," *J. Am. Ceram. Soc*., **90** [4] 1146-56 (2007).

31. B. Wilshire and M.R. Bache, "Creep of Monolithic and Fibre-Reinforced Silicon Carbide," *J. Eur. Ceram. Soc*., **28** [7] 1535-42 (2008).

32. B.A. Fields and S.M. Wiederhorn, "Creep Cavitation in a Siliconized Silicon Carbide Tested in Tension and Flexure," *J. Am. Ceram. Soc*., **79** [4] 977-86 (1996).

33. C.H. Carter Jr., R. F. Davis, and J. Bentley, "Kinetics and Mechanisms of High-Temperature Creep in Silicon Carbide: I, Reaction Bonded," *J. Am. Ceram. Soc.*, **67** [6] 409-17 (1984).

34. C.H. Carter, Jr., R.F. Davis, and J. Bentley, "Kinetics and Mechanisms of High-Temperature Creep in Silicon Carbide: II, Chemically Vapor Deposited," *J. Am. Ceram. Soc.*, **67** [11] 732-40 (1984).

35. P. Marshall, "The Relationship Between Delayed Fracture, Creep, and Texture in Silicon Carbide"; paper presented at Special Ceramics Symposium (Stoke-on-Trent, 1967), British Ceramic Research Association. As cited in C.H. Carter Jr., R. F. Davis, and J. Bentley, "Kinetics and Mechanisms of High-Temperature Creep in Silicon Carbide: I, Reaction Bonded," *J. Am. Ceram. Soc.*, **67** [6] 409-17 (1984).

36. S.M. Wiederhorn, D.E. Roberts, T. Chuang, and L. Chuck, "Damage-Enhanced Creep in a Siliconized Silicon Carbide: Phenomenology," *J. Am. Ceram. Soc.*, **71** [7] 602-8 (1988).

37. H.J. Frost and M.F. Ashby, *Deformation-Mechanism Maps: The Plasticity and Creep of Metals and Ceramics*; Fig. 9.3. Pergamon Press, New York, 1982. Also available at <http://engineering.dartmouth.edu/defmech/ >

38. A. Kebbedde, GE Global Research, Niskayuna, NY, July 2009, Private Communication.

39. J.A. DiCarlo, H.M. Yun, and J.B. Hurst, "Fracture Mechanisms for SiC Fibers and SiC/SiC Composites under Stress-Rupture Conditions at High Temperatures," *Appl. Math. Comput.*, **152** [2] 473-81 (2004).

40. J.A. DiCarlo and H.M. Yun, "Modeling the Thermostructural Capability of Continous Fiber-Reinforced Ceramic Composites," *J. Eng. Gas Turbines Power*, **124** [3] 465-70 (2002).

41. G.N. Morscher, "Tensile Stress Rupture of SiC_f/SiC_m Minicomposites with Carbon and Boron Nitride Interphases at Elevated Temperatures in Air," *J. Am. Ceram. Soc*., **80** [8] 2029-42 (1997).

42. H.G. Halverson and W.A. Curtin, "Stress Rupture in Ceramic-Matrix Composites: Theory and Experiment," *J. Am. Ceram. Soc*., **85** [6] 1350-65 (2002).

43. R.C. Hibbeler, *Mechanics of Materials*; pp. 281-287. Macmillan Publishing, New York, 1991.

44. J.H. Weaver, J. Yang, A.G. Evans, and F.W. Zok, "A Modified Test for Measuring the Interlaminar Tensile Strength of Fiber-reinforced Ceramic Composites," *Compos. Sci. Technol*., **68** [1] 10-16 (2008).

45. F. Hild, J.-M. Domergue, F.A. Leckie, and A.G. Evans, "Tensile and Flexural Ultimate Strength of Fiber-Reinforced Ceramic Matrix Composites," *Int. J. Solids Struct*., **31** [7] 1035-45 (1994).

46. J.C. McNulty and F.W. Zok, "Application of Weakest-Link Fracture Statistics to Fiber-Reinforced Ceramic-Matrix Composites," *J. Am. Ceram. Soc*., **80** [6] 1535-43 (1997).

47. A.G. Evans, J.-M. Domergue, and E. Vagaggini, "Methodology for Relating the Tensile Constitutive Behavior of Ceramic-Matrix Composites to Constituent Properties," *J. Am. Ceram. Soc.*, **77** [6] 1425-35 (1994).

48. F.W. Zok and S.M. Spearing, "Matrix Crack Spacing in Brittle Matrix Composites," *Acta Metall. Mater*., **40** [8] 2033-43 (1992).

49. J.A. Coppola and R.C. Bradt, "Measurement of Fracture Surface Energy of SiC," *J. Am. Ceram. Soc*., **55** [9] 455-58 (1972).

50. G.D. Quinn, "Weibull Strength Scaling for Standardized Rectangular Flexure Specimens," *J. Am. Ceram. Soc.*, **86** [3] 508-10 (2003).

51. U. Ramamurty, F.W. Zok, F.A. Leckie, and H.E. Deve, "Strength Variability in Alumina Fiber-Reinforced Aluminum Matrix Composites," *Acta Mater*. **45** [11] 4603-13 (1997).

52. H.M. Yun, J.A. Di Carlo, R.T. Bhatt, and J.B. Hurst, "Processing and Structural Advantages of the Sylramic-iBN SiC Fiber for SiC/SiC Components," *Ceram. Eng. Sci. Proc.*, **24** [3] 247-53 (2003).